TECHNISCHE UNIVERSITÄT MÜNCHEN
Institut für Photogrammetrie und Kartographie
Lehrstuhl für Methodik der Fernerkundung

Combination of LiDAR and SAR data with simulation techniques for image interpretation and change detection in complex urban scenarios

Junyi Tao

Vollständiger Abdruck der von der Ingenieurfakultät Bau Geo Umwelt der Technischen Universität München zur Erlangung des akademischen Grades eines

Doktor-Ingenieurs (Dr.-Ing.)

genehmigten Dissertation.

Vorsitzender: Univ.-Prof. Dr.-Ing. Uwe Stilla
Prüfer der Dissertation:
1. Univ.-Prof. Dr.-Ing. habil. Richard Bamler
2. Hon.-Prof. Dr.-Ing. Peter Reinartz
   Universität Osnabrück
3. Univ.-Prof. Dr.-Ing. Uwe Sörgel
   Technische Universität Darmstadt

Die Dissertation wurde am 18.02.2015 bei der Technischen Universität München eingereicht und durch die Ingenieurfakultät Bau Geo Umwelt am 31.03.2015 angenommen.

Abstract

Synthetic aperture radar (SAR) images have shown great potential in change detection applications but still suffer from two main difficulties: 1) interpretation of changes, 2) limitation in the availability of SAR images acquired with same incidence angles. To solve these tasks, in this dissertation, novel simulation-based techniques have been developed for image interpretation and change detection.

In this context, an enhanced SAR simulator GeoRaySAR has been developed which specializes on LiDAR digital surface models (DSM) as input data and provides geocoded simulated SAR images. Exploiting this simulator, different layers (e.g., layover, shadow) are generated for different digital elevation models (whole DSM, individual buildings and walls) by combining simulated images. Especially, a novel wall segmentation method based on image processing has been developed to identify individual walls in SAR images. Using the proposed SAR simulator and object identification methods, five change-detection methods are elaborated in this dissertation.

In order to detect new buildings, LiDAR and SAR data are compared. An algorithm is developed to distinguish increased backscattering in SAR images by analyzing the SAR pixel values extracted based on the simulated layers. To detect demolished buildings, two comparison operators (normalized mutual information and joint histogram slope) are used to compare the image patches of simulated and real SAR images related to buildings. Three further algorithms focus on change detection between SAR images acquired with different incidence angles. The first algorithm is a building-level algorithm based on layer fill. Image patches related to the same buildings in the two SAR images are extracted using the simulation methods. The change ratios based on the fill ratio of building layers are estimated for each image patch pair and classified into two classes using the expectation-maximization algorithm. The second algorithm uses the same idea and focuses on wall-level changes. Image patches related to the same walls in the two SAR images are extracted and converted to have the same geometry. The converted patch pairs are then compared using a change ratio based on the fill position. The last algorithm is a wall-level algorithm which compares the location of the local maxima in the two SAR images corresponding to the same building façade. The wall-level results can also be fused to provide results on the building-level.

The proposed algorithms are tested for scenes of Munich and San Francisco using TerraSAR-X images and meter-resolution LiDAR data. The proposed simulator provides results with good geocoding accuracy, reasonable mask layers and precise individual building layover contours. These ease the interpretation of SAR images in complex urban scenarios and enable an object-based SAR image analysis. The developed change-detection algorithms for comparing LiDAR and SAR data successfully detect the increased backscattering related to new buildings and demolished buildings with an overall accuracy of more than 90%. The other three change-detection algorithms focus on different levels of change details, which therefore provide options for different applications of change detection. The building-level algorithm works well for buildings with different size and shape in complex urban scenarios. The wall-level algorithms are relatively time-consuming but yield better results for partly demolished buildings. In conclusion, the proposed SAR simulator GeoRaySAR and its application in change detection have shown great potential in different remote sensing applications and provide a good basis for future related works.

Keywords: Digital surface model (DSM), Synthetic aperture radar (SAR), Data fusion, SAR simulation, Change detection, Image interpretation, Mutual information, Wall segmentation, GeoRaySAR.

Zusammenfassung

Synthetische Apertur Radar (SAR) Bilder weisen großes Potential im Bereich der Änderungsdetektion auf. Jedoch werden diese mit zwei Herausforderungen konfrontiert: 1) Schwierigkeit in der Interpretation von Änderungen, 2) Limitierung durch die Anforderung der gleichen Einfallswinkel der SAR Bilder. Um diese zwei Schwierigkeiten zu lösen, werden in dieser Dissertation für die Bildinterpretation und Änderungsdetektion innovative Methoden entwickelt, die auf Simulation basieren.

Hierfür wird ein SAR Simulator GeoRaySAR entwickelt, der LiDAR digitale Oberflächen Modelle (DOM) als Input Daten verwendet und geokodierte simulierte Bilder generiert. Dieser Simulator ermöglicht in Kombination von simulierten Bildern aus diversen digitalen Höhenmodellen (ganze DOM, individuelle Gebäude, Wände) unterschiedliche Layers (z.B. Überlagerung, Schattenwurf) zu generieren. Insbesondere wird eine neuartige Wandsegmentierungsmethode zur Identifizierung individuelle Wände in SAR-Bildern entwickelt, welche auf Bildverarbeitung basiert. Unter Verwendung des SAR Simulators und Objekterkennungsmethoden werden fünf Änderungsdetektionsmethoden in dieser Dissertation herausgearbeitet.

Für die Detektion neuer Gebäude werden ein LiDAR und ein SAR Datensatz miteinander verglichen. Ein Algorithmus analysiert SAR Pixelwerte des entsprechenden simulierten Layers zur Detektion ansteigender Rückstreuung in SAR-Bildern. Um zerstörte Gebäude zu erkennen, werden zwei Vergleichsoperatoren (Normalized Mutual Information und Joint Histogram Slope) verwendet, damit Bildabschnitte der simulierten und der ursprünglichen SAR Bilder derselben Gebäude verglichen werden. Drei weitere Algorithmen sind für die Änderungsdetektion zwischen SAR Bildern mit unterschiedlichen Einfallswinkeln entwickelt worden. Der erste Algorithmus detektiert Änderungen auf der Gebäudenebene. Bildabschnitte derselben Gebäude in zwei SAR Bildern werden mit Hilfe des Simulators extrahiert. Für jedes Paar der Bildabschnitte wird die Änderungsrate der Füllmengenverhältnisse von Gebäude-Layers geschätzt. Die Änderungsrate aller Gebäude wird mit dem Expectation-Maximization Algorithmus in zwei Klassen klassifiziert. Der zweite Algorithmus verwendet eine ähnliche Herangehensweise und ist spezialisiert auf Änderungen auf der Wandebene. Bildabschnitte derselben Wände in zwei SAR Bildern werden extrahiert und konvertiert, sodass diese die gleichen Geometrie haben. Diese konvertierten Paare von Bildabschnitten werden dann mit Hilfe von Änderungsrate der Füllmengenverhältnisse verglichen. Der letzte Algorithmus arbeitet ebenfalls auf der Wandebene. Dieser vergleicht Positionen der lokalen Maxima in den zwei SAR Bildern derselben Fassade. Die Fusion von resultierenden Veränderungen der Wände können Änderungen an Gebäuden aufweisen.

Diese Algorithmen sind anhand von TerraSAR-X Bildern und LiDAR Daten von München und San Francisco getestet worden. Der entwickelte Simulator generiert simulierte Resultate mit hohen Geokodierungsgenauigkeit, zum anderen sinnvolle Layers und präzise individuelle Konturen der Gebäuden, welche die Interpretation von SAR Bildern in komplexen urbanen Gebieten vereinfacht und eine objektbasierte Analyse von SAR Bilder ermöglicht. Der entwickelte Änderungsdetektionsalgorithmus für den Vergleich von LiDAR und SAR Daten haben erfolgreich die angestiegene Rückstreuung der neuen Gebäude und zerstörten Gebäude mit einer Genauigkeit von mehr als 90% detektiert. Die drei anderen Änderungsdetektionsalgorithmen für Vergleiche von SAR Bildern mit unterschiedlichen Einfallswinkeln können auf verschiedene Ebenen von Änderungsdetails fokussieren und ermöglicht daher Optionen für unterschiedliche Anwendungen. Der Algorithmus auf der Gebäudenebene ist für Gebäude unterschiedlicher Größen und Formen in komplexen urbanen Gebieten geeignet. Die Algorithmen auf der Wandebene sind relativ zeitaufwendig, erzielen jedoch bessere Ergebnisse für teils zerstörte Gebäuden. Insgesamt weisen der

vorgeschlagene SAR Simulator GeoRaySAR und seine Anwendung in Änderungsdetektion großes Potenzial für unterschiedliche Anwendungen in der Fernerkundung auf und bieten eine gute Basis für zukünftige relevante Arbeiten.

Schlüsselwörter: Digital Oberflächenmodelle (DOM), Synthetic Aperture Radar (SAR), Datenfusion, SAR Simulation, Änderungsdetektion, Bild Interpretation, Mutual Information, Wand Segmentierung, GeoRaySAR.

Dissertationstitel auf Deutsch: Simulationsbasierte Fusion von LiDAR- und SAR-Daten zur Bildinterpretation und Änderungsdetektion in Stadtgebieten.

List of abbreviations

|	
2D	Two Dimension
3D	Three Dimension
CAD	Computer-Aided Design
CityGML	City Geography Markup Language
DEM	Digital Elevation Model
DLR	German Aerospace Center
DSM	Digital Surface Model
DTM	Digital Terrain Model
EM	Expectation-Maximization
EMS	European Macroseismic Scale
GEC	Geocoded Ellipsoid Corrected
GeoRaySAR	Geocoding extended ray-tracing based SAR simulator
GIS	Geographic Information System
ID	Identifier number
JHS	Joint Histogram Slope
KI	Kittler-Illingworth
KL	Kullback-Leibler
LiDAR	Light Detection And Ranging
MI	Mutual Information
MRF	Markov Random Field
nDSM	normalized Digital Surface Model
NMI	Normalized Mutual Information
PDF	Probability Density Function
POV	Persistence Of Vision
Radar	Radio Detection And Ranging
RaySAR	Ray-tracing based SAR simulator
SAR	Synthetic Aperture Radar
SSC	Single look Slant range Complex
SVM	support vector machine
SWT	stationary wavelet transformation
TMF	Triplet Markov Field
TUM	Technische Universität München
UDWT	Undecimated Discrete Wavelet Transformation
UTM	Universal Transverse Mercator (map projection)
VHR	Very High Resolution
WGS84	World Geodetic System 1984 (global reference system)

Contents

1 Introduction

1.1 Motivation

Due to the sensor's independence on weather and solar illumination, Synthetic Aperture Radar (SAR) images have been used in different change-detection applications, like damage assessment, flood monitoring, and have shown their great potential. High resolution satellite SAR missions like TerraSAR-X/TanDEM-X and COSMO-SkyMed with spatial resolutions up to one meter enable a detailed analysis of urban man-made objects. However, the exploitation of SAR images in change-detection applications suffers still from two challenging tasks.

First, SAR images are often difficult to visually interpret, especially in dense urban areas. As illustrated in Fig. 1.1, it is hard to determine the location of streets, the boundaries of buildings or to identify individual buildings (e.g. to find the two towers of the Frauenkirche in the SAR image). This is related to the distortion effects pertinent to the SAR imaging concept. The layover effects lead to a mixture of backscatter from different objects at the same position in the SAR images; the shadow effects make many objects invisible; multiple scattering leads to bright lines, point signatures or even ghost scatterers (Auer et al. 2011) and causes high local contrasts in intensity. Man-made objects with different heights, shapes, materials or surface roughness appear in SAR images very differently, which also leads to unclear object boundaries. Nevertheless, exploiting these effects may bring us information which may be not contained in other kind of data (e.g. optical images or LiDAR data). For example, point signatures are strong hints of buildings (Soergel et al. 2006) and provide information about façade details such as windows or balconies (Auer et al. 2010a). Bright lines caused by double reflection signals indicate the boundaries of buildings (Wegner et al. 2010; Auer and Gernhardt 2014).

Second, the majority of applications of SAR images in change-detection applications are based on the comparison of pre- and post-event space borne SAR images captured with the same incidence angle. However, because of the satellite orbit trajectory - e.g. for TerraSAR-X the maximum site access time is approximately 2.5 days (adjacent orbit) and the revisit time is 11 days (same orbit) - the first available post-event SAR image may be captured with a different incidence angle. In urgent situations such as earthquakes, this data have to be analyzed for changes in order to support local decision makers as fast as possible.

However, it is a challenging task to detect the changes in SAR images captured with different signal incidence angles, since the same building appears differently in such cases: i) wall layover areas are scaled in range direction, ii) object occlusions are different, affecting the object visibility, shadow size, etc. iii) multiple reflections of signals related to building structures may be different. Accordingly, a traditional pixel based comparison is not suitable as it would lead to a large amount of false alarms.
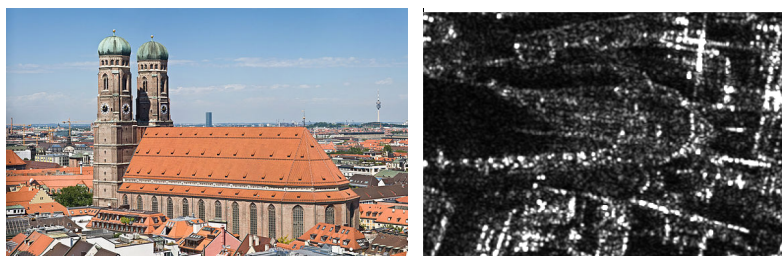
Fig. 1.1: SAR Interpretation is a challenging task: Frauenkirche in Munich (left, ©Wikipedia) and its surroundings in a TerraSAR-X image (right).

1.2 Objectives and contributions

To solve the previously described challenging tasks, novel techniques are developed and presented in this thesis. In this framework, four main novel contributions are introduced:

1. An enhanced SAR simulator to automatically generate geocoded simulated radar images;
2. A novel simulation-based algorithm to identify different layers (e.g., shadow, layover) of digital surface models, individual buildings and walls in SAR image;
3. Novel simulation-based algorithms for change detection between LiDAR and SAR data;
4. Novel simulation-based algorithms for change detection between SAR images acquired with different incidence angles.

In the next sub-sections these main objectives and novelties are briefly described.

1. An enhanced SAR simulator to automatically generate geocoded simulated radar image

Most of the existing SAR simulators provide simulated images only for visual interpretation. This thesis presents a new approach for supporting the automatic interpretation of high resolution SAR images in complex scenarios. To this end, a simulator named GeoRaySAR, which includes an automatic processing chain for generating and geocoding of simulated radar images, has been developed, based on the simulator RaySAR (Auer et al. 2010b) and digital surface models as geometric information for urban scenes.

2. Novel simulation-based algorithm to identify different layers of DSMs, individual buildings and walls in SAR image

The backscattering of different buildings and walls are often mixed together in the SAR images, making it difficult to analyze them individually. To identify the individual walls and buildings in the SAR images, buildings are extracted from the DSM. An algorithm based on image processing has been developed to separate individual walls of the building models. Various simulated images and different layers (layover, shadow, double bounce and ground) are generated for whole scenes as well as for individual buildings and walls, with consideration of neighboring influences. The identification of these layers enables the object-based analysis of the corresponding SAR images.

3. Novel simulation-based algorithms for change detection between LiDAR and SAR data

Most algorithms of change detection using SAR images require SAR images acquired with the same acquisition geometry. For making the analysis independent on SAR acquisition geometry, a novel algorithm for change detection between LiDAR and SAR data has been developed. To this end, different simulated images of the LiDAR data have been generated. A pixel-based method has been developed to detect increased backscattering between simulated and SAR images. To detect demolished buildings, normalized mutual information (NMI) and a novel comparison operator named joint histogram slope (JHS) are used to compare the sub-images in the real and simulated images according to the same buildings. The combination of these two operators is discussed thereafter.

4. Novel simulation-based algorithms for change detection between SAR images acquired with different incidence angles

To the author's knowledge, none of the existing methods in literatures has been developed to compare SAR images with different incidence angles. In this thesis, several methods based on the simulation technique are developed to detect demolished buildings and/ or walls by comparison of SAR images with different incidence angles. For this purpose, image patches according to the same building or walls in the two SAR images are extracted by simulation methods. Different region-based (layer fill ratio, fill position) and feature-based (point location) methods were developed to detect demolished buildings or walls. The experiment using Munich data has shown that, not only completely demolished buildings but also partly demolished buildings can be detected correctly.

1.3 Structure of the thesis

The thesis is structured in seven chapters. The present chapter describes the motivation of this thesis, and pointes out the objectives and main novel contributions.

Chapter 2 describes the basics on LiDAR and SAR data with their geometric properties. Besides the SAR simulator RaySAR is described.

Chapter 3 presents the developed SAR simulator GeoRaySAR and aims at the first objective described in Section 1.2. In particular, the state of the art of SAR simulation is introduced. The development of GeoRaySAR based on the existing simulator RaySAR is discussed in detail. Especially, the simulation parameters and geocoding steps are presented.

The second objective is addressed by chapter 4 and chapter 5. Chapter 4 presents a simulation based method for the identification of different layers (e.g., layover, shadow) of DSMs and individual buildings. Chapter 5 presents the developed method to separate individual wall segments in building models. The identification of walls in the SAR image is experimentally shown.

Chapter 6 refers to the third and fourth objectives. It presents the newly developed change detection algorithms based on simulation techniques. In this context, the state of the art of SAR change detection techniques and its application for damage assessment are introduced. The algorithms by comparing LiDAR and SAR data to detect increased backscattering and demolished buildings are presented in Section 6.2. In Section 6.3-6.5, novel change detection algorithms for comparing SAR images with different incidence angles are presented. The comparison and combination of all the proposed change detection methods is presented in Section 6.6.

Lastly, Chapter 7 draws the contributions of this thesis and provides an outlook to future work.

2 Basics

In this chapter, the two main input data of this thesis: LiDAR data and SAR data with their geometric properties are briefly introduced. Besides the SAR simulator RaySAR is described.

2.1 LiDAR data

LiDAR (Light Detection and Ranging) is a remote sensing technique that uses light in the form of a pulsed laser to measure distance (Ackermann 1999; Weng and Quattrochi 2006). It is one of the main methods (LiDAR, optical stereo matching, SAR interferometry, SAR radargrammetry) to derive digital surface models (DSM). In comparison to the other two sensors, LiDAR provides points with higher accuracy, especially in urban scenarios. That is why it is chosen as an input data for the SAR simulator in this dissertation. A detailed description of LiDAR can be found in Fujii and Fukuchi (2005) and Rottensteiner and Briese (2002).

The LiDAR data is derived normally with airborne sensors. The original LiDAR output data is a point cloud with 3D point coordinates. This point cloud includes all the objects which reflect LiDAR signal back to the sensor (e.g., trees, grass, ground and buildings). Since only the buildings are interesting targets in this thesis for change-detection analysis, a digital estate map (DFK, digitale Flurkarte) indicating the building footprints is used to discard the vegetation points. After resampling the point cloud into one meter grid in a software "Quick Terrain Modeler" (parameters: adaptive triangulation, maximum height, antialiasing), a digital surface model without vegetation is generated. The generated DSM is located in UTM coordinate system with ellipsoidal heights. The horizontal resolution is one meter while the vertical accuracy is 0.1 meter.

2.2 SAR data

Radar (Radio detection and ranging) is a technique which uses transmitted microwaves to measure the distances between the sensor and targets. Based on this, synthetic aperture radar (SAR) is an imaging radar system, which illuminates the scene in side looking geometry and records the reflected signals of targets in a raw data image which is thereafter processed to a SAR image. Detailed information of SAR systems can be found in the following books: Oliver and Quegan (2004) and Soergel (2010). In this section, only a brief introduction of SAR characteristics will be given.

2.2.1 SAR acquisition geometry

The side-looking geometry of SAR acquisition is illustrated in Fig. 2.1. The sensor (on platforms like satellite or airplane) flies parallel to the azimuth direction, and transmits signals in slant range direction. The angle between nadir and the line-of-sight of SAR sensor is called the incidence angle θ.

Since the radar sensor measures the distance, reflected signals of the objects, which are located in the same nadir-range plane and have the same distance to the sensor, will be recorded in the same image cell of the SAR azimuth-range image. The side-looking geometry of the SAR sensor together with uneven terrain leads to different geometric distortions, such as layover and shadow, especially in urban scenarios. The layover effect is related to the overlaid signals of walls and grounds. The shadows are regions with no reflected signals because of occlusions of high objects in range direction. Besides of these geometric distortions, signals with several reflections show sometimes strong intensity in a
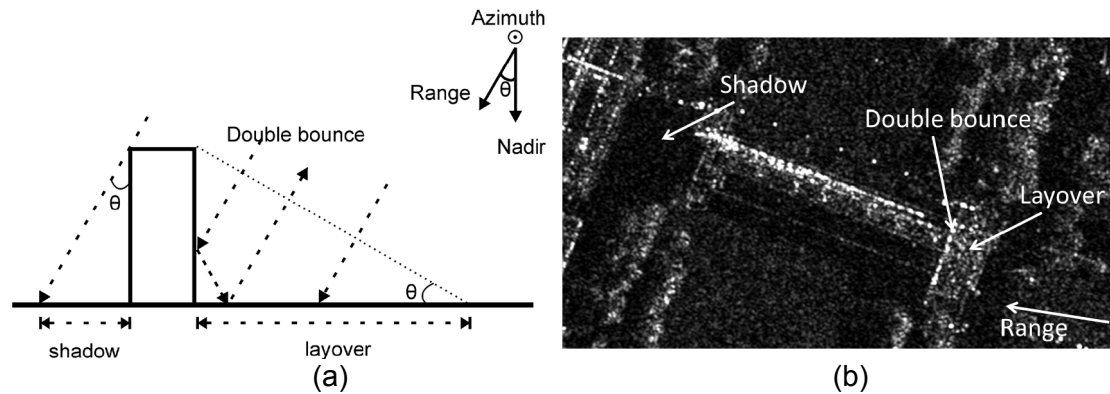
Fig. 2.1: Sketch of the SAR acquisition geometry and geometric distortions (a) with an example building in the city center of Munich in TerraSAR-X image (b).

SAR image. This is related to special geometric shapes (dihedral or trilateral corners) in the scene. These shapes lead to the effect, that signals travelling with different paths but same distance will be recorded in a line or a point. Especially the double bounce effect often appears in a building corner and forms a bright line related to the building footprint. Fig. 2.1a illustrates the principle of geometrical distortions (layover, shadow and double bounce), and an example building in SAR image with these effects is shown in Fig. 2.1b.

2.2.2 SAR radiometry

Every pixel in a SAR image stores two values of the signal: amplitude and phase. The amplitude value indicates the reflection strength of a target, which can be used to recognize the building. In this thesis, only the amplitude values of SAR images are used. Since the grey value in an image is also called image intensity, the word "intensity" in this thesis means also the amplitude, instead of "amplitude square" defined in physics.

For most cases in urban areas, the backscattering intensity of different areas will be ordered like this: shadow<ground<layover<double bounce. The intensity of roof backscattering is dependent on its material (grass, tile, or metal) and surface roughness. So its intensity can be as weak as a ground or as bright as layover areas.

SAR images are affected by "speckle noise", which is the result of interferences between the complex signals from scatterers in a resolution cell. To reduce this kind of noise, different speckle filters were developed, like Lee (Lee 1981) and Wavelet (Xie et al. 2002). In this thesis, a non-local filter (Deledalle et al. 2009) is used to reduce the speckle noise. Instead of using surrounding pixels, the non-local filter uses all similar pixels in the image to estimate a filtered value of a target pixel. Compared to other traditional filters, this filter is more time consuming but leads to better results.

2.2.3 SAR products

Until now, several meter-resolution spaceborne SAR sensors like TerraSAR-X, TanDEM-X and COSMO-SkyMed have been launched and have provided lots of earth-observation data. These data are acquired with different acquisition modes (SpotLight, ScanSAR, StripMap) and polarizations. The acquired data are provided with different product types (SSC, MGD, GEC, and EEC). More information about TerraSAR-X processing and products can be found in Breit et al. (2010). In this thesis, TSX data with high-resolution SpotLight mode are used. This kind of data have a coverage of 5km×10km (azimuth × ground range), with a ground resolution of 1m×1.5m (azimuth × ground range). For a better comparison with other data

sources, the geocoded product type of SAR data "GEC" is chosen. GEC is an abbreviation of geocoded ellipsoid corrected. This kind of product is presented in a map geometry with ellipsoidal correction but no terrain corrections. The frame mean height of the respective scene is added to the semi-major and semi-minor axes of WGS84 ellipsoid as correction (Breit et al. 2010). Besides, the image is resampled to a pixel spacing of 0.5m × 0.5m.

2.3 SAR Simulator RaySAR

For the interpretation of high resolution SAR images, a SAR imaging simulator RaySAR has been developed by Stefan Auer at the Chair of Remote Sensing Technology, Technische Universität München. A detailed description of RaySAR can be found in Auer et al. (2010a), (2010b) and Auer (2011). In this section, RaySAR is briefly introduced.

RaySAR contains three main components: modeling, sampling and scatterer analysis. The modeling is performed to provide geometrical shape and radiometric surface characteristics of objects, as well as the position and parameters of a virtual SAR sensor. The sampling of object scene is performed based on ray tracing methods provided by POV-Ray (Buck 2014), an open-source ray-tracing software. The detected signal responses from objects are stored with relevant information (e.g., signal amplitude, position, bounce level and intersection points). Based on this data, 2D and 3D simulation results are provided by the scatterer analysis. In this dissertation, only the 2D simulated images (also called reflectivity maps) are used for different applications.

RaySAR focuses on geometrical correctness, while simplified diffuse and specular reflection models are applied for simulating the radiometry of SAR images. The main advantages of RaySAR are

- simulation in 3D (azimuth, range, elevation),
- separability of different reflection levels,
- identification of the origin of reflected signals (link between signal and object geometry), and
- speed and availability of different data interfaces (POV-Ray continuously enhanced by the community since 1991).

Based on RaySAR, an extended version of simulator GeoRaySAR is developed in this thesis (see Chapter 3).

3 GeoRaySAR: Automatic SAR simulation using LiDAR data

As discussed in the introduction, SAR images are often difficult to visually interpret. To support the interpretation of SAR images, a novel SAR simulator named **GeoRaySAR** (**Geo**coding extended **ray**-tracing based **SAR** simulator) has been developed and is introduced in this chapter. GeoRaySAR, which extends the Simulator RaySAR, is an automatic processing chain of simulation, specializing on LiDAR DSM as input data, and provides geocoded simulated images.

Parts of this chapter have been published in: Tao et al. (2014), (2012), (2011c).

3.1 State of the art: SAR (imaging) simulation

To support the interpretation and processing of SAR images, various simulators developed with different techniques have been proposed in literature. There are mainly two groups of simulators: SAR raw data simulators including raw data processing (Franceschetti et al. 2003; Margarit et al. 2006) and SAR imaging simulators directly providing images (Mametsa et al. 2002; Xu and Jin 2006; Balz and Stilla 2009; Brunner et al. 2011; Hammer and Schulz 2011; Auer et al. 2010). Raw data simulators consider dielectric properties and roughness parameters of building materials exploiting the intensity of reflected radar signals (Guida et al. 2008). SAR imaging simulators focus on the use of detailed building CAD (computer-aided design)-models, often with simplified surface material information as input. A detailed overview of different concepts for SAR simulation is presented in Balz (2010).

Commonly, the output of the simulators is images in the azimuth-range coordinate system, which can only be visually compared with real SAR images. In Gelautz et al. (1998), Wegmueller (1999), Balz et al. (2008) and Auer (2011), correlation techniques are used for matching the simulated image with a real SAR image for building retrieval. In Brunner et al. (2010b) mutual information is used in a function optimization method to find the translation between the simulated and real SAR images.

However, correlation techniques should be avoided for the following reasons in case geometric information is available for the image matching. First, the correlation of a simulated image with a SAR image (typically approx. 10000 × 6000 pixels) is very time consuming, unless a manual reduction of the searching area is done before. Second, the correctness of the matching depends on the features in the simulated images. The matching may fail for small simulated images from individual buildings, which include a low number of dominant features. Finally, the matching may be unstable due to a mistakenly confusion of features related to different buildings, which is the worst case scenario that needs to be avoided. To the authors' knowledge, none of the simulators reported in literature enables to provide geocoded simulated images for a direct comparison with real SAR data.

In our previous publication (Tao et al. 2011a), the matching of a simulated image with a SAR image was also tried, based on the detected line features in both images. It works only well for a DSM with moderate size and the SAR image patch must be manually cut to suitable smaller size. This approach was discarded and replaced by the geocoding step described in the following sections.
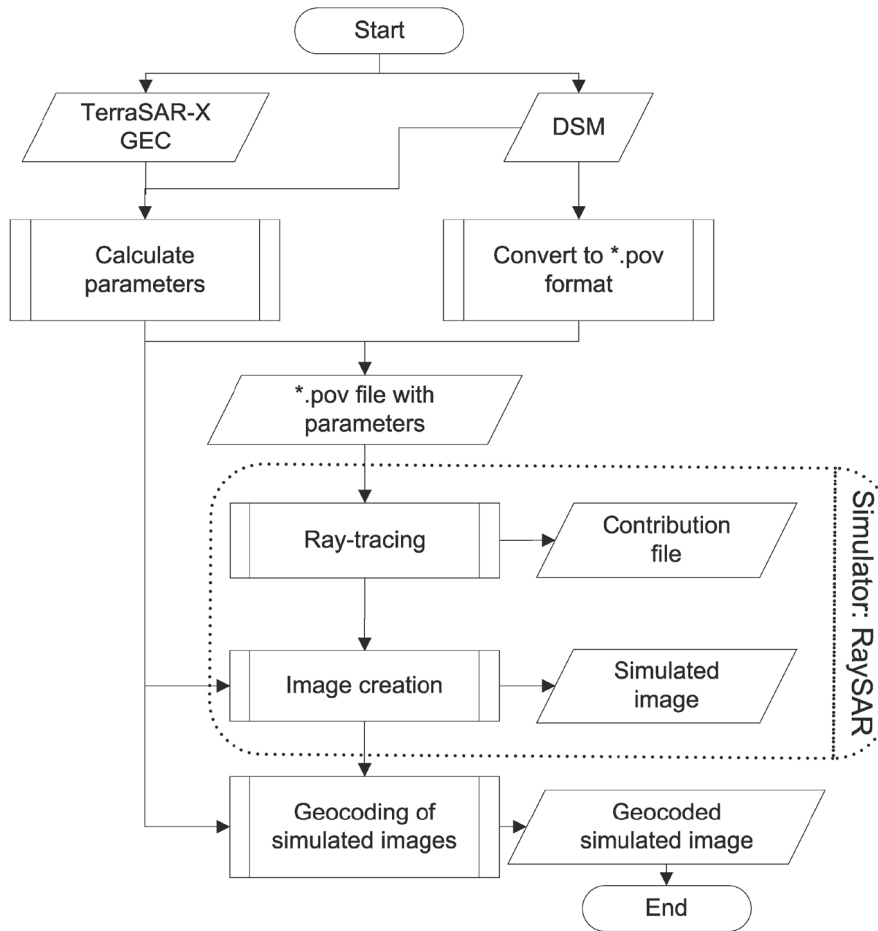
Fig. 3.1: Automatic processing chain of simulator GeoRaySAR.

3.2   Methodology

Based on the simulator RaySAR mentioned in Section 2.3, an automatic processing chain of simulation, specializing on digital surface models as input data, has been developed. In this context, building information may be based on optical data, LiDAR data or a given digital elevation model (DEM). Thereafter, we use the geoinformation of the DSM as well as the orbit and projection parameters of the real SAR image to geocode the simulated image, which enables a direct comparison with the real SAR image. The processing chain is illustrated as a flowchart in Fig. 3.1. The main contribution of this dissertation for the simulation process is to extrapolate the input parameters for the steps ray tracing, image creation and geocoding, corresponding to sections 3.2.2, 3.2.3 and 3.2.4, respectively (see Fig. 3.1).

At this point, it shall be emphasized that the processing chain is not restricted to the RaySAR package or simulators based on ray tracing. Alternative solutions based on low-level digital surface models may be based on any SAR simulator representing direct backscattering and double reflections.

3.2.1 Input data

As the real SAR image, we use the TerraSAR-X GEC product, which is presented in a map geometry (in the east and north direction) with ellipsoidal correction. The mean height of the respective scene (frame mean height) is added to the semi-major and semi-minor axes of
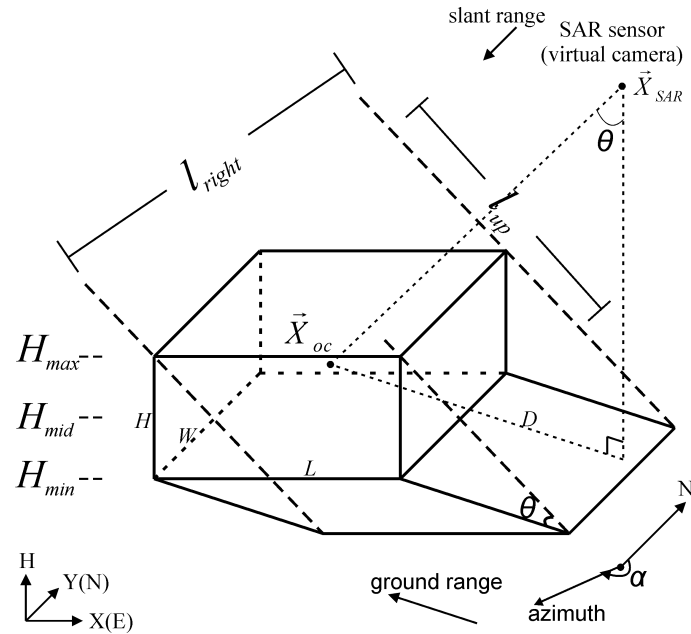
Fig. 3.2: Parameters for simulation and geocoding.

WGS84 ellipsoid as correction (Breit et al. 2010). It can be considered as a projection of the TerraSAR-X SSC product (Breit et al. 2010) on a horizontal plane using the frame mean height. From its metadata (the xml file), the following parameters are directly extracted for the next steps:

1) the frame mean height H_{fm}, ('meanHeight' in the xml file) (see Fig. 3.4);
2) the azimuth angle α ('headingAngle' in the xml file) (see Fig. 3.2, Fig. 3.3);
3) five signal incidence angles θ (see Fig. 3.2) at the frame center and 4 corners, which are used to interpolate the signal incidence angle for the scene center (assumed to be locally constant for the whole scene);
4) the pixel spacing in east and north direction δ_{SE}, δ_{SN}, which equal the pixel spacing in azimuth and ground range direction δ_{S_az}, δ_{S_rg} for the TerraSAR-X GEC product (e.g., 0.5 m x 0.5 m).

The second input data is a digital surface model based on LiDAR data. The DSM is a raster image in the UTM coordinate system with the ellipsoidal height as pixel value, where height information related to vegetation has been removed. Its sampling of the DSM should be similar to the sampling of the SAR image. In this context, the following parameters are required for subsequent processing steps:

1) length L and width W (in east and north direction, respectively) (see Fig. 3.2, Fig. 3.3);
2) pixel spacing in east and north direction δ_{LE}, δ_{LN};
3) the UTM coordinate of the northwest corner X_{DSM}, Y_{DSM};
4) the maximum and minimum height H_{max}, H_{min}, which lead to the middle height $H_{mid} = (H_{max}+H_{min})/2$ and the height difference $H=H_{max}-H_{min}$ (see Fig. 3.2).

The geometric accuracy of GEC products is normally better than 1 m (Breit et al. 2010). The airborne LiDAR data has normally an accuracy of several centimeters. A common coordinate system is chosen for both data sources (WGS 84 ellipsoid, UTM coordinate, ellipsoidal heights).
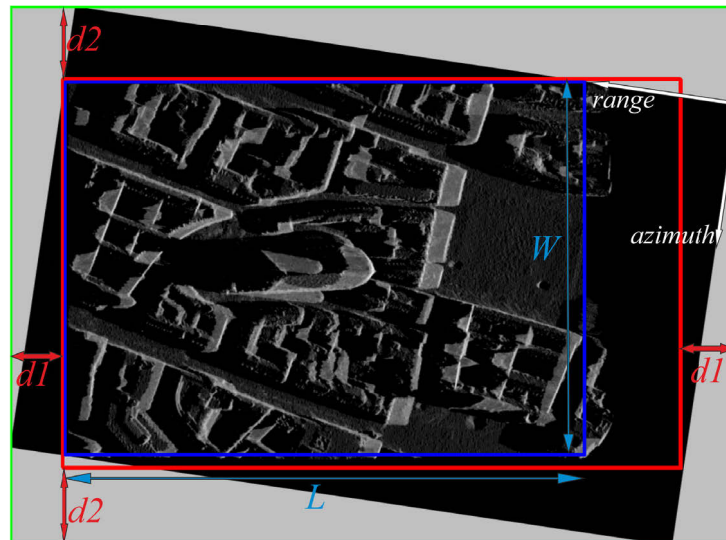
Fig. 3.3: Geocoding step 1 using DSM geoinformation (blue rectangle: area of DEM; black: simulated image in azimuth and range direction; green: rotated simulated image in east north direction; red: cropped image as final result).
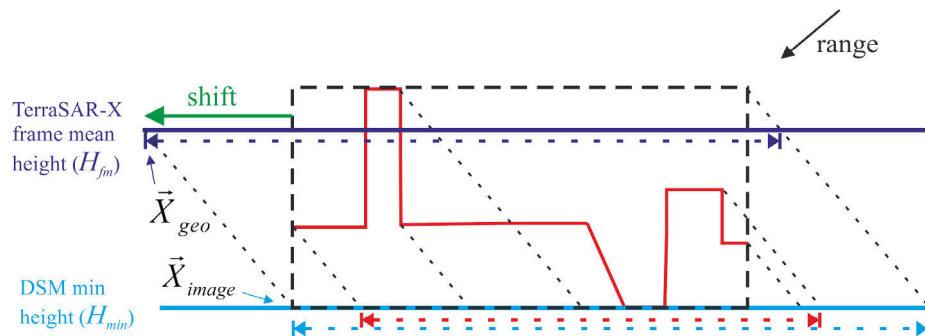
Fig. 3.4: Geocoding step 2: impact of height difference on geocoding of simulated image (The red lines indicate the geometry of the DSM. The black dashed box fully contains the DSM and is projected onto the plane marked in cyan. The cyan dotted line indicates the area of the simulated image. The blue dotted line indicates the area of the real SAR image.).

3.2.2 **Calculating parameters for ray tracing**

For ray tracing in POV-Ray, the DSM is converted to the POV-Ray format (.pov), which uses triangles to describe the model. The simulator RaySAR is developed for analyzing local urban scenes where the local incidence angle of the radar signal is assumed to be constant (flat wave front assumption in the far field of the antenna). Therefore, a signal source emitting parallel light is defined in POV-Ray for representing the radar signal emitter and an orthographic camera receiving parallel light for representing the radar receiver. Thereby, the coordinates of signals in the far field can be directly simulated without modeling the synthetic aperture (Auer et al. 2010b). In more detail, the following scene and rendering parameters have to be defined:

    1) the position of the scene center;
    2) the position of the signal source (radar sender) emitting parallel light;
    3) the position and cover area of the virtual orthographic camera (radar receiver);
    4) the size of the simulated image.

The scene center refers to the center of a box which contains the DSM exactly:

$$\vec{X}_{oc} = [\frac{L - \delta_{LE}}{2}, H_{mid}, \frac{W - \delta_{LN}}{2}]. \tag{3.1}$$

Then, the positions of the signal (light) source and the orthographic camera are the same:

$$\vec{X}_{SAR} = \vec{X}_{oc} + [-D\cos\alpha, \frac{D}{\tan\theta}, D\sin\alpha], \tag{3.2}$$

where D (see in Fig. 3.2) is any positive number (e.g. 1000), which describes the horizontal distance between the SAR sensor position and the scene center. The variability of D is related to the parallel signal assumption. Based on Equation 3.1 and Equation 3.2, the line of sight of the virtual sensor is defined.

The cover area of the orthographic camera can be defined with l_{right}, l_{up}, spanning the axes in the azimuth and elevation direction (orthogonal to azimuth and slant range direction), respectively (see Fig. 3.2):

$$l_{right} = \|L\sin\alpha\| + \|W\cos\alpha\|$$
$$l_{up} = (\|L\cos\alpha\| + \|W\sin\alpha\|)\cos\theta + H\sin\theta. \tag{3.3}$$

These two values can be understood as the projected range of the DSM box on the azimuth-elevation plane.

Based on these distances, the size (pixels) of the simulated image in azimuth-ground range geometry can be calculated as:

$$I_{columns} = \frac{l_{right}}{\delta_{S\_az}}, \quad I_{rows} = \frac{l_{up2}}{\delta_{S\_rg}\sin\theta},$$
$$where: l_{up2} = (\|L\cos\alpha\| + \|W\sin\alpha\|)\sin\theta + H\cos\theta. \tag{3.4}$$

The values l_{right} and l_{up2} can be understood as the projected range of the DSM box on the azimuth-slant range plane. The denominators in Equation 3.4 represent the pixel size in azimuth and slant range direction, respectively.

Finally, the output of POV-Ray (named contribution file in Fig. 3.1) contains the discrete position as well as the strength and reflection level of the simulated signals, forming the input for the SAR image creation step.

3.2.3 Calculating parameters for image creation

For generating images, the limit area of the signal contribution has to be defined as follows:

$$S_{azimuth\_min} = -I_{columns} \cdot \delta_{S\_az}/2,$$
$$S_{azimuth\_max} = -S_{azimuth\_min}$$
$$S_{range\_min} = \frac{D}{\sin^2\theta} - \frac{l_{up2}}{2\sin\theta},$$
$$S_{range\_max} = S_{range\_min} + I_{rows} \cdot \delta_{S\_rg}. \tag{3.5}$$

In this context, the values $S_{azimuth\_min}$ and $S_{azimuth\_max}$ relate to the azimuth distance, i.e. the minimal and maximal distance of the object surface to the SAR sensor in azimuth direction. Their difference is l_{right}. The values S_{range_min} and S_{range_max} relate to ground range, i.e. the minimal and maximal range distance of the object surface to the SAR sensor (virtual camera) projected to the ground plane. Their difference is $l_{up2}/\sin\theta$. The component $D/\sin^2\theta$ refers to the ground range distance between the scene center and the SAR sensor.

3.2.4 Geocoding of simulated image

The output of basic RaySAR is a simulated image in azimuth-range geometry (alternatively: azimuth-ground range geometry). The geocoding of this image includes two steps:

- step 1: using the DSM geoinformation to project it in a plane in UTM-coordinate system;
- step 2: shift of the image in consideration of different projection planes.

In this context, geocoding does not mean orthorectification. Instead, it only means the projection of the simulated image from the azimuth-range geometry onto a horizontal plane. A correction of the earth curvature for this plane is neglected because of the simulation of local scenes. The radiometric distortion of the simulated image caused by geocoding is not of significance as the simulator is generally limited in radiometric correctness (simplified models for diffuse and specular reflection). The procedure of geocoding is explained in more detail in the following.

Geocoding step 1: using DSM geoinformation

Step 1 is based on the geoinformation of the DSM and the projection geometry. The principle is to project the simulated image from the azimuth-slant range plain onto a horizontal plain with a constant height, which is equal to the minimal height value H_{min} of the used DSM (see Fig. 3.4, cyan marked line).

As an example, this principle is illustrated with a simulated image in Fig. 3.3. The blue rectangle marks the area covered by the DSM. Using RaySAR, we obtain a simulated SAR image within the area marked in black. With a clockwise rotation of (α – 90°), we get the green marked image, which is oriented in east-north direction. Considering the projection in viewing direction of the camera, only the red marked area contains meaningful values. Hence, we cut the border of the green marked image in both horizontal and vertical direction with range of $d1 = \|W\cos\alpha\sin\alpha\|$ and $d2 = \|L\cos\alpha\sin\alpha\|$. Thereafter, the geocoding of the red image can then easily be conducted using the geocoded DSM as follows:

$$X_{image} = \begin{cases} X_{DSM}, & \text{if } \alpha \in [90°, 270°] \\ X_{DSM} - H\tan(90° - \theta)\cos\alpha, & \text{if } \alpha \in [0°, 90°) \cup (270°, 360°) \end{cases}$$

$$Y_{image} = \begin{cases} Y_{DSM}, & \text{if } \alpha \in [180°, 360°] \\ Y_{DSM} + H\tan(90° - \theta)\sin\alpha, & \text{if } \alpha \in [0°, 180°). \end{cases}$$

(3.6)

Geocoding step 2: consideration of different projection planes

The second step is concerned with the difference of the projection plane of the geocoded SAR image and the projection plain used in step 1. In more detail, the difference of the "frame mean height" of the TerraSAR-X GEC product and the minimum DSM height leads to a constant shift between the simulated image and the real SAR image.

The principle of geocoding step 2 is shown in Fig. 3.4. The 2D-shift between the simulated image and the real SAR image is calculated and the geocoding can be corrected as follows:

$$X_{geo} = X_{image} + (H_{fm} - H_{min})\tan(90° - \theta)\cos\alpha$$
$$Y_{geo} = Y_{image} - (H_{fm} - H_{min})\tan(90° - \theta)\sin\alpha,$$

(3.7)

where X_{geo} and Y_{geo} are the UTM coordinates of the northwestern corner of the geocoded simulated image.

3.3 Experimental results

To demonstrate the results of our simulation method, we use a LiDAR DSM of Munich city center (size 600 m × 400 m) with a vertical and horizontal resolution of 0.1 m and 1 m, respectively (see Fig. 3.5). Several isolated building blocks are included in this DSM with a height of about 30 meter. Furthermore, a church (Frauenkirche) can be distinguished in the DSM, characterized by two towers with a height of about 100 meter. The DSM includes no vegetation.

The real TerraSAR-X image (spotlight mode, GEC product) captured at June 6th 2008 with an incidence angle of about 50° from a descending orbit is shown in Fig. 3.6a.

For the simulation, it is assumed that all surfaces in the scene consist of the same material which therefore exhibits the same radiometric reflection properties with respect to specular and diffuse reflection. Therefore, the radiometric correctness of the simulation result is moderate. However, this is not a problem as the appearance of signals in the simulated images is by far good enough for extracting the geometric information needed for identifying the scene components. The overestimation of diffuse reflections is welcomed as the DSM lacks geometric details about scene objects. To obtain the appearance of point scatterers dominating the SAR image seen in Fig. 3.6a, a city model with a detailed representation of object details (facade and roof structures, balconies, etc.) is required. In contrast, the realistic case of a given 2.5D DSM (one height value per pixel) without surface material information enables only to represent the extent of surfaces in the simulated images. However, this is sufficient for the separation of layover, shadow and ground areas (see Chapter 4).
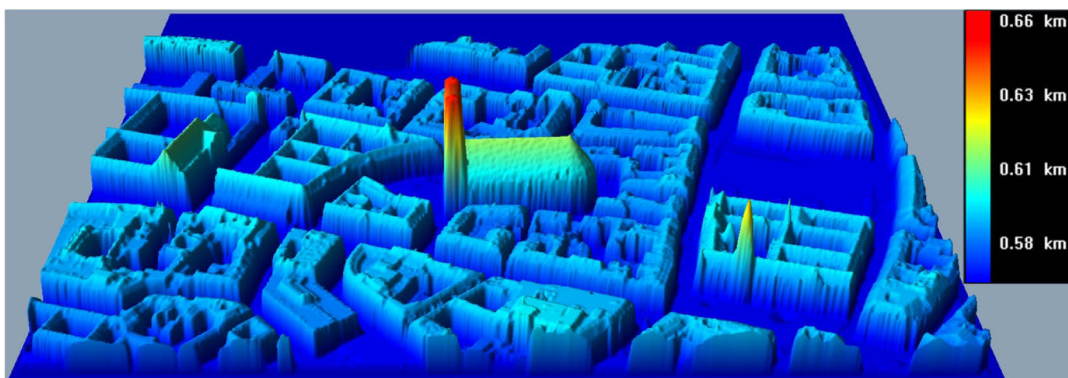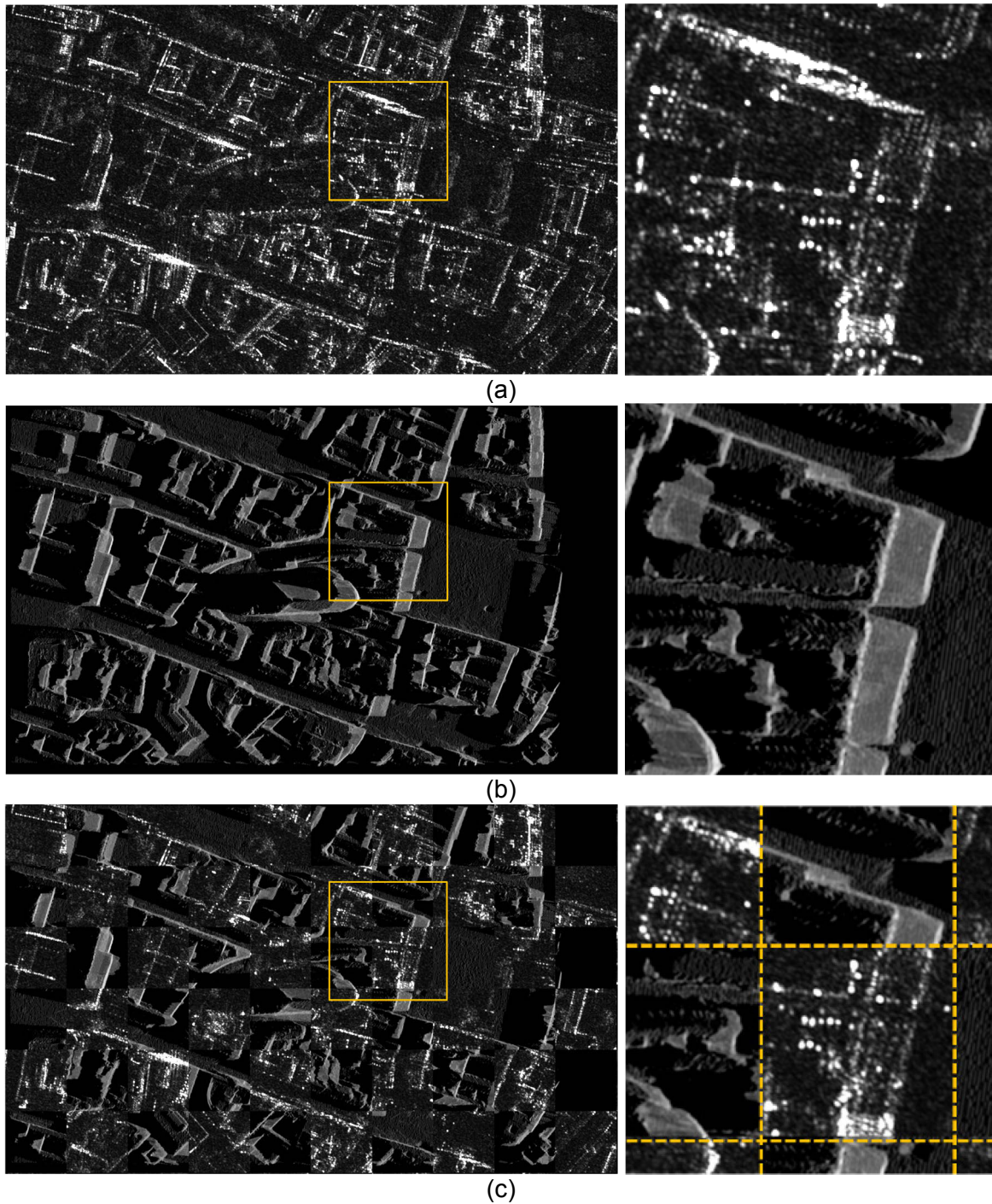

Fig. 3.5: LiDAR digital surface model of Munich center.

(a)

(b)

(c)

Fig. 3.6: Simulated results of the whole scene of the Munich city center. a) TerraSAR-X GEC product, b) geocoded simulated image, c) chessboard view of the real and simulated image. The orange rectangles in the left images mark the area for zoom-in in the right images.

The simulated image (Fig. 3.6b) contains single and double reflection signals. The simulation of reflection levels higher than two is not reasonable as the geometry of structures related to signal multiple reflections is mostly not represented by the 2.5D DSM.

For indicating the geocoding accuracy, Fig. 3.6c shows a chessboard-like view (consisting of squares arranged in two alternating images) of the simulated image and the real SAR image. Although we partly obtain high radiometric differences, the geometry of the building layover areas shows good correspondence. On the right of Fig. 3.6, a close-up view of the simulation

results is shown for a selected area (see orange rectangles in the left images in Fig. 3.6). Especially, the geocoding accuracy can be better distinguished, e.g. the correspondence of wall layover in Fig. 3.6c.

Simulation Performance

Due to the hypothesis of parallel rays, a constant incidence angle (interpolated to the scene center) has been used for the simulation of the whole scene. Therefore the correctness of the geocoding of buildings will be maximum in the scene center and minimum at the scene boundaries. A correction of the earth curvature for the projection of simulated images onto horizontal plane is neglected. Both of these assumptions show little effect on the simulation of local scenes (error of translation lower than 0.1 meter in case of object height 100 meter, incidence angle circa 40 degree and scene width 400 meter). Apart from these theoretical assumptions, the accuracy of geocoding depends on the accuracy of the input DSM. For instance, errors in the DSM location lead to a shift of the simulated images. A large pixel spacing (e.g., > 2m) of the DSM leads to a low comparability of the simulated images.

The simulation procedure based on ray tracing is memory consuming, which, at the present state, leads to a limited size of the input DSM (current limit approx. 2000 m × 2000 m). For simulation of larger DSM scenes it is suggested to split it into small ones.

Using a Linux computer (Inter Core2 Quad CPU 2.83GHz, 8GB RAM, 64-bit Linux operation system CentOS 5.8), the whole scene (size 600 m × 400 m) is simulated in less than 40 seconds.

3.4 Summary

In this chapter, a new simulation approach is presented for supporting the interpretation of VHR SAR images in complex urban scenarios. To this end, a fully automatic processing chain based on the simulator RaySAR has been developed, specialized in using digital surface models as input data. After a geocoding step, the simulated image can be directly compared to the real SAR image.

In this context, a limitation has been discussed. The constant incidence angle used in simulation leads to a limited geocoding correctness at the scene boundaries. This effect is negligible for the simulation of small local scenes where the impact of the DSM resolution and accuracy is of more importance.

The potentials of the proposed methodology are manifold. Firstly, the automatic processing chain enables SAR simulations to focus on a number of user specific buildings. Providing an xml file of a SAR scene and a user specific patch of a LiDAR DSM, the simulator will calculate all the required parameters accordingly and provide the simulated images. Secondly, the geocoding approach eases the application of simulation results to real SAR data. Correlation techniques for matching the simulated and real SAR images are no longer needed. Lastly, the presented algorithm is not restricted to the RaySAR simulator, but can also be adapted to other simulation concepts based on rendering techniques.

4   SAR object identification on DSM and building level

Using the SAR simulator described in Chapter 3, this chapter presents a method to identify different SAR scene image in global and local scenes. The global identification means the identification of different layers over the whole scene (double bounce, layover, shadow, and ground). The local identification is related to the detection of layover and shadow of individual buildings.

Globally simulated layers enable an area based analysis of the SAR image, e.g., the change detection described in Section 6.2.2. Complementary, locally simulated results support the development of object-based methods, e.g., the building-level change detection described in Section 6.3.

Part of this chapter appears in: Berger et al. (2013); Tao et al. (2014).

4.1   State of the art: object identification in SAR images

Different techniques for object detection from SAR images are presented in the literature. Some of them use linear features to extract edges (Touzi et al. 1988), roads (Tupin et al. 1998) or double bounce lines (Ferro et al. 2011; Wegner et al. 2010). Based on the knowledge of building shapes and their composition of structured primitives, buildings with special characters can be detected from single high resolution SAR images. Simonetto et al. (2005) used L-shaped echoes to extract buildings in airborne SAR images. Barthelet et al. (2012) detected buildings using a maximum likelihood model inversion performed from low-level primitives. Ferro et al. (2013) presented a method for the automatic detection and 2D reconstruction of building footprints from single SAR images.

These methods for the detection of buildings from single SAR images work only well for specific buildings (rectangular shape and isolated). They may fail for building complexes with courtyards or dense buildings in city centers.

Instead of using single SAR images, ancillary data may ease the detection of buildings. Sportouche et al. (2011) projected the detected footprints from optical image into SAR data to get an improved superposition of building features. Brunner et al. (2010b) combined building footprints in GIS-data and one SAR image to analyze the building location in SAR images and building heights. In the dissertations of Bolter (2001) and Soergel (2003), simulation methods were used for the detection and reconstruction of buildings from SAR images.

Ancillary data can also help to identify layover and shadow layers in SAR images. Schreier (1993) analyzed the distance and viewing angles of pixels in a DEM with respect to a SAR sensor's location to detect layover and shadow regions. Based on the same idea, Soergel et al. (2005) detected layover and shadow regions using GIS data for the SAR mission planning.

Exploiting the LiDAR DSM data, this section will use the simulation method to identify buildings and layers in the SAR images. Thanks to the detailed LiDAR information, this method enables to identify all buildings contained in the DSM without a limit to rectangular buildings. The layover and shadow layers can be detected not only for the whole DSM scene but also for individual buildings.

4.2 Global identification on DSM level

Global identification is related to combining the geocoded simulated images of the DSM for generating layover, shadow, ground and double reflection layers of the whole scene.

In Arefi et al. (2011), a hierarchical image filtering motivated from gray-scale reconstruction was developed to eliminate 3D above-ground objects as well as below ground outliers from a DSM. Using this methodology, a digital terrain model (DTM) and a normalized digital surface model (nDSM) are generated from the input DSM. Based on these three models (see the left column of Fig. 4.1) as input, different simulated SAR images including signals of reflection levels 1 and/or 2 are generated. In this regard, the following simulated images are relevant (see the center column of Fig. 4.1):

- **image A**: double reflections from DSM
- **image B, C and D**: sum of all reflection levels (here: single and double reflections) for DSM, DTM and nDSM, respectively.

Afterwards, the images are combined in different ways to generate five image layers for identifying different image parts:

1. double reflection (A>0)
2. layover (D>0)
3. shadow (B=0 & C>0)
4. background (B=0 & C=0)
5. ground (B>0 & A=0 & D=0).

At this point, it shall be mentioned that the layover layer does not only include building wall reflections but also signals from building roofs. Moreover, the ground layer includes signals from streets, squares and vegetated areas. The background layer indicates areas with no signals from all three models, which is not really relevant in the context of the real SAR image.

The principle of generating layers is visualized in Fig. 4.1 for an example DSM (including the Alte Pinakothek and a part of TUM building). Eventually, the layers can be imposed on the real SAR image for analyzing different image parts of interest, e.g. layover or shadow areas located within the urban scene.

4.3 Local identification on building level

Individual building models are extracted from the DSM in order to identify the corresponding SAR image parts. In this context, the influence between adjacent buildings in the azimuth-range plane can be revealed.

The generated layover layer of the whole scene provides the layover areas of all buildings which are often overlapping in dense urban areas. For indicating individual building layers in the SAR image, isolated parts in the nDSM exceeding a threshold on the size (chosen according to the size of the building of interest, e.g. > 1500 pixels) are considered as individual buildings and are extracted. Using a similar method described in section 4.2, three layers (layover, shadow, double bounce) of the buildings are generated. Note that instead of the three elevation models used in section 4.2, we generate a plane with constant height (median height of building neighborhood) as DTM, combine the plane with the building model as DSM, and use the building model as nDSM.
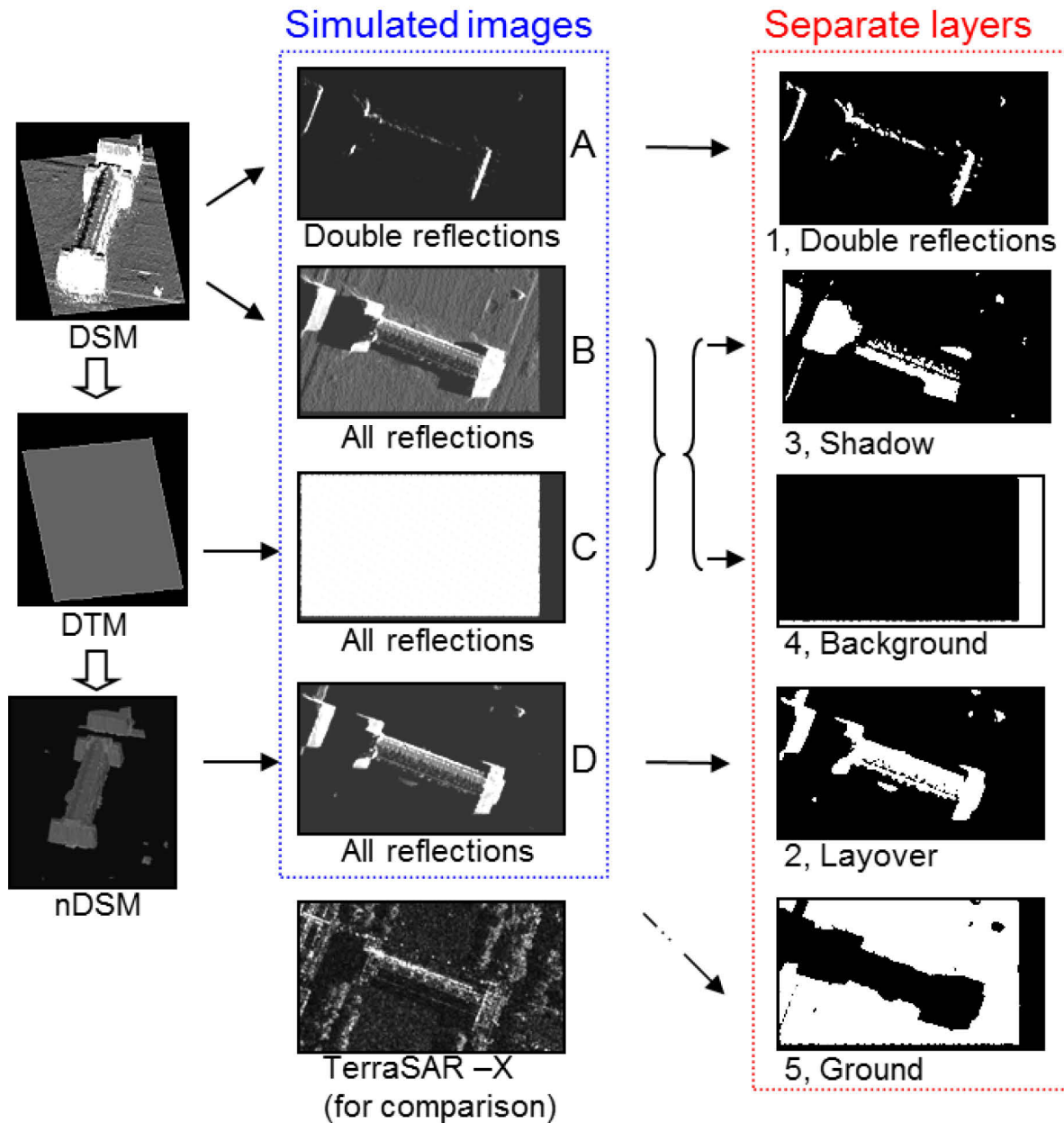
Fig. 4.1: Simulation of separate layers: From the elevation models (left), four simulated images are generated (center); the combination of them yields five image layers for scene interpretation (right).

The simulated layover and shadow layer of individual buildings does not include the influence of neighboring urban objects. For obtaining this information, the intersection area of the local (individual building) and global (whole scene) layer is calculated in order to generate a fused layer for individual buildings.
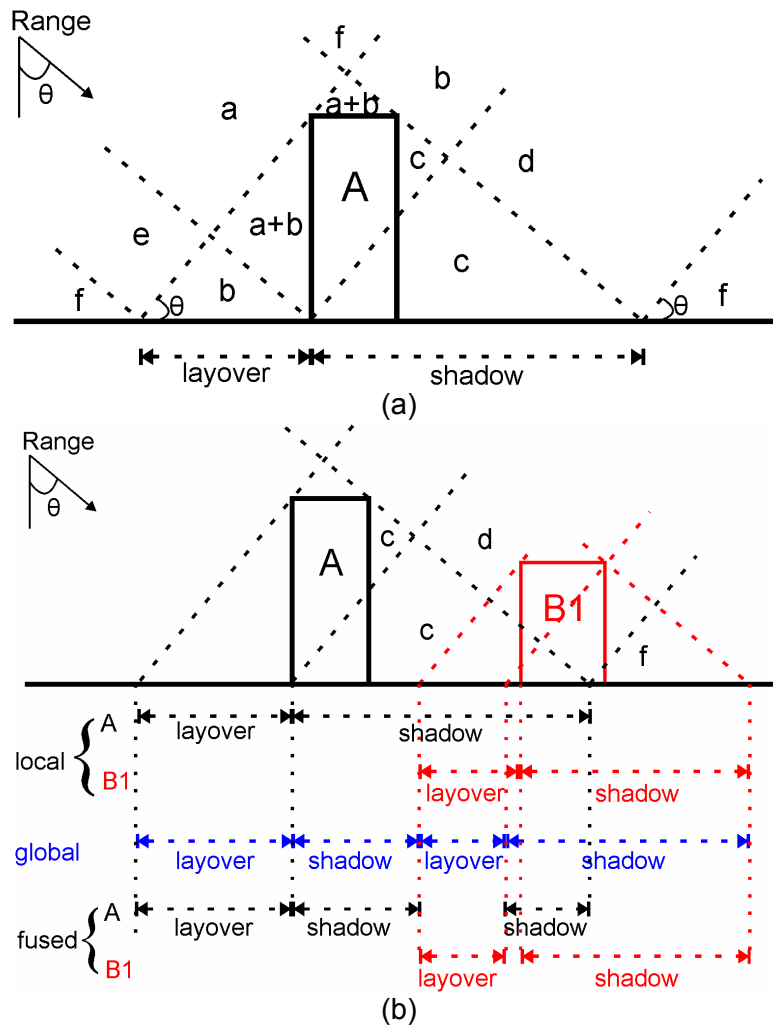
Fig. 4.2: Influence of neighboring buildings in the SAR imaging geometry. The upper image generally describes the influence areas: Areas (a-f) near building A which may be covered by a neighboring building B. The related effects in the SAR image are: a: B partly or fully covers A; b: the layover areas of A and B are mixed; c: B is in shadow of A; d: the layover of B covers the shadow of A; e: the layover of A covers the shadow of B; f: no influence between A and B. The lower image gives an example: the red building B1 is located in areas c, d and f. Then, building A shortens the extent of the layover of B1. Moreover, the layover signals of B1 superpose the shadow area of A. The dotted arrows mark the local, global and fused shadow and layover areas of both buildings.

Fig. 4.2a generally describes the influence areas next to a building. An example with a neighboring building is illustrated in Fig. 4.2b. The shadow of building A is influenced by building B1, the layover of building B1 is influenced by building A as it is partly covered. Accordingly, the fused shadow layer of building A and fused layover layer of building B1 are different from the original one.

The proposed fusion method for indicating individual building layover area works for most situations with except for specific cases. Taking Fig. 4.2b as an example, a fully hidden building located in area c may still have a fused layover area because of signals from another building standing in area d. For this special situation, a visibility analysis (e.g., Soergel et al. 2003) of the entire model surface may be needed.

4.4 Experimental results

4.4.1 Results of Munich Data

Global identification

Using the same data set as in Section 3.3, different image layers (blue: shadow; green: ground; red: layover; cyan: double reflections; grey: background) generated from the simulation results are visualized in Fig. 4.3b. The layover and shadow layers improve the understanding of different brightness in the SAR images. The double bounce layer highlights most of the bright backscattering in the SAR image. Since the building walls in the DSM are modeled with triangles, which are not perpendicular to the ground, the double bounce layer is thicker than expected (see the right image in Fig. 4.3b). For the intended goal of this dissertation, the generated double bounce layer is sufficient for image interpretation. For a better identification of double bounce layers, more precise data (e.g., GIS data, or enhanced DSM model (Arefi and Reinartz 2013)) is needed.

(a)

(b)
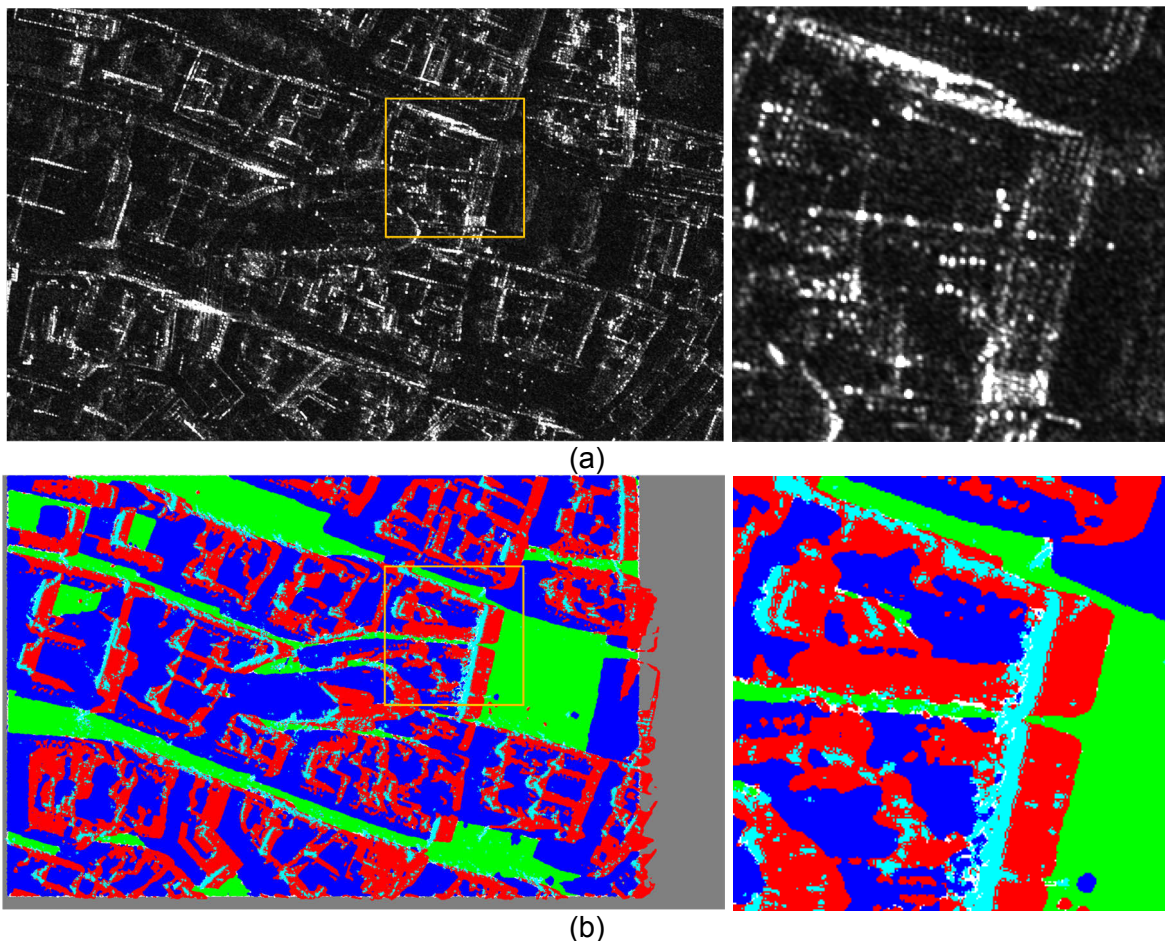
Fig. 4.3: Simulated results of the whole scene of the Munich city center. a) TerraSAR-X GEC image, b) separate layers (blue: shadow; green: ground; red: layover; cyan: double reflections; grey: background). The orange rectangles in the left images mark the area for the zoom-in in the right images.

Local identification

For an extended evaluation, 20 building models, exceeding a size larger than 1500 pixels, are extracted from the DSM as described in Section 3.3. For a local detailed interpretation of the SAR image, five buildings around the Frauenkirche are chosen for simulation. Their models with IDs, simulated images, and contours of layover and shadow areas are shown in Fig. 4.4. Different colors indicate different buildings.

In Fig. 4.4c the building layover and shadow areas can be clearly distinguished. Some of them fit very well to the signal responses in the real SAR image, like the layover of building 12 (red). Some of them do not fit, like the layover of building 9 (green). The reason is that building 9 is partly covered by the tower of building 12.

To provide a correct identification of individual layover areas, the intersection area of local and global layover are calculated. Fig. 4.5a shows the contours of local (green) and fused (magenta) layover area of building 9 superimposed on the TerraSAR-X image. The fused contours include the influence of the neighboring buildings and, are now comparable to the real SAR image. A similar procedure can be performed using the intersection of local and global shadow to generate a fused individual building shadow mask. An example can be seen in Fig. 4.5b which shows the local (green) and fused (red) shadow of building 12.

Using the same computer as Section 3.3, the simulation of an individual building model takes about 4 seconds.

(a) (b)

(c)
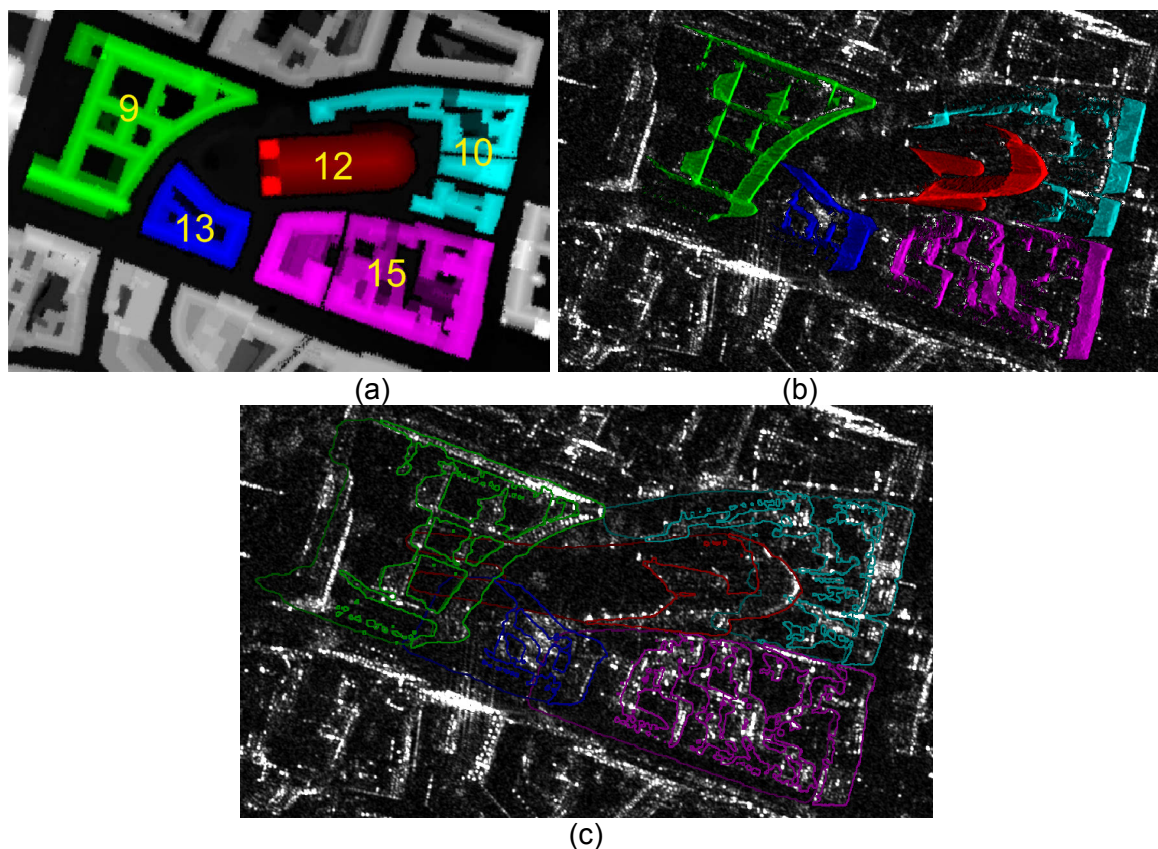
Fig. 4.4: Simulated results of individual buildings: (a) nDSM with highlighted extracted individual building models and their IDs; (b) simulated images and (c) layover (bright color) and shadow (dark color) contours superimposed on TerraSAR-X image. Different colors indicate different building models in the images.

(a)

(b)
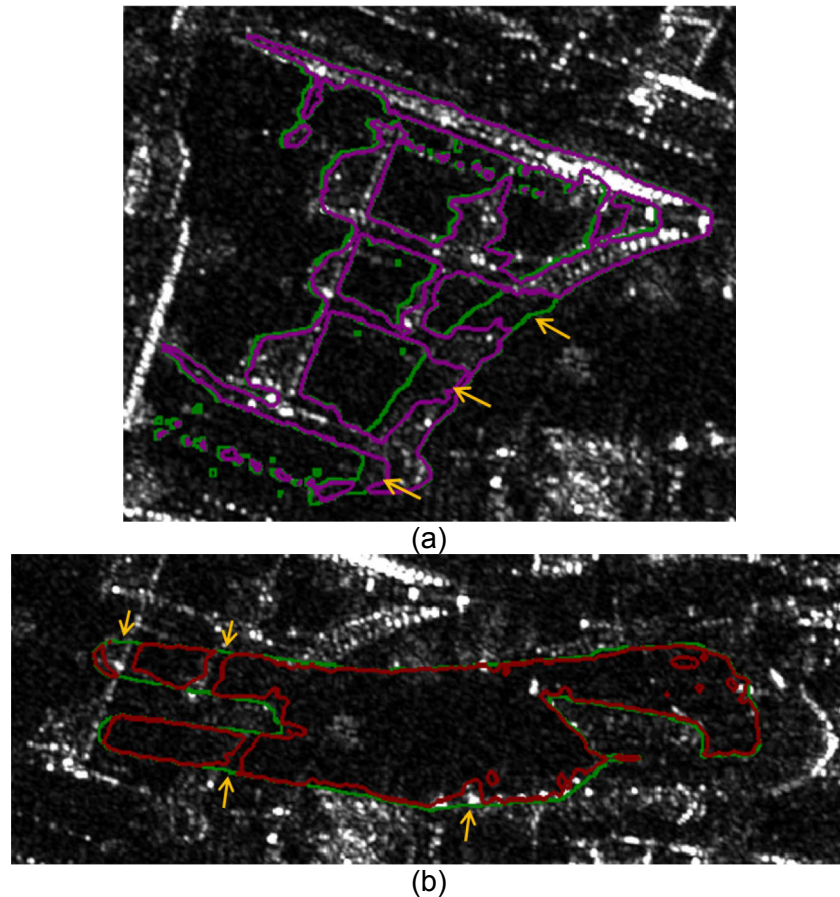
Fig. 4.5: Fusion of local and fused layers for individual buildings: (a) local (green) and fused (magenta) layover of building 9; (b) local (green) and fused (red) shadow of building 12. The orange arrows mark the main differences between local and fused layers.

4.4.2 Results of San Francisco Data

In order to test the functionality of the proposed approach with different data sets and object properties, a data set on a dense area with high buildings in San Francisco is chosen. In this area, the layover and shadow related to different buildings are mixed more often and the scene is more difficult to interpret. This data set was provided by the 2012 IEEE Data Fusion Contest.

The provided LiDAR point clouds are converted to a DSM with a pixel spacing of 0.5m×0.5m and a vertical accuracy of 0.1m in a WGS84 coordinate system. The TerraSAR-X image was captured on October 13th, 2011 with an incidence angle of about 40° from a descending orbit.

As an example, five building models are chosen from the DSM and shown in Fig. 4.6a. The contours of the corresponding simulated layover, superimposed on the geocoded TerraSAR-X image, are depicted in Fig. 4.6c. Different colors indicate different building models. Parts of the layover area of the red building are overlapped with signal responses from the green and blue buildings. It is clearly seen which layover parts and, hence, signature patterns are related exclusively to the red building. This helps to understand why the façade of the red building in the real SAR image has an abnormal pattern in the overlapping area.
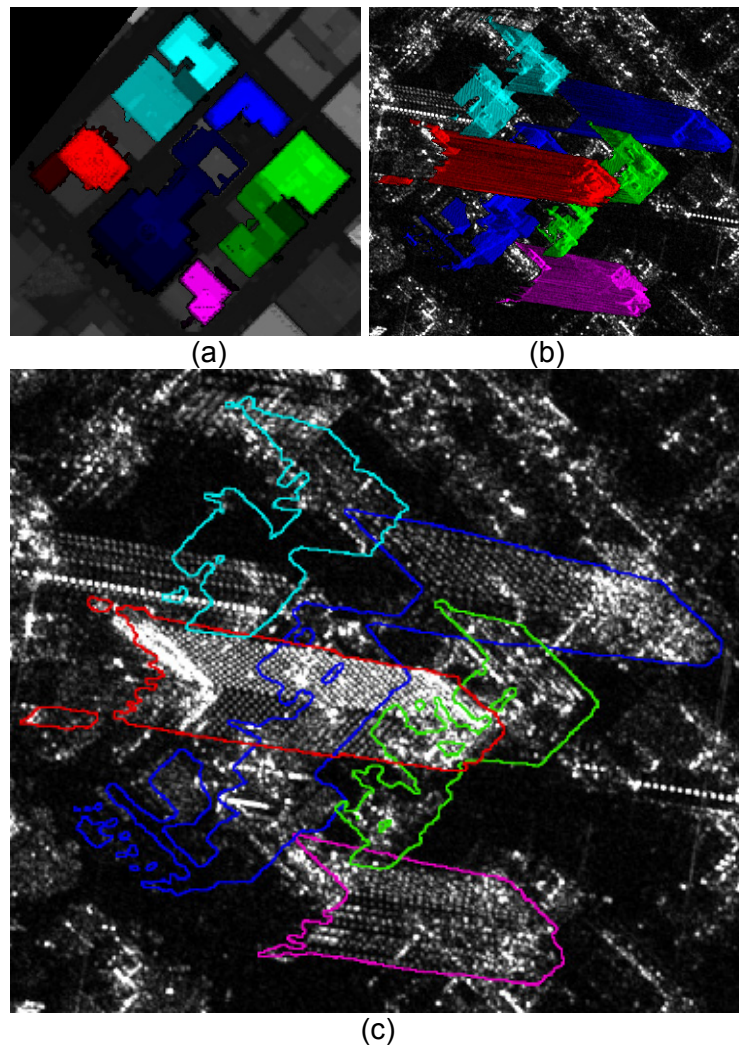
Fig. 4.6: Interpretation of TerraSAR-X spotlight image in urban area of San Francisco. (a) Individual building models; (b) simulated layover areas and (c) layover contours imposed on TerraSAR-X image. Different colors indicate different building models in the images.

4.5 Summary

This chapter illustrates a simulation based method to identify building-related parts in SAR images. Using the simulator described in chapter 3, different simulation results are combined to generate four image layers indicating double bounce reflection, layover, shadow, and ground areas, for the whole scene as well as for individual buildings. The generated global and local layers are then fused in consideration of neighboring building influences to identify the boundaries of layover and shadow areas of individual buildings.

The experimental results of Munich and San Francisco data have shown great potential of the proposed methodology. Building boundaries are clearly marked in the SAR images. Overlapping areas of different building layovers are presented, which helps the interpretation of SAR image in dense urban scenarios with tall buildings.

The identified layers and buildings enable an object-based analysis of the SAR images, e.g., the change-detection methods described in Chapter 6.

5 SAR detailed identification of objects on wall level

Chapter 4 describes a simulation-based method to identify building layover and shadow layers in SAR images. Since building façades are related to a high number of signatures in the side-looking SAR images, it is interesting to identify individual wall facades in SAR images for the analysis of wall patches, e.g. the wall change-detection described in Sections 6.4 and 6.5.

In this chapter, a method for segmentation of individual wall models from DSM is presented. Based on the simulator described in Chapter 3, the segmented individual wall models are then used to predict the façade layover areas in SAR images.

5.1 State of the art: Building modeling

Since almost two decades, research on automatic building modeling has been a very active area. Different techniques for building modeling using LiDAR data have been presented in the literature. Verma et al. (2006) combined simple parametric shapes to model complex buildings. Lafarge et al. (2008) approximated building footprints with connected rectangles. Zhou and Neumann (2008) proposed a data-driven algorithm which automatically learns the principal directions of roof boundaries and uses them in building footprint production. Arefi and Reinartz (2013) extracted 3D building models from DSMs and orthorectified images.

An important review of building modeling is presented by Haala and Kada (2010). This article presented the state of the art of reconstruction methods and their respective principles. The existing building modeling techniques are summarized in this article in 3 categories: 1) modeling using simple parametric shapes of common buildings; 2) construction based on point cloud segmentation; 3) reconstruction by DSM simplification.

Most of the existing techniques aimed at polyhedral building objects, which use roof shapes and footprints to describe buildings. The walls are normally described by combined vertical planes.

Different from the existing algorithms, a new method is presented in this chapter for the specific application of wall-layover identification in SAR images. To this end, wall models are segmented from the provided LiDAR DSM. The major distinct features of the proposed method are: 1) the output wall models are described with triangulated mesh (instead of vertical planes), which is the same as the used DSM description in the SAR simulator, so that the fusion of local and global layover layers will use a unique data source and avoid systematic errors; 2) relevant wall parameters (e.g., wall gradient direction) are accordingly estimated, which are important for the wall-selection and wall-layover-conversion in the change-detection methods (see Chapter 6.4).

5.2 Proposed method for wall segmentation

From a given DSM, a normalized digital surface model (nDSM) can be generated, using the method described in Arefi et al. (2011). Isolated parts in the nDSM exceeding a size threshold (e.g., > 1000 pixels) are selected as buildings of interest. It is worth noting that these isolated parts of nDSM may describe not only individual buildings, but also building complex with courtyards. They may even include several buildings which are located very close to each other and cannot be distinguished by the method described in Arefi et al. (2011). These isolated parts of nDSM are the input data for the wall segmentation in this section.

The method for decomposing individual building model into separate wall segments is as follows (see example in Fig. 5.1 and flowchart in Fig. 5.2):

1. Gradient magnitude (Fig. 5.1b) and gradient direction (Fig. 5.1c) maps are generated using a Sobel filter and are processed with a median filter.
2. A height threshold value is calculated in the neighborhood (3x3 patch) of the pixel with the highest gradient magnitude, which equals to the mean value of the maximal and minimal height in the patch.
3. After extracting all height values above the height threshold (Fig. 5.1d), the building boundary polygons (with 1 pixel width) are generated (using Matlab function bwboundaries). These boundary polygons may describe building outside walls, courtyards, and walls of different building blocks.
4. For every boundary polygon, the corresponding gradient direction values are extracted. A strong variation of the gradient direction along the polygon indicates a corner of the building. The boundary polygon is then separated at these corner pixels into boundary segments (Fig. 5.1e).
5. The boundary segments with 1 pixel width are enlarged using the pixel neighborhood (dilation of 3 pixels) and similar gradient direction (difference smaller than 30°), resulting in wall masks for the building façades.
6. The wall masks are fused into a wall map (Fig. 5.1f) as output, in which pixels of one wall model share the same integer value. Besides, different wall parameters are generated which are useful for choosing walls of interest (median gradient direction, length, height) and for wall layover conversion (median gradient direction, position of the wall center point). Since the wall model gradient direction is also the horizontal component of wall normal direction, the word "gradient direction" in this thesis means also the wall normal direction in physics.

Due to the height threshold in the second step, boundaries of low building parts will not be detected in this approach. However, this limitation is not major as façades with low height will trigger only a low number of signatures in the SAR images. The suggested threshold value for strong variations of the gradient direction in step 4 is 30 degrees, which works for most of the rectangular buildings.

(a)   (b)   (c)

(d)   (e)   (f)
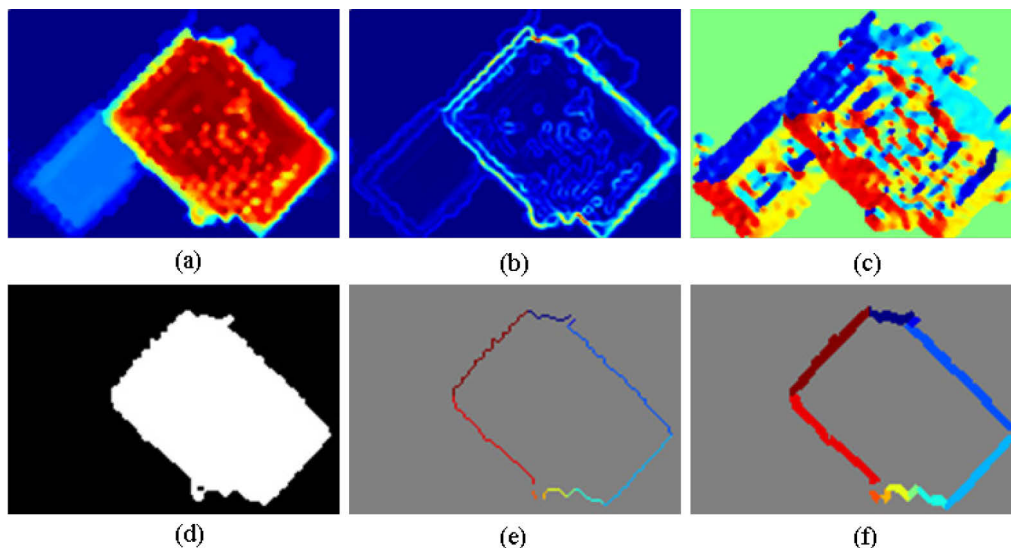
Fig. 5.1: Separation of building walls (DSM parts) for an individual building: (a) building extent in DSM, (b) gradient magnitude map, (c) gradient direction map, (d) building model after applying the height threshold, (e) separated building boundary segments, (f) extracted wall masks, different colors indicate different wall masks.
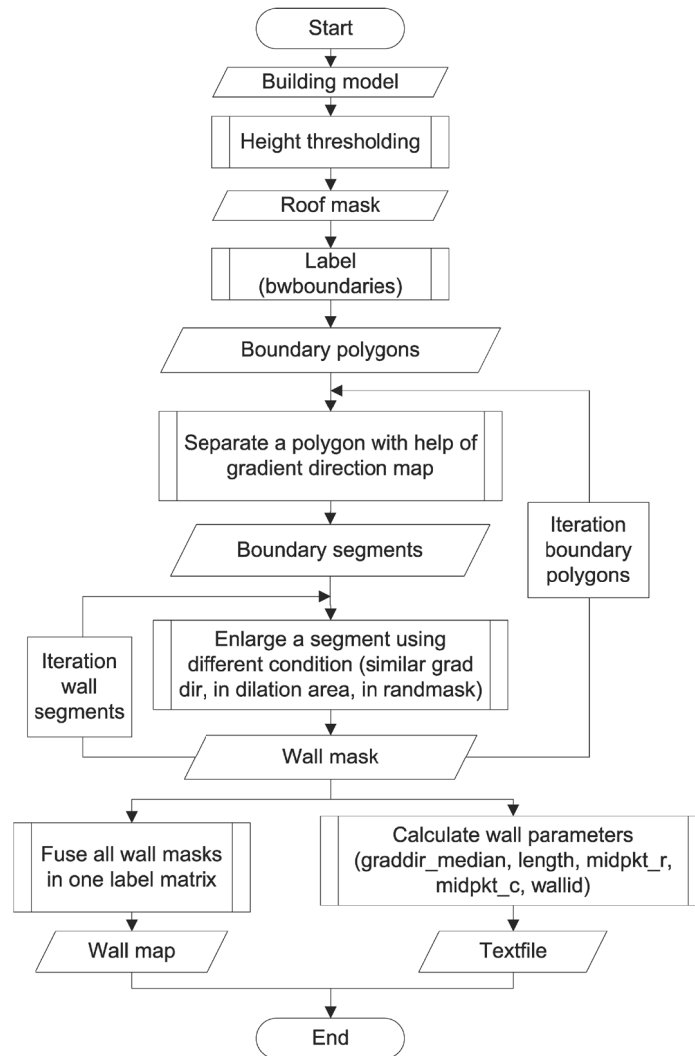
Fig. 5.2: Flowchart of the proposed method for wall segmentation.

The layover areas of the segmented wall models can be generated using the same algorithm as described in Chapter 4. A fusion of local wall layover with layover of DSM can also be performed, in order to provide fused wall layover areas.

5.3 Experimental results

To demonstrate the results of the proposed wall segmentation method, several buildings with different properties are analyzed in this section.

Fig. 5.3 presents the results of two buildings in Munich center. The building in the left of Fig. 5.3 is a small rectangular building with a courtyard. Among the detected nine wall segments from this building, the wall 9 (see the left-bottom image in Fig. 5.3) is oversegmented. This wall part is actually a corner of the courtyard. However, this kind of walls will not affect the application in change detection, since such walls with short length will be discarded (see Section 6.4.1). The color in the bottom images indicates the gradient direction of pixels in degrees. Since the left wall of the left building faces approximately the west direction, the gradient values of pixels according to this wall range between [-180°, -175°] and [175°,180°]. Although these values are displayed with highly different colors in the figures, they are considered as similar gradient direction in the proposed algorithms.
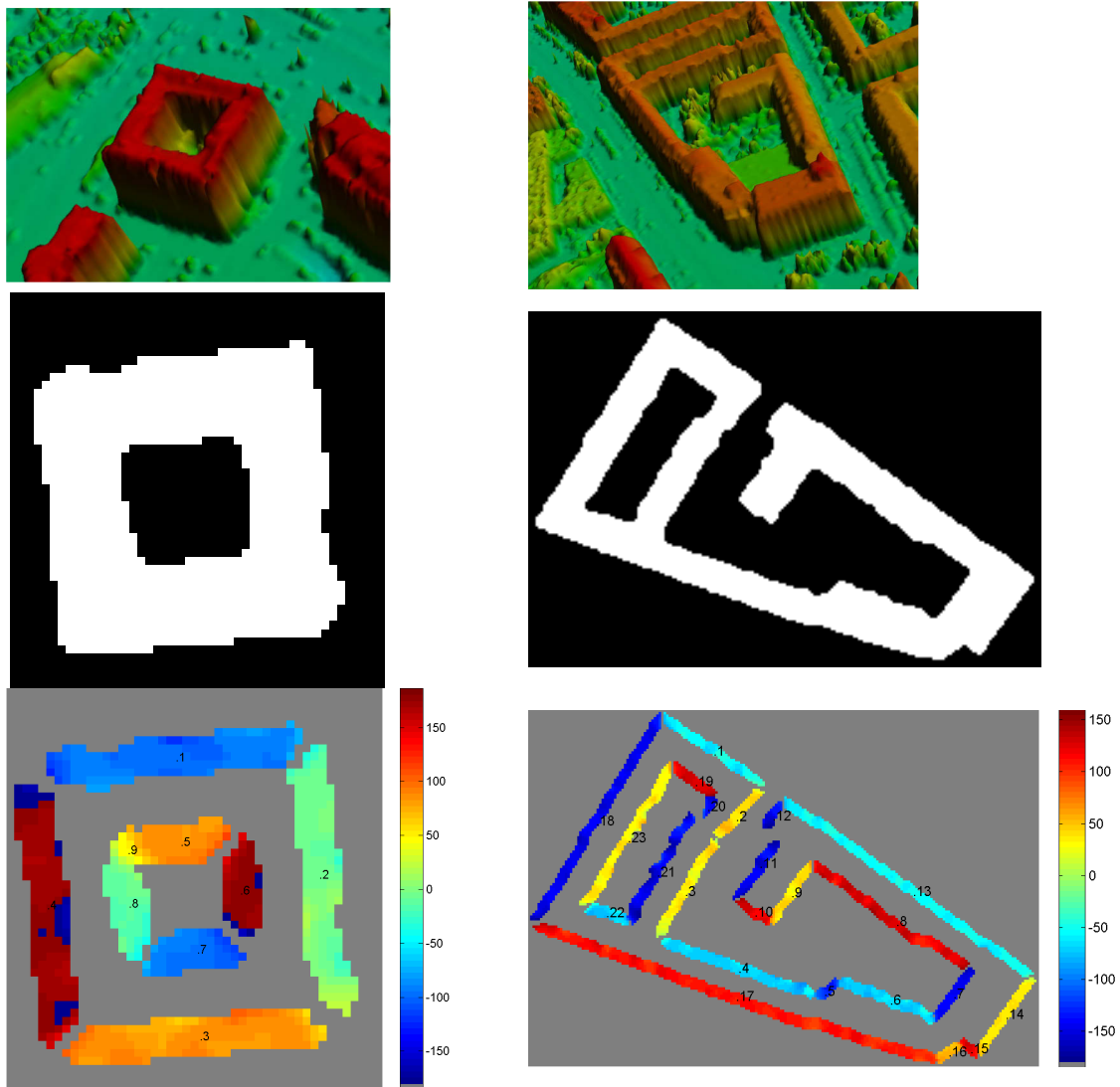
Fig. 5.3: Two buildings with their corresponding results of segmented walls (top to bottom: 3D building model, roof mask, segmented walls with wall IDs and colors for gradient direction in degree).

The building in the right of Fig. 5.3 is a large building complex with a courtyard. Altogether 23 wall segments are extracted from it. Most of them are reasonable. Some of them seem to be oversegmented. For example the walls 2 and 3 as well as the walls 20 and 21 (see right bottom image in Fig. 5.3) actually belong to one building façade part, respectively, but they are recognized as individual walls by the proposed algorithm. This is mainly due to the strong variation of the local gradient direction along the walls. Besides, the wall segment between wall 11 and 12 is discarded since it is too short. These effects will not affect the application in change-detection algorithms, since all wall models with large size are correctly segmented.

(a)   (b)

(c)   (d)
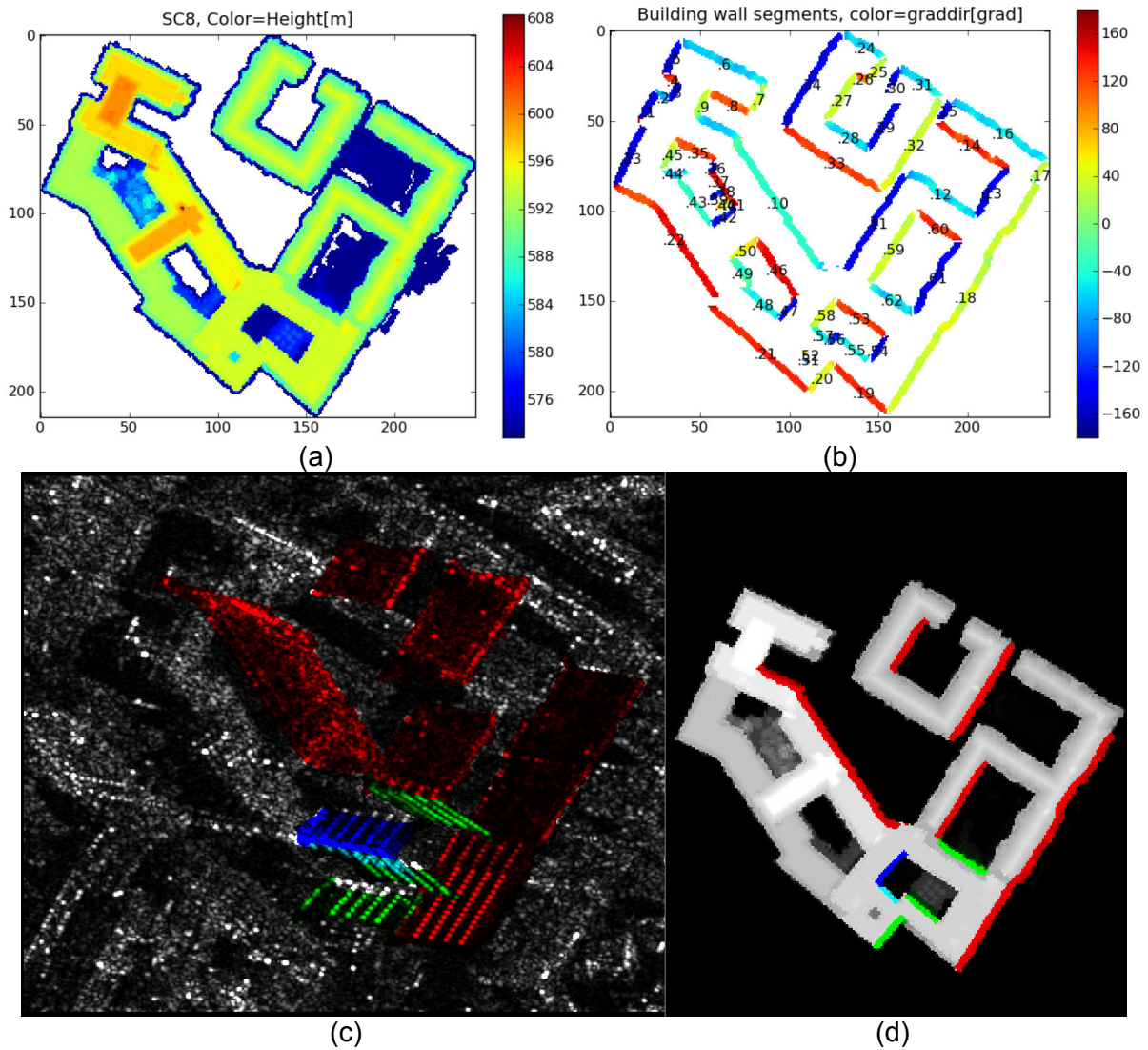
Fig. 5.4: Wall segmentation and identification results of building 8 in Fig. 6.16a in Munich. (a) building model; (b) segmented walls with wall IDs, colors represent gradient direction in degree; (c) layover areas of several walls superimposed on TerraSAR-X image and their corresponding masks in the building model (d), different colors indicate different building walls in the images.

Table 5.1: Parameters of several walls of the building in Fig. 5.4

Wall ID	Median gradient direction [°]	Wall length [m]	Position of the wall center point		Building part	Courtyard	Median roof height [m]	Standard deviation of height [m]	Wall height [m]
			row	column					
18	33,0	150,0	148,6	198,8	1	0	588,3	1,4	15,4
20	43,1	18,4	193,6	118,4	1	0	593,2	2,6	20,3
32	33,4	59,1	63,8	170,0	2	0	588,7	1,2	15,9
58	43,2	17,0	158,5	120,1	1	1	592,8	3,0	20,0
61	-140,7	46,3	137,3	182,6	1	1	589,1	1,1	16,2
62	-55,5	27,5	149,9	157,7	1	1	589,9	1,2	17,1

In Fig. 5.4, detailed results of another building in Munich are presented. The building model and its segmented walls are shown in Fig. 5.4a and Fig. 5.4b, respectively. Several selected segmented walls are marked with different colors in Fig. 5.4d. Their corresponding simulated layover areas are marked with same colors in Fig. 5.4c superimposed on a TerraSAR-X image. This building complex includes actually two close-located buildings with four courtyards. Altogether 62 wall models are segmented from it. Among them, five walls, which contribute the largest layover areas in the corresponding SAR image in Fig. 5.4d, are marked with red color. Several other walls, which lead to interesting point patterns, are marked with different colors (green, cyan, and blue) in the SAR image. It can be recognized that layover areas of different walls (e.g., 55 and 18) may be overlapping.

Different wall parameters are estimated during the processing. Parameters of several walls are listed in Table 5.1. The wall model gradient direction is also the horizontal component of wall normal direction, which is defined as the clockwise angle from the east direction. The position of the wall center point is defined in the DSM image pixel coordinate. Some parameters (median gradient direction, wall length, wall height) are important for the wall selection in change-detection algorithms (see Section 6.4.1). Some parameters (median gradient direction, position of the wall center point) describe the wall vertical plane, which is important for the wall layover conversion (see Section 6.4.1). Besides of these parameters, other parameters provide additional information of the walls. "Building part" indicates which walls belong to the same building part. "Courtyard" marks the walls of courtyards with value "1". "Median roof height" and "Standard deviation of height" stand for the median value and standard deviation of the absolute heights (ellipsoidal heights) of wall pixels. Walls with large standard deviation of height may include different façade patterns. This information might be relevant for the pattern analysis in SAR images (e.g., Auer et al. 2012).

5.4 Summary

In this chapter, a wall segmentation algorithm for wall identification in SAR images is presented. Different from other modeling techniques in literature, the proposed method extracts wall masks in the DSM and uses a triangulated mesh of this DSM part as wall model.

In this context, two limitations are discussed. Firstly, the triangulated mesh described walls are not perpendicular to the ground. On one side, this will lead to a slightly smaller wall layover area. On the other side, it is easier to estimate the wall normal direction. Secondly, small walls with low height may be discarded by the thresholding step. As discussed before, this will not affect the application in change detection, since the neglected walls will trigger only a minor number of signatures in the SAR images.

Despite these limitations, the proposed method extracts DSM parts as wall models, which makes the fusion of wall layover and DSM layover possible. Besides this, many relevant parameters of walls are estimated, which are important for the wall selection and conversion steps in the change-detection algorithms (see Section 6.4).

6   Change detection

The simulator GeoRaySAR is introduced in chapter 3 and used for object identification in chapter 4 and 5. Based on GeoRaySAR and the object identification techniques, five change detection methodologies are developed and presented in this chapter. Section 6.1 introduces the state of the art of SAR change detection techniques and their application for damage assessment. In Section 6.2, the algorithms by comparing LiDAR and SAR data to detect increased backscattering and demolished buildings are presented. For comparing SAR images with different incidence angles, three algorithms are introduced in Section 6.3-6.5, separately. The comparison and combination of all the proposed change detection methods is presented in Section 6.6.

6.1   State of the art: SAR (and multi-modal) change detection

In remote sensing, change detection is the process of identifying changes on the earth surface by jointly analyzing two (or more) images of the same geographical area acquired at different times (Bruzzone and Bovolo, 2013). The techniques of change detection have been widely applied in different remote sensing fields, like urban planning, city expansion monitoring, agricultural surveying, natural resource monitoring, natural hazard prevention and damage assessment. Thanks to the remote sensing data acquired by different sensors (optical, LiDAR, SAR) on different platforms (airplanes, satellites), many change-detection techniques have been developed and presented in literature. Some of the techniques have been summarized and classified in Singh (1989), Lu et al. (2004), and Radke et al. (2005). A framework is proposed in Bruzzone and Bovolo (2013) that aims at defining a top-down approach to the design of novel change-detection systems for multi-temporal VHR images.

Generally, optical sensors have been extensively exploited for change detection approaches. This is due to the long history of satellite optical sensors since the launch of Landsat in 1972. Besides this, optical data is easier to interpret for human eyes. In contrast, the satellite SAR sensor has only existed since the launch of ERS-1 in 1991. The SAR images are difficult to understand because of their intrinsic speckle phenomenon and geometric distortions.

However, the SAR sensor is insensitive to atmospheric conditions (e.g., clouds) and the absence of solar illumination. This makes it highly attractive from the operational viewpoint. Especially in urgent cases like earthquakes, SAR might be the first and only available data for damage assessment, which is very important for rescue teams.

In the literature, extensive work has been done in the area of SAR change detection. The change detection is mainly based on two steps. The first step is to generate a difference image (or data) by using specific comparison operators. In this difference image (or data), the changed regions (pixels or masks) should be easily distinguishable from the unchanged regions (including uninteresting changed regions). The second step is to analyze the difference image (or data) using supervised or unsupervised methods, to generate a binary change-detection map. This step could be considered as a classification or clustering process, where the difference image (or data) of step one is classified into two classes (changed, unchanged) or three classes (unchanged, positive change, negative change). The methods of these two steps are discussed in Section 6.1.1 and 6.1.2, respectively. In Section 6.1.3, articles for change detection using SAR and ancillary data are presented. Section 6.1.4 gives a brief view of change detection for earthquake damage assessment. Section 6.1.5 presents the most related work on simulation based SAR change detection.

6.1.1 Comparison operators of SAR change detection

This section summarizes the different comparison operators used for SAR change detection. Based on the analysis domain and the level of detail, the comparison operators can be roughly differentiated into three classes: pixel-level analysis in the spatial domain, analysis in the wavelet domain, primitive-level analysis (see Table 6.1).

Table 6.1: Comparison operators of SAR change detection

pixel-level spatial domain	rationing	Bazi et al. (2005); Bovolo and Bruzzone (2007)
	local correlation	Matsuoka and Yamazaki (2004); Stramondo et al. (2006)
	similarity measure (Kullback-Leibler divergence)	Inglada and Mercier (2007); Luo et al. (2012); Cui and Datcu (2012)
wavelet domain		Bovolo and Bruzzone (2005); Celik (2009); Schmitt et al. (2009)
primitive-level		Gamba et al. (2006); Brett and Guida (2013)

Three types of comparison operators fall into the pixel-level analysis in the spatial domain: image rationing, local correlation, and similarity measurement.

Image rationing is the basic and most popular comparison operator. In SAR image analysis, the ratio image is usually expressed in a logarithmic scale. With this operation the residual multiplicative speckle noise can be transformed into an additive noise component. The log-ratio operator was used in Bazi et al. (2005); Bovolo and Bruzzone (2007). This operator compares only the corresponding pixel values, so that it is sensitive to the miss-registration error, noise and speckle.

The local correlation operator compares the adjacent area of a pixel using the pixel correlation. A high correlation indicates a low possibility of change. Based on this idea, Matsuoka and Yamazaki (2004) compared the backscattering coefficient and intensity correlation of two SAR images. Grid-cell correlation was used in Dekker (2011). This idea was extended in Stramondo et al. (2006) by comparing the difference of intensity correlation, which used three images as input data.

Another important and interesting operator is based on a similarity measurement and compares the local statistics. To this end, the Kullback-Leibler (KL) divergence (Kullback and Leibler 1951) as a similarity measurement was used. This idea was used in Inglada and Mercier (2007) for SAR change detection in spatial domain. The local statistics are estimated by cumulant-based Edgeworth series expansion, which approximates the probability density functions (PDF) in the neighborhood of each pixel in the image. Luo et al. (2012) used the same idea and classified the KL results into three classes. The KL divergence was used in Cui and Datcu (2012) in wavelet domain to model the subband statistics.

Another class of comparison operators is "analysis in wavelet domain". Wavelets can distinguish horizontally and vertically aligned features in SAR images. Bovolo and Bruzzone (2005) used the two-dimensional discrete stationary wavelet transformation (2D-SWT) to generate a multi-scale decomposition of the log-ratio image aiming at achieving different levels of representation of the change signal. Each scale is characterized by a different tradeoff between speckle reduction and preservation of geometrical details. Celik (2009) extracted feature vectors by using the subband of the undecimated discrete wavelet transformation (UDWT) decomposition of the difference image. Being an extension of the

wavelet concept, the curvelet coefficients describe ridge-like structures in the images. The curvelet decomposition turns out to be an effective way to describe urban scenes in SAR images, as most SAR signatures of urban areas are composed of linear elements of an arbitrary orientation (Schmitt et al. 2009).

The third class of comparison operator is primitive-level comparison. Different from the pixel or pixel-neighborhood analysis, the primitive-level analysis includes a step of geometrical primitive extraction. Gamba et al. (2006) extracted the linear features from two SAR images. The unmatched linear features confirmed the pixel-based change detection. In Brett and Guida (2013), double bounce lines were extracted for detecting damaged building structures.

6.1.2 Analysis of the difference image

The different comparison operators provide difference images or data. Usually, the difference image has the same size as the original input image. Every pixel contains a difference value, which could be intensity ratio, feature vector distance or dissimilarity. In difference data, every region (e.g., grid cell, patch, object mask, or manual defined region) has one difference value. To generate a binary change map associated with changed and unchanged classes from the difference image, many analysis methods have been developed. Generally, two main approaches to the analysis of difference image have been proposed: the supervised approach and the unsupervised approach. These approaches and some example articles are summarized in Table 6.2.

Table 6.2: Analysis techniques of the difference image

Supervised approaches	Classification	Support Vector Machine (SVM)	Huo et al. (2010)
		Neural network	Longbotham et al. (2012)
	Manual trial-and-error threshold selection		Bovolo and Bruzzone (2005)
Unsupervised approaches	Thresholding	Expectation-Maximization (EM) Dempster et al. (1977)	Bruzzone and Prieto (2000); Bazi et al. (2007); Bovolo and Bruzzone (2007)
		Kittler-Illingworth (KI) Kittler and Illingworth (1986)	Bazi et al. (2005); Moser and Serpico (2006); Ban and Yousif (2012)
	Contextual information	Markov Random Field	Bruzzone and Prieto (2000)
		Fuzzy hidden Markov chains	Carincotte et al. (2006)
		Triplet Markov Field	Wang et al. (2013)
	Clustering		Celik (2009); Luo et al. (2012)

The supervised approach requires the availability of ground truth data in order to derive a suitable training set for the learning process of the classifiers. Huo et al. (2010) used the support vector machine (SVM) for classifying features characterizing changes. A supervised neural network approach was proposed in Longbotham et al. (2012) to exploit both the optical and SAR images for detecting flooded areas. Besides these classification methods, a "manual trial-and-error threshold selection" method was applied in Bovolo and Bruzzone (2005), in order to discriminate changed and unchanged pixels in the difference image. All of these methods are expensive in terms of time because of the providing of training data and the manual work of threshold selection.

The unsupervised approaches do not require a training set and can be performed automatically. Because of this they are more attractive from an operational viewpoint. Based on different assumptions, two kinds of methods were developed.

The first assumption is that the pixel values in the difference image are independent of each other. Under this assumption, an optimal threshold value is selected to minimize the overall error probability in the change-detection process. Two kinds of thresholding methods were presented in the literature: Expectation-Maximization (EM) and Kittler-Illingworth (KI). The EM algorithm (Dempster et al. 1977) is a general approach to maximum-likelihood estimation for incomplete data problems, which requires the estimation of the a priori probability density functions for the classes associated with the changed and unchanged pixels. This algorithm was first used in Bruzzone and Prieto (2000) for change detection, where Gaussian mixture models characterize the statistics in the difference image. This work was extended in Bazi et al. (2007), under the assumption that the two classes of pixels follow a generalized Gaussian (GG) distribution. Bovolo and Bruzzone (2007) used a split-based method to detect small changed areas in a large-size image, where the threshold value was selected in a sub-image having high probability to contain changes.

The Kittler-Illingworth (KI) algorithm (Kittler and Illingworth 1986) aims at minimizing the probability of classification error based on Bayesian decision theory. Bazi et al. (2005) applied this threshold selection criterion with generalized Gaussian modeling of distributions of different classes in SAR images. Moser and Serpico (2006) used different distribution models (log-normal, Nakagami, Weibull) for this technique. Ban and Yousif (2012) developed a modified ratio operator and also applied this thresholding (KI) algorithm.

Another technique takes into account the spatial-contextual information, under the assumption that a pixel is likely to be surrounded by pixels belonging to the same class. Bruzzone and Prieto (2000) used the Markov Random Fields (MRF's) to exploit interpixel class dependency contexts. Carincotte et al. (2006) applied a fuzzy hidden Markov chain for the unsupervised change detection on SAR images. Wang et al. (2013) proposed a change detection method based on triplet Markov Field (TMF), where the third field represents texture similarities of the corresponding pixels in SAR images.

If a feature vector, instead of one value, represents the change indicator of every pixel, a clustering method is needed for the change detection approach. Celik (2009) conducted k-means clustering on feature vectors, which are extracted using the subband of the undecimated discrete wavelet transformation decomposition of the difference image, for unsupervised change detection. Luo et al. (2012) clustered the KL coefficients into 3 classes using graph cut optimization.

6.1.3 Change detection using SAR and ancillary data

The previous sections summarize the change-detection techniques using only SAR images as input data. Sometimes, exploiting ancillary data (e.g., GIS data, optical imagery, LiDAR data) may help the interpretation of the change-detection results, and improve the accuracy and robustness of these results. A summary of change-detection techniques based on SAR and ancillary data is provided in this section.

Ehrlich et al. (2009) used a pre-event optical image to manually interpret changed buildings in a post-event SAR image. Balz and Liao (2010) used building models to present the appearance of collapsed buildings in high-resolution SAR images. This kind of technique depends on the analyst expert. Thus it is of limited interest for operational performance.

In some articles pre- and post-event optical images were used as ancillary data. Stramondo et al. (2006) extracted different features from optical and SAR multi-temporal images, and exploited combined feature classification to detect changed areas. Chini et al. (2009) proposed a change-detection algorithm based on mathematical morphology of optical images, and the decrease of pre- and co-seismic intensity correlation of SAR images, for damage level assessment. In Longbotham et al. (2012), different supervised and unsupervised classification methods exploiting optical and/or SAR data for detecting flood areas were presented. In Dell'Acqua et al. (2011), optical images were used to distinguish between damage and non-damage classes, while SAR texture features could better distinguish between low and heavy damage at block scale.

A very interesting approach for very high resolution building change detection was presented in Barthelet et al. (2011). Rectangular buildings were extracted from optical and SAR images respectively. The derived building parameters were then compared for building change detection. Despite the limitations of automatization, this kind of technique indicates another technical tendency to develop meter-resolution spaceborne remote sensing change detection in future.

6.1.4 Change detection for earthquake damage assessment

As one of the most important applications of change-detection techniques, earthquake damage assessment has been widely presented in the literature. This application is also one main motivation of the later proposed change-detection techniques in this dissertation. In this section, a brief view of change detection for earthquake damage assessment will be presented.

Table 6.3: Articles for earthquake damage assessment

Earthquake events	Articles
Kobe 1995	Matsuoka and Yamazaki (2004)
Bam 2003	Gamba et al. (2007); Chini et al. (2009)
Wenchuan 2008	Brunner et al. (2010a); Balz and Liao (2010); Tong et al. (2012)
L'Aquila 2009	Dell'Acqua et al. (2011)
Haiti 2010	Dekker (2011); Wang and Jin (2012); Brett and Guida (2013)

Table 6.3 presents some articles for damage assessment by exploiting remote sensing data in different earthquakes since 1995. The damage assessment products presented here tend to be more detailed, ranging from grid-cell damage level assessment (Matsuoka and Yamazaki 2004) to building-level analysis (Brett and Guida 2013).

As a recently published article, Dell'Acqua and Gamba (2012) reviewed the techniques and data used to evaluate earthquake damage and presented some open issues for damage assessment collaboration. This paper mentioned the damage level, which was also described in Dekker (2011). The damage level is generally classified according to a seismic scale such as the European Macroseismic Scale 1998 (EMS-98) (Gruenthal 1998). In this dissertation, only the grades 4 and 5 of the EMS-98 building damage scale are of interest, which refer to "partial structural failure of roofs and floors", and "total or near total collapse", respectively. Moderate structural damage might be partially or totally invisible to space-borne SAR sensors.

6.1.5 Most related work: simulation-based SAR change detection

The most related work according to the subsequent proposed techniques is the simulation-based SAR change detection. In this section, three related articles will be discussed.

Balz (2004) presented the geo-referencing of the simulated images and the real SAR image, and its application in building change detection. To the author's knowledge, this is the first attempt to compare simulated and real SAR images for building change detection. However, the georeferencing based on extracted linear features is potentially more time consuming than the proposed method later, especially for a real-time application like earthquake damage assessment. Besides this, the proposed change detection technique was not really automatic. Instead, only a manual interpretation of intensity differences was performed.

Brunner et al. (2010a) published an important article on simulation based SAR change detection. Firstly, building parameters were manually extracted in a pre-event optical image. These building models were then simulated and the simulated images were matched with real SAR images. Finally, normalized mutual information was used to calculate the similarity of the simulated and real SAR images to identify collapsed buildings. This article presented the first application of simulation based method in earthquake damage assessment. However, only isolated rectangular buildings were considered. The manual measuring of building parameters from the optical images is a further limitation.

Wang and Jin (2012) proposed a very similar technique to Brunner et al. (2010a). Additionally, the buildings were simulated under different situations (i.e., unchanged, collapsed, subsided, or deformed) and analyzed.

All the techniques proposed in the three articles are limited by co-registration errors of simulated and real SAR images. The procedure proposed later in this dissertation (Section 6.2-6.5) will focus on fully automatic techniques, which do not need manual extraction of building parameters, work for all kinds of buildings, and provide detailed building change-detection results.

6.2 LiDAR-SAR change detection

Most of the existing articles about SAR change detection require both pre- and post-event SAR images. However, a pre-event SAR image is not always available. Thanks to more and more high resolution airborne or spaceborne remote sensing sensors, 3D surface models can more frequently be derived from LiDAR point clouds or optical stereo matching. Change detection between these two data sets (pre-event DSM, post-event SAR) may enable a fast analysis of disaster damage or city expansion.

This section presents a novel method for detecting changes between LiDAR and SAR data. The connection between DSM and SAR is established by the SAR simulation technique introduced in Chapter 3. As the focus of the simulation algorithm is on geometrical correctness, the comparison is not carried out between simulated and real intensities using the traditional differencing or rationing of image intensities. Instead, the geometric information provided by the simulated images is used. Section 6.2.1 will discuss the effects of building changes in SAR images. Section 6.2.2 presents a pixel-based thresholding method to detect the positive changes. To detect demolished or rebuilt buildings, the comparison operators normalized-mutual-information and joint-histogram-slope are used, which are presented in Section 6.2.3 and Section 6.2.4, respectively. The comparison and combination of these two operators is discussed in Section 6.2.5. Section 6.2.6 describes the

data set of Munich. The experimental results are presented in Sections 6.2.7 - 6.2.10, according to the methods described in Sections 6.2.2 - 6.2.5, respectively. Part of this section appears in Tao et al. (2011b).

6.2.1 Effect of building changes in SAR images

The simulation results provide four layers (shadow, ground, layover and double bounce) (see Chapter 4). If there is no change within the scene between the LiDAR and SAR acquisition dates, SAR image pixels in the shadow and ground layers should be mainly characterized by low intensity, whereas the layover and double bounce layers are mainly covered by pixels with high intensities.

If an isolated building (i.e., building located in the area f of all surrounding buildings in Fig. 4.2) is changed, the corresponding backscattering will decrease and increase in different areas, as illustrated in Fig. 6.1. A positively changed building (new building) leads to a new layover area (increased backscattering) and a new shadow area (decreased backscattering), while a negative changed building (total collapsed building or demolished building) leads to disappeared layover and shadow areas (decreased and increased backscattering, respectively).

However, these theoretical changes of backscattering might not be easy to distinguish. The example in Fig. 6.2 presents histograms of SAR image intensities in three simulated layers. The x-axes denote the logarithmic intensity. As we can see, the three histograms have a big overlap area. This means it is hard to distinguish the three classes of intensities based only on the pixel values.
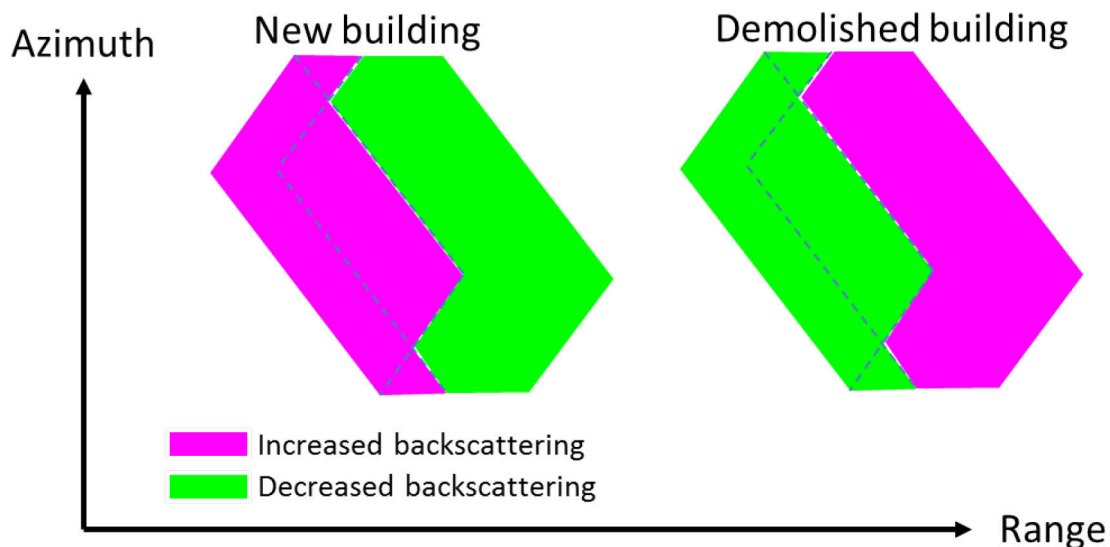
Fig. 6.1: Changed buildings lead to decrease and increase of backscattering in different areas.
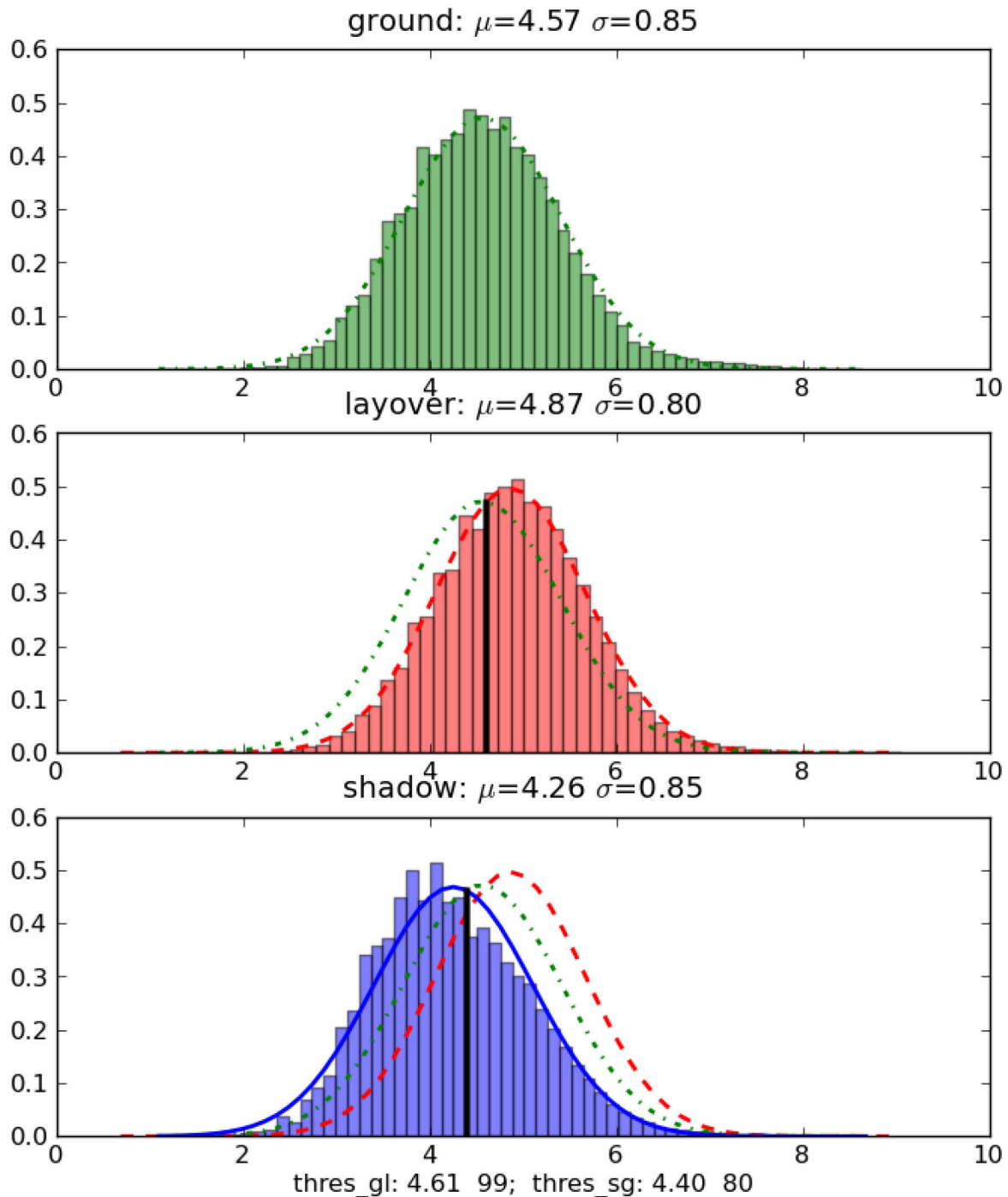
Fig. 6.2: Histogram of image intensities in three layers (ground, layover and shadow) for an example SAR scene with the estimated lines of Gaussian distributions.

If a building is affacted by adjacent buildings, the analysis becomes more complicated. Fig. 6.3 illustrates four new buildings near Building A. The hidden Building B2 leads to no change. The layover of B3 is mixed with the layover of Building A. Only Building B4 and B5 lead to significantly increased backscattering. The Building B5 is isolated to the Building A, whereas the layover of B4 is mixed with the shadow of Building A.
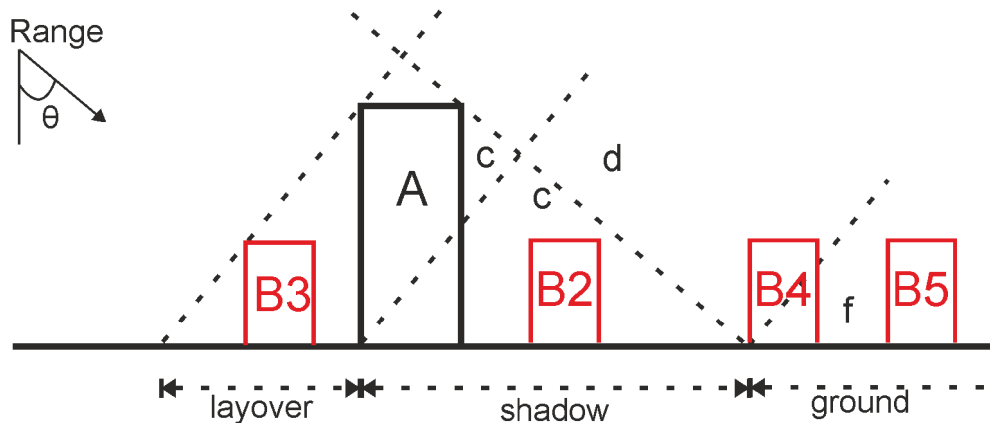
Fig. 6.3: Four new buildings near building A lead to different changes of backscattering in the image (B2 leads to no change; B3 lead to fused layover with A; B4 and B5 lead to increased backscattering in old shadow and ground layers, respectively).

6.2.2 Pixel-based positive change detection

This section focuses on the positively changed (new) isolated buildings (e.g., Building B5 in Fig. 6.3), including some affected buildings (e.g., B4 in Fig. 6.3). A positive changed building may lead to increased (layover) and decreased (shadow) backscattering in different areas. However, the decreased backscattering (backscattering changed from ground to shadow layer) is normally not significantly differentiable, as the shadow and ground layers have similar backscattering in SAR images (see Fig. 6.2). The increased backscattering in the old layover areas is mixed with other building backscattering. Therefore, this increased backscattering is difficult to distinguish and not considered in this section. The increased backscattering in shadow and ground layers is normally very clear, since a building backscattering is normally significantly higher than the shadow and ground backscattering.

Based on this idea, in this section, a method to detect the positive changes between LiDAR and SAR data is proposed. Fig. 6.4 presents the flowchart of the algorithm. The detailed steps of the change-detection algorithm are described as follows.

1. Generation of the different layers (shadow, ground, layover, and double-bounce) of the DSM using the different simulated images (see method described in Section 4.1). In this dissertation, the shadow and ground layers together are called "dark layer", while the layover and double-bounce layers are referred to as "bright layer".
2. Determination of two threshold values which can distinguish the weak and strong bright signals (building backscattering of layover and double-bounce layers) from the dark signals (shadow and ground backscattering) by analyzing the corresponding SAR signal statistical distribution in different layers. The detailed thresholding algorithm is described later in this section.
3. Thresholding the SAR image into mask T1 (with low threshold value) and T5 (with high threshold value).
4. Merge the shadow and ground layer into mask M1. Reduce M1 to M2 using morphological binary erosion (with four iterations in this dissertation). This eroded mask M2 exhibits smaller area and is thus less sensitive to LiDAR model errors (e.g., geocoding error, vertical wall error), especially in the boundaries of the layover layer.
5. Merge the masks T1 and M1 into mask Bw, which denotes the weakly changed area. Merge the masks T5 and M2 into mask Bs, which denotes the strongly changed area. Filter Bw and Bs with median filter to reduce the noise.
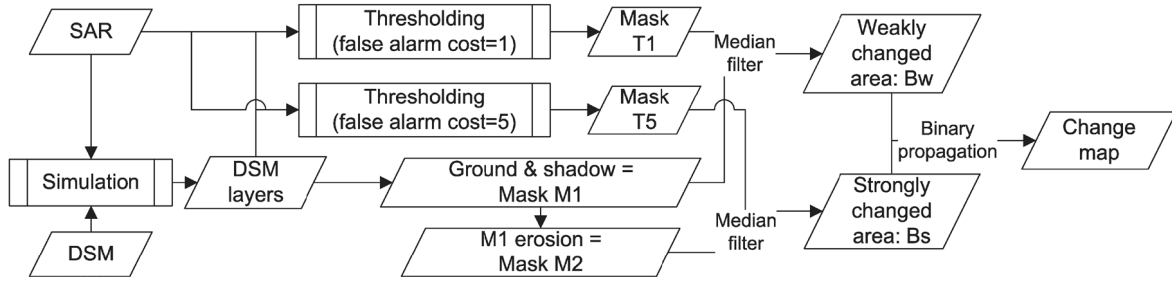
Fig. 6.4: Flowchart of pixel-based detection of positive changes between LiDAR and SAR data.

6. Enlarge Bs in consideration of Bw by binary propagation, so that the neighboring pixels of Bs in the mask Bw will also be considered as "change". This result mask is also called "change map".

The high threshold value of T5 and the reduced mask M2 ensure the low false-alarm-rate of Bs. However this detected changed area is too small and the "missed hit" regions are large. In comparison, the "missed hit" regions in Bw are small but the correctness is moderate. This is mainly owing to the similar backscattering of trees, streets and some buildings with specific types (rough) and materials of surfaces. The binary propagation of Bs improves the correctness and reduces the "missed hit" areas.

Thesholding of SAR image to distinguish bright and dark signals

To find a proper threshold value to distinguish the bright signals from the dark signals in the SAR image, the simulated layers are exploited as apriori information. The SAR values corresponding to the simulated layers are extracted and considered as "training data", in order to estimate the distribution parameters of different layers. Based on the Bayesian decision rule, the "minimization of total expected cost" (also called "minimum risk decision rule" in Duda et al. 2001) is used to distinguish bright from dark signals:

for a pixel with value Y_i, decide for ω_b,

if $p(Y_i \mid \omega_b)p(\omega_b)(C_{bd} - C_{bb}) > p(Y_i \mid \omega_d)p(\omega_d)(C_{db} - C_{dd})$, otherwise decide for ω_d. (6.1)

Where ω_b, ω_d denote the bright (layover and double-bounce) and dark (shadow and ground) classes respectively; $p(Y_i \mid \omega_b)$ and $p(Y_i \mid \omega_d)$ are the conditional distributions of pixel values for bright and dark layers, $p(\omega_b)$ and $p(\omega_d)$ are the prior probabilities of bright and dark values with $p(\omega_b) + p(\omega_d) = 1$; $C_{bb}, C_{dd}, C_{bd}, C_{db}$ denote the costs of four decisions: "correct decision of bright signal", "correct decision of dark signal", "missed hit", and "false alarm", respectively. The distribution parameters $p(Y_i \mid \omega_b)$, $p(Y_i \mid \omega_d)$, $p(\omega_b)$ and $p(\omega_d)$ are derived from the training data.

The Equation (6.1) is equivalent to find a threshold T with $p(T \mid \omega_b)p(\omega_b)(C_{bd} - C_{bb}) = p(T \mid \omega_d)p(\omega_d)(C_{db} - C_{dd})$ and the decision rule is given by:

for a pixel with value Y_i, decide for ω_b if $Y_i > T$, otherwise decide for ω_d. (6.2)

Normally the decision-costs $C_{bb} = C_{dd} = 0$, which means no cost for correct decisions. Since only the ratio C_{bd} / C_{db} plays a role for the calculation of the threshold values, one can fix one (the missed-hit decision cost $C_{bd} = 1$) and vary the other (the false-alarm decision cost C_{db}). The higher the false-alarm decision cost C_{db} is, the bigger is the threshold value T. A high threshold value leads to a low false-alarm rate and high missed-hit rate. To compensate this effect and find a proper tradeoff between the false-alarm and missed-hit rates, two threshold values are defined instead of one. A small threshold value is calculated by $C_{db} = 1$, which means equal false-alarm and missed-hit costs. This is the common way to find the threshold. Based on experimental tests, a big threshold value is calculated by $C_{db} = 5$ (i.e., the false-alarm-decision-cost is higher than missed-hit-decision-cost), which yields the best results.

The SAR values corresponding to the simulated layers have been used as a kind of "training data". Since the simulated layers correspond to the LiDAR data instead of the SAR image, this training data includes changes between the two acquisition dates. Under the assumption that most areas inside the whole LiDAR data are not changed, this training data can still be used with limited impact. In case the assumption fails, it is suggested to manually choose another unchanged area as training data to find the threshold values.

The distribution parameters $p(Y_i | \omega_b)$, $p(Y_i | \omega_d)$, $p(\omega_b)$ and $p(\omega_d)$ are derived from the training data, which is based on the SAR image distribution properties. As the pixel intensity distribution of high-resolution SAR images in urban areas can be well modeled by the log-normal distribution (Oliver and Quegan 2004), the SAR values are converted to logarithmic values so that their distribution is a normal distribution. The distribution of $p(Y_i | \omega_b)$, $p(Y_i | \omega_d)$ can be defined as $\mathrm{N}(\mu_b, \sigma_b^2), \mathrm{N}(\mu_d, \sigma_d^2)$, where $\mu_b, \sigma_b^2, \mu_d, \sigma_d^2$ indicate the mean and variance of the two normal distributions.

Reason of failed pixel-based negative change detection

The previous steps show a method for detecting positively changed buildings by extracting bright pixels in the shadow and ground layers. Exploiting the layover and double-bounce layers, the same method was tried which is based on the assumption that low intensity pixels indicate negative changes. However, the reflection of the radar signals depends on many different physical parameters (e.g., surface material, roughness), which may be only roughly considered in the simulation steps and are not provided by the LiDAR DSM. Moreover, due to the lack of geometrical information in the 2.5D DSM, no façade signal can be simulated to predict the appearance of salient signatures. To conclude, the amount of apriori knowledge provided by the DSM does not suffice for a generalized pixel-based analysis for negative changes, as there are many false alarms in the change detection result. Hence, an object-based method is needed to solve this problem. To this end, the mutual-information-based method is developed and described in the following section.

6.2.3 Mutual information-based negative change detection

The previous step discusses the failure of pixel-based negative change detection between LiDAR and SAR data. This section will present an object-based method for negative change detection. Instead of considering every pixel individually, an object (building) mask will be generated and all the corresponding pixels inside the mask will be analyzed together to provide a single change indicator value – the normalized mutual information (NMI).
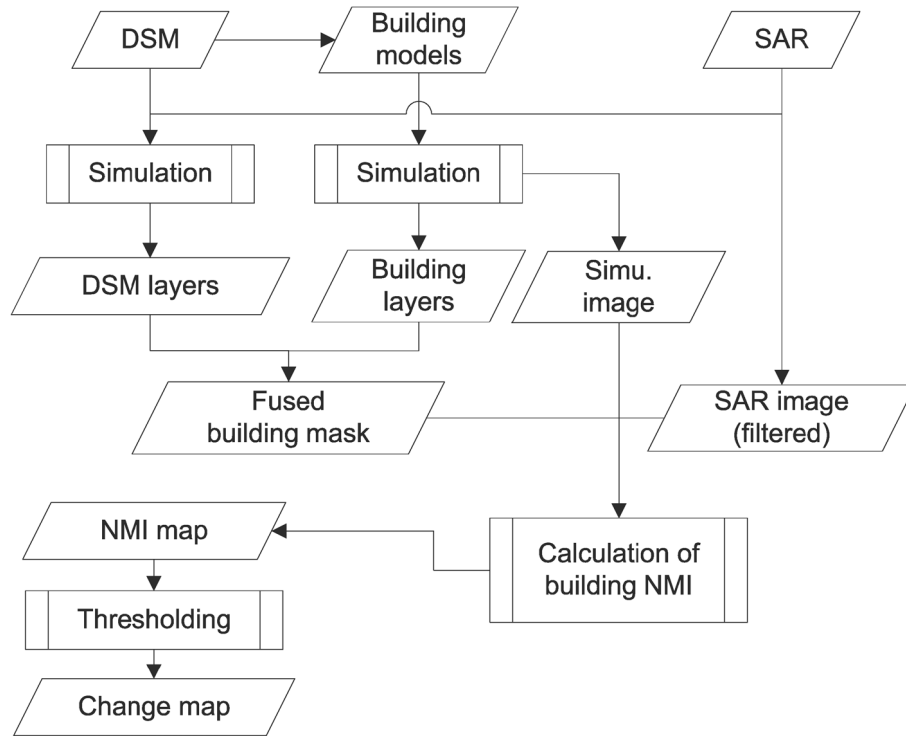
Fig. 6.5: Flowchart of mutual-information-based change detection between LiDAR and SAR data.

Fig. 6.5 illustrates the flowchart of the algorithm. The DSM and individual building models are simulated and their layers are generated and fused (see details in Chapter 3, 4 and 5). For every building, three fused layers are generated (shadow, layover and double bounce), with consideration of neighborhood influences. These three layers together build up a "building mask". The corresponding pixels of the building mask according to individual buildings inside the simulated and SAR image are extracted. These pixel values consist the random variables X_1 and X_2, respectively. These two variables are the input of the following steps for calculating the Mutual information and NMI. The SAR image is suggested to be filtered before to reduce the speckle noise. The non-local filter (Deledalle et al. 2009) without iteration has been used here.

Mutual information (MI)

As a measure derived from information theory, mutual information (Shannon 1948) is based on entropy. Entropy measures the uncertainty in a random variable. The Shannon entropy (Shannon 1948) is defined as

$$H = -\sum p_i \log_2 p_i. \tag{6.3}$$

Where p_i is the probability of the i-th value. For example, if an image contains n different values with the same probability $p_i = 1/n$, the entropy of this image is $H = -n\left[1/n \log_2(1/n)\right] = \log_2 n$, which is equal to a bit value in binary system.
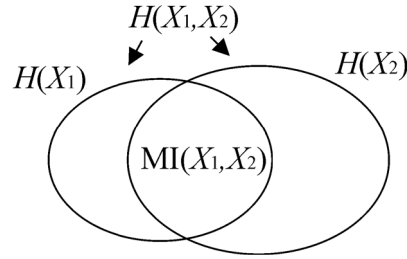
Fig. 6.6: Relationship between entropy, joint entropy and mutual information.

Mutual information (MI) measures the mutual dependence of two random variables. The MI between two random variables X_1 and X_2 (here, pixel values in the images) is defined as

$$
\begin{aligned}
MI(X_1, X_2) &= H(X_1) + H(X_2) - H(X_1, X_2) \\
H(X_1) &= -\sum p(X_1)\log_2 p(X_1) \\
H(X_2) &= -\sum p(X_2)\log_2 p(X_2) \\
H(X_1, X_2) &= -\sum p(X_1, X_2)\log_2 p(X_1, X_2)
\end{aligned}
\tag{6.4}
$$

where $H(X_1)$ and $H(X_2)$ are the entropies of X_1 and X_2, and $H(X_1, X_2)$ denotes their joint entropy. The relationship of these three entropies is:

$$
\max(H(X_1), H(X_2)) \le H(X_1, X_2) \le H(X_1) + H(X_2).
\tag{6.5}
$$

Their relationship is illustrated in Fig. 6.6.

The estimation of MI is mainly based on the joint histogram of the two variables (here: images):

$$
\begin{aligned}
p(X_1, X_2) &= \frac{hist(X_1, X_2)}{\sum hist(X_1, X_2)} = \frac{hist(X_1, X_2)}{length(X_1)} \\
p(X_1) &= \frac{hist(X_1)}{length(X_1)} = \sum_{X_2} p(X_1, X_2) \\
p(X_2) &= \frac{hist(X_2)}{length(X_2)} = \sum_{X_1} p(X_1, X_2)
\end{aligned}
\tag{6.6}
$$

Although the estimated MI derived from the histogram is different from the theoretical definition of MI, the symbol "MI" in this dissertation is used for both of them to ease the understanding. The quantization step size and, hence, the number of bins plays an important role in the calculation of the joint histogram. Too few bins lead to loss of the image information, while too many bins lead to inefficient comparison. The selection of the number of bins is discussed in detail in Suri (2010). It is suggested that the joint histogram has on average at least one entry per bin in Xie et al. (2003). Considering the bin number used in different articles (Brunner et al. 2010; Suri 2010), 128 bins for both the simulated and real SAR images have been tested and chosen, which yields the best comparison results. It is worth noting that the bin number of X_1 and X_2 need not be the same, but their length (here: image size) must be the same.

The MI considers only the occurrence of the same pairs of values in X_1 and X_2. It is not sensitive to the absolute values of X_1 and X_2. That is why it is favorable for multi-modal image matching and comparison.

Normalized mutual information (NMI)

In the upcoming steps, the aim is to distinguish changed and unchanged buildings by evaluating an absolute measurement of the building. This measurement should be invariant to the building size. However, the MI described in the previous section depends on the length of the variable (i.e., the size of the image patch related to a building), which is then dependent on the building size and orientation. Because of this, the normalized mutual information (NMI) is used. Various NMI were proposed in literature. This dissertation works with the three versions of NMI (Saerndal 1974; Joe 1989; Studholme et al. 1999) used in Brunner et al. (2010a), and additionally the version in Strehl and Ghosh (2003):

$$SAE(X_1, X_2) = \frac{MI(X_1, X_2)}{\frac{1}{2}(H(X_1) + H(X_2))}$$

$$JOE(X_1, X_2) = \frac{MI(X_1, X_2)}{\min(H(X_1), H(X_2))}$$

$$STU(X_1, X_2) = \frac{H(X_1) + H(X_2)}{H(X_1, X_2)} = \frac{MI(X_1, X_2)}{H(X_1, X_2)} + 1 \qquad (6.7)$$

$$STR(X_1, X_2) = \frac{MI(X_1, X_2)}{\sqrt{H(X_1) H(X_2)}}$$

The values of SAE, JOE and STR range between [0,1]. The value of STU ranges between [1, 2]. The difference of the four NMI is only the denominator. One can better understand this difference in Fig. 6.6. The reason in Strehl and Ghosh (2003) to use the geometric mean instead of arithmetic mean in the denominator is "because of the analogy with a normalized inner product in Hilbert space".

Expectation Maximization (EM) algorithm

The Expectation Maximization (EM) algorithm is a widely used classification algorithm, representing a general approach to the maximum likelihood estimation for incomplete data issues (Dempster et al. 1977). Bruzzone and Prieto (2000) used it to distinguish the changed pixels in optical remote sensing images, where the Gaussian mixture model characterizes the statistics in the difference image. This work was extended in Bazi et al. (2007) for SAR image change detection, under the assumption that the two classes of pixels follow a generalized Gaussian distribution.

In case of this section, the values to be distinguished are not the image values, but the NMI of buildings. Assuming that the distributions of NMI of both changed and unchanged buildings are Gaussian, the probability density function $p(Y)$ of $Y = NMI$ is modeled as a mixture Gaussian distribution:

$$p(Y) = p(Y \mid \omega_c)p(\omega_c) + p(Y \mid \omega_u)p(\omega_u), \tag{6.8}$$

where $p(Y \mid \omega_c)$ and $p(Y \mid \omega_u)$ are the conditional distributions of NMI for changed and unchanged buildings, $p(\omega_c)$ and $p(\omega_u)$ are the probabilities of changed and unchanged buildings with $p(\omega_c) + p(\omega_u) = 1$. The one-dimensional Gaussian distributions $p(Y \mid \omega_c)$ and $p(Y \mid \omega_u)$ are based on two parameters: mean μ and variance σ^2. They can be derived iteratively using the following equations (Redner and Walker 1984; Bruzzone and Prieto 2000):

$$N_{i,k}^t = \frac{p^t(\omega_k)p^t(Y_i \mid \omega_k)}{p^t(Y_i)}$$

$$p^{t+1}(\omega_k) = \frac{\sum\limits_i N_{i,k}^t}{I}$$

$$\mu_k^{t+1} = \frac{\sum\limits_i N_{i,k}^t Y_i}{\sum\limits_i N_{i,k}^t} \tag{6.9}$$

$$\left(\sigma_k^2\right)^{t+1} = \frac{\sum\limits_i N_{i,k}^t \left(Y_i - \mu_k^t\right)^2}{\sum\limits_i N_{i,k}^t}$$

where t denotes the iteration step; $i \in \{1, 2 \ldots I\}$ denotes the number of buildings with sum I; Y_i denotes the NMI of the buildings; $k \in \{c, u\}$ denotes the changed and unchanged classes.

The initialization of EM can be conducted by choosing two sets of values (Y_{set1} and Y_{set2}) with two thresholds (T_1 and T_2), which is based on the idea in Bruzzone and Prieto (2000):

$$T_1 = \min(Y) + (\max(Y) - \min(Y))\alpha$$
$$T_2 = \max(Y) - (\max(Y) - \min(Y))\alpha, \quad \alpha \in (0, 0.5] \tag{6.10}$$
$$Y_{set1} = \{Y_i \mid Y_i \le T_1\}, \quad Y_{set2} = \{Y_i \mid Y_i \ge T_2\}.$$

The parameters $\mu_k^{\,0}, (\sigma_k^2)^0, p^0(\omega_k)$ are then calculated using these two sets of values accordingly.

Thresholding

The EM algorithm provides five parameters $\mu_c, \sigma_c^2, p(\omega_c), \mu_u, \sigma_u^2$ and $p(\omega_u) = 1 - p(\omega_c)$ of the two classes with Gaussian distribution:

$$p(Y \mid \omega_c) = \frac{1}{\sigma_c \sqrt{2\pi}} \exp\left\{-\frac{(Y-\mu_c)^2}{2\sigma_c^2}\right\} \sim N\left(\mu_c, \sigma_c^2\right)$$

$$p(Y \mid \omega_u) = \frac{1}{\sigma_u \sqrt{2\pi}} \exp\left\{-\frac{(Y-\mu_u)^2}{2\sigma_u^2}\right\} \sim N\left(\mu_u, \sigma_u^2\right) \tag{6.11}$$

Based on the Bayesian decision rule, the maximum likelihood classifier is defined as:

for a building with a NMI of Y_i,

decide for ω_u if $p(Y_i \mid \omega_u)p(\omega_u) > p(Y_i \mid \omega_c)p(\omega_c)$, otherwise decide for ω_c. $\tag{6.12}$

This is equivalent to finding a threshold value T with $p(T \mid \omega_u)p(\omega_u) = p(T \mid \omega_c)p(\omega_c)$. By inserting Equation (6.11), this is equivalent to solving the quadratic equation:

$$(\sigma_u^2 - \sigma_c^2)T^2 + (-2\mu_c\sigma_u^2 + 2\mu_u\sigma_c^2)T + \sigma_u^2\mu_c^2 - \sigma_c^2\mu_u^2 - 2\sigma_c^2\sigma_u^2 \ln\frac{\sigma_u P(\omega_c)}{\sigma_c P(\omega_u)} = 0$$

$$\Rightarrow$$

$$a = \sigma_u^2 - \sigma_c^2$$

$$b = -2\mu_c\sigma_u^2 + 2\mu_u\sigma_c^2$$

$$c = \sigma_u^2\mu_c^2 - \sigma_c^2\mu_u^2 - 2\sigma_c^2\sigma_u^2 \ln\frac{\sigma_u P(\omega_c)}{\sigma_c P(\omega_u)} \tag{6.13}$$

$$T_{1,2} = \frac{-b \pm \sqrt{b^2 - 4ac}}{2a}$$

$$T = \begin{cases} T_1, \text{ if } |T_1\text{-}\sigma_u| <= |T_2\text{-}\sigma_u| \\ T_2, \text{ if } |T_1\text{-}\sigma_u| > |T_2\text{-}\sigma_u| \end{cases} \text{ for } \sigma_c \neq \sigma_u \\ \frac{\mu_c + \mu_u}{2} \qquad \text{ for } \sigma_c = \sigma_u$$

Since a high NMI indicates high similarity of the simulated and real SAR images, the resulting decision criterion is given by:

for a building with a NMI of Y_i, decide for ω_u if $Y_i > T$, otherwise decide for ω_c. $\tag{6.14}$

The EM algorithm and thresholding is illustrated in Fig. 6.7.

μ_1=0.37 σ_1=0.20 P_1=0.38; μ_2=0.61 σ_2=0.09 P_2=0.62; thres=0.45
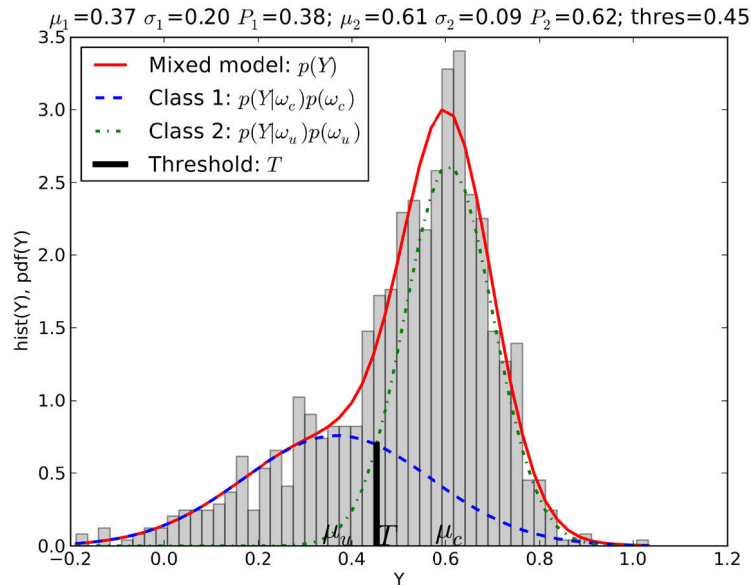
Fig. 6.7: The estimated Gaussian models (plotted curves) and threshold values (vertical dark line) using the Expectation-Maximization (EM) algorithm with building NMI values (Y) as input.

6.2.4 A novel comparison operator: joint histogram slope (JHS)

The previous section presents the comparison operator: normalized mutual information (NMI). NMI considers only the occurrence of the same pairs of values in the input random variables X_1 and X_2 (here, pixel values in the simulated and real SAR images). Hence it is not sensitive to the absolute values of X_1 and X_2 and suitable for multi-modal image matching and comparison. However, "not sensitive to the absolute values" is also a disadvantage of NMI, since the NMI does not consider the increasing or decreasing relationship of the value pairs in X_1 and X_2. For example, if one compares the same image X_1=X_2=X, then NMI(X,X)=1, which means the two input images are highly dependent. In a second situation, let X_2=-X=-X_1, NMI(X,-X)=1. In this case, although X_2 is a monotonically decreasing function of X_1, their NMI is still the same as the first case, since the occurrence of the same pairs of values has not changed. However, for the change detection application discussed in this dissertation, a monotonically decreasing relationship of the simulated and real SAR image means certainly a significant change. Because of this, in some case, NMI will lead to missed hit decisions (see the experimental results in Section 6.2.8).

To compensate this deficit of MI in the application of change detection, and to take into account of the increasing properties of the value pairs in the simulated and real SAR images, a novel comparison operator, the joint histogram slope (JHS), is created.

JHS is the slope of a line that matches best the joint histogram of the simulated and real SAR image patches. JHS describes the increasing relationship of the input value pairs. For an ideal unchanged image pair (X_1=X_2=X), X_2 is a monotonically increasing function of X_1, and their joint histogram slope is "1". If some pixel values in X_2 decrease, the joint histogram slope will be smaller. A negative slope denotes a significant change of the image. This is the basic idea of JHS.

Let X_1 and X_2 denote the corresponding pixel values of a building inside the simulated and real SAR images, respectively. The detailed steps of calculating the JHS of this building is as follows:

1. Radiometric normalization of X_1 and X_2, to make their distribution properties (Histogram) similar.
2. Calculation of the JHS by linear regression using least squares estimation.

Radiometric normalization

To exploit the absolute values of X_1 and X_2 and to provide a JHS with physical meaning, X_1 and X_2 should have similar distribution properties. However, the simulated image and the real SAR image have very different radiometric properties. The real SAR image values (of TerraSAR-X GEC product) range between [0, 65535] (16 bit radiometric resolution). In comparison, the simulated image values (of RaySAR) range between [0, 255] (8 bit radiometric resolution). To compensate these radiometric differences between the two images caused by inconsistencies of acquisition conditions rather than object changes, the SAR image values are first converted to natural logarithmic values. Thereby the multiplicative nature of speckle will be converted to additive. After this, both images are processed with histogram equalization (histeq) separately.

"Histogram equalization" (Acharya and Ray 2005) is an algorithm in image processing of contrast adjustment using the image's histogram. This algorithm usually increases the global contrast of an image. Through this algorithm, the intensities can be better distributed on the histogram.

Let an image (or image patch) with n pixels having pixel values i ranging between [0, 1, …, L-1]. A pixel with value k will be converted to:

$$I_k^{new} = round(I_{max} \sum_{i=0}^{k} \frac{n_i}{n}), \quad k=0,1,...,L-1. \tag{6.15}$$

Where n_i denotes the number of pixels with the value i, n_i/n denotes the probability of i, $\sum_{i=0}^{k} n_i/n$ denotes the cumulative distribution function of k, I_{max} denotes the new image maximum values (here 255).

Under experimental tests, the bin size (radiometric level) has not significantly affected the calculation of JHS. Different values of I_{max} (from 255, 127, to 15) have been tested, they provide a similar JHS, highlighting the robustness of the comparison operator.

The same I_{max} for the histogram equalization of both image X_1 and X_2 is defined, so that the joint histogram is a quadratic matrix with size ($I_{max}+1$, $I_{max}+1$). After the radiometric normalization, the image values X_1 and X_2 are converted to Y_1 and Y_2, respectively.

Calculation of JHS using least square estimation

Let us assume the relationship of Y_1 and Y_2 is linear dependent:

$$Y_2 = \beta Y_1 + \alpha, \text{ where } \alpha \text{ is the intercept, } \beta \text{ is the slope.} \tag{6.16}$$

Using the value pairs Y_1 and Y_2 as input, the two parameters can be derived using the least square estimation:

$$Y_2 = \begin{bmatrix} Y_{2,1} \\ \vdots \\ Y_{2,n} \end{bmatrix} = \begin{bmatrix} Y_{1,1} & 1 \\ \vdots & \vdots \\ Y_{1,n} & 1 \end{bmatrix} \begin{bmatrix} \beta \\ \alpha \end{bmatrix} + e, \quad M = \begin{bmatrix} Y_{1,1} & 1 \\ \vdots & \vdots \\ Y_{1,n} & 1 \end{bmatrix}$$

$$\begin{bmatrix} \hat{\beta} \\ \hat{\alpha} \end{bmatrix} = (M^T M)^{-1} M^T Y_2.$$

(6.17)

Under the assumption of no change, Y_2 should be a monotonically increasing function of Y_1, thus the slope is positive. Because of the radiometric normalization of both images to the range [0,255], the slope should be equal to "1". A decreased pixel value in Y2 will lead to decreasing of the slope. Theoretically, the slope can be any value between $(-\infty, +\infty)$. According to my experience, the slope ranges between (-1, 1.5). Under experimental experience, a negative slope denotes a demolished building. For an unchanged building, the slope ranges between the value (0.5, 1.5). If a slope ranges between (0, 0.5), it is a hint of the building is partly demolished, rebuilt or its roof material is changed.

For the calculation of the slope, the simple linear regression (also called ordinary least square estimation) is used, which is sensitive to outliers. There are some other robust linear regression methods that might fit the line insensitive to outliers. For example, the Theil-Sen estimator (Siegel 1982) chooses the median slope among all lines through pairs of two-dimensional sample points. However, it is difficult to distinguish an outlier caused by observation errors (DSM model error, building position error, influence of trees) from real changes (building change). An "insensitive-to-outlier" method might lead to "missed-hit". Because of this, the simple linear regression has been chosen to let it be sensitive to any change. The false-alarm detection will be removed afterwards by human interpretation or by the combination with other comparison operators.

Relationship of JHS to other comparison operators

The estimated parameter $\hat{\beta}$ slope can also be expressed as (Keeping and Kenney, 1965):

$$\hat{\beta} = \frac{\text{cov}(Y_1, Y_2)}{\text{var}(Y_1)} = r(Y_1, Y_2) \frac{\sigma_{Y_2}}{\sigma_{Y_1}},$$

$$\text{cov}(Y_1, Y_2) = \frac{1}{n} \sum_{i=1}^{n} (Y_{1,i} - \mu_{Y_1})(Y_{2,i} - \mu_{Y_2})$$

$$\text{var}(Y_1) = \text{cov}(Y_1, Y_1) = \sigma_{Y_1}^2$$

$$r(Y_1, Y_2) = \frac{\text{cov}(Y_1, Y_2)}{\sqrt{\text{var}(Y_1)\,\text{var}(Y_2)}}$$

(6.18)

Where μ and σ denote the mean and standard deviation, respectively. The Equation (6.18) presents the relationship of line slope with covariance, variance and correlation coefficient $r(Y_1, Y_2)$. In some articles (Radke et al. 2005), the correlation coefficient has been used as a comparison operator. In comparison with other operators, the main advantage of JHS is its physical meaning.
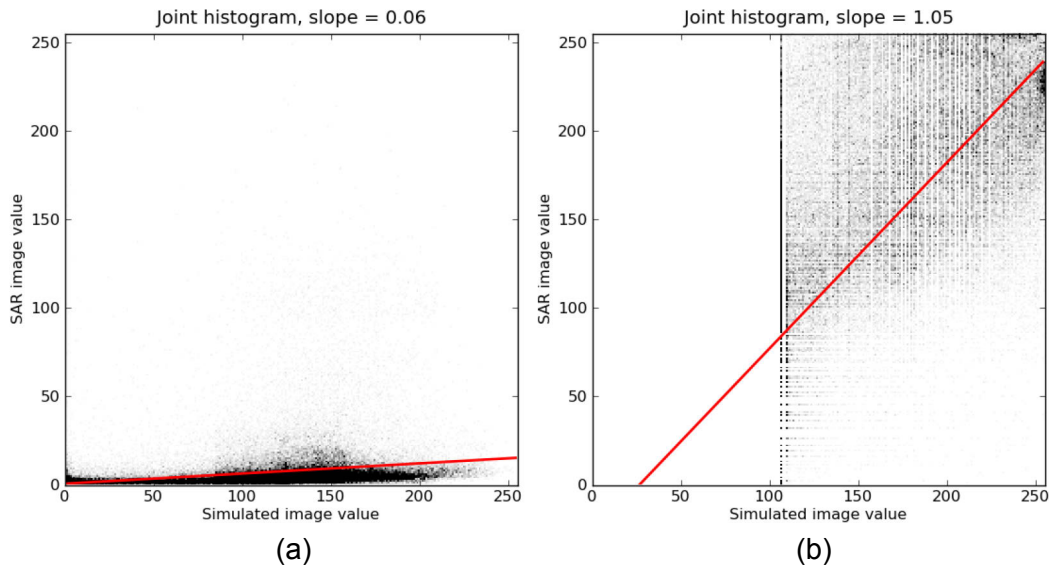
Fig. 6.8: The joint histograms of a building 8 before and after the radiometric normalization. The red lines indicate the estimated lines of the points.

Example of JHS

As expected, the radiometric normalization (especially the histogram equalization) plays an important role in the calculation of JHS. Fig. 6.8 presents the joint histogram of a building 8 (see Fig. 6.16a) before and after the radiometric normalization, using a line indicating the fitted line after simple linear regression.

Because of the low contrast of the SAR image in the low intensity part, Fig. 6.8a shows an insignificant increasing. In Fig. 6.8b, the histogram equalization spreads out the most frequent intensity values in the whole histogram, so a significant slope is distinguishable. It is worth noting that, all the pixels in the shadow area of the simulated image have the same value "0". This leads to a high value (~100) in the left column of the joint histogram in Fig. 6.8b. But this phenomenon has not affected the result significantly.

6.2.5 Comparison and combination of NMI and JHS

The previous two sections have presented two comparison operators: the normalized mutual information (NMI) and the joint histogram slope (JHS). Both of them have potential and limitations. In this section, these two comparison operators are compared and the possibility for the combination of them is discussed.

The comparison of the two operators is presented in Table 6.4. The two operators have similar semantic interpretation (low value denotes change, high value denotes unchanged) but different value ranges. NMI is suitable to multi-modal image comparison but leads to missed-hit in case of a monotonically decreasing relationship. JHS has physical meaning and is easy to distinguish, but it is very sensible to small changes, which might lead to false-alarm caused by DSM errors or influences of neighboring trees. A combination of these two comparison operators may provide a stable and improved result.

Table 6.4: Comparison of normalized mutual information and joint histogram slope

Comparison operators		Normalized mutual information (NMI)	Joint histogram slope (JHS)
Input		The corresponding pixel values of a "building mask" according to individual buildings inside the simulated and real SAR images	
Consideration		Occurrence of same pairs of values	Slope (dependence) of value pairs in the joint histogram
Radiometric normalization		SAR image linear scaled to (0-255)	Natural logarithm of SAR image value, then histogram equalization to 0-255 of both images
Value range	theoretical	[0,1]	$(-\infty, +\infty)$
	practical	[0,0.25] of JOE	[-1,1.5]
Semantic meaning		Low value: change; high value: unchanged	Negative: demolished; (0,0.5): rebuilt, or partly changed; (0.5-1.5): unchanged
		Only relative interpretation	Physical meaning of slope
Analysis techniques (decision)		Expectation-Maximization (EM), or manual thresholding	Thresholding (0,0.5), or EM to distinguish unchanged and rebuilt building
Advantage		Suitable to multi-modal comparison	Physical meaning, easier analysis for making decision
Disadvantage		Missed-hit for monotonically decreasing relationship	Very sensitive to small changes, false-alarm for DSM error or neighboring influences of trees

Several combination methods have been tested. The following three combination methods have been tried, but they cannot compete with the subsequent method of "decision tree":

1. JHS×NMI, decision with EM-algorithm. The product of NMI and JHS provides a reasonable result (changed buildings have low values). However, the unsupervised EM-algorithm leads to false-alarms, since the product of two operators follows no longer a Gaussian distribution.
2. EM2d(JHS, NMI), decision with EM-algorithm of two dimensional version (EM2d). EM2d is an extension of the EM algorithm described in the Section 6.2.3, which aims at distinguishing the Gaussian mixture models in 2 dimensional (every object with two feature parameters). However, if the scene includes very few changed buildings, the sample of changed buildings cannot constitute a Gaussian distribution and the result will be false.
3. EM2d(JHS, JHS×NMI). Instead of using NMI as one feature parameter of the last method, the product of JHS×NMI is used here. In this case, the joint feature distribution highly dependents on the JHS. However, this method still fails because of the same reason in the last method.

The method "decision tree" has exploited the potential of both operators and yielded the best results. The decision-tree is illustrated in Fig. 6.9. This method exploits the physical meaning of JHS to provide a basic decision, and uses the NMI afterwards to improve the decision accuracy of JHSϵ(0,0.5).
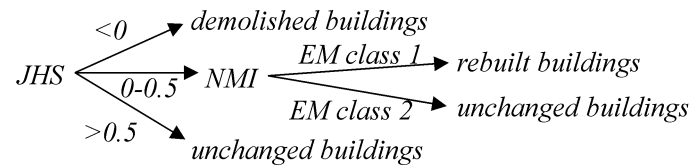
Fig. 6.9: The algorithm of decision tree to combine NMI and JHS for change detection between LiDAR and SAR data.

6.2.6 Data set description

To assess the potential of the proposed approaches, experiments were carried out on a LiDAR DSM (see in Fig. 6.10a) and a TerraSAR-X GEC image (see in Fig. 6.10b). The LiDAR data have been acquired in 2003-04 over Munich city center with a vertical and horizontal resolution of 0.1 meter and 1 meter, respectively. This DSM includes no vegetation. Most of the buildings in the test site have a height of about 30 meters, include a courtyard and are located close to each other. This situation makes the test site difficult to analyze, since the backscattering from different walls and buildings are mixed.

The SAR image (high resolution spotlight mode, 0.5 meter pixel spacing) has been acquired from a descending orbit with an incidence angle of 39.3° on 2010-01-05.

The pre-event LiDAR data was acquired seven years prior to the SAR image. Different changes might have occurred during this long time. For example, buildings might have been demolished or rebuilt; the roof material might have been changed; new buildings might have been built. All of these changes will affect the backscattering of buildings in the SAR image.

As reference data, the archived space-borne optical images in Google Earth (see Fig. 6.11) is used, which were acquired on 2004-08-29, 2007-08-25, and 2009-05-23. The first and the third date are close to the dates of the two data acquisitions, while the second is used to see what happened between the two acquisitions.

(a)   (b)
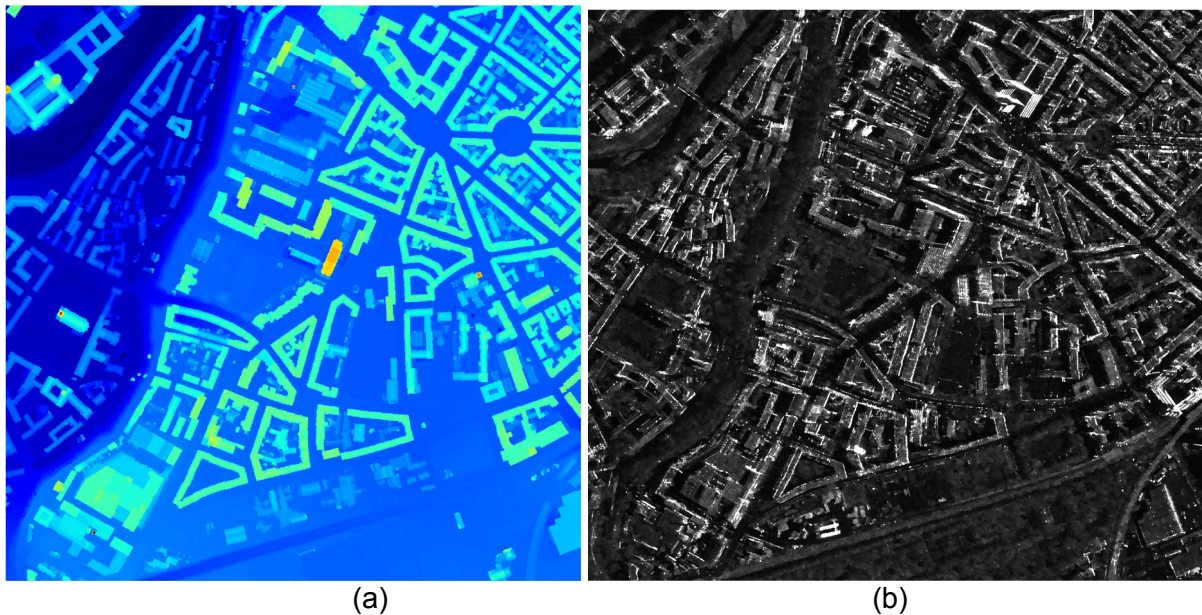
Fig. 6.10: The input data showing the same area in Munich center: (left) LiDAR digital surface model, acquired at 2003-04, (right) TerraSAR-X image after non-local filtering, acquired on 2010-01-05 with incidence angle of 39°.

(a)   (b)
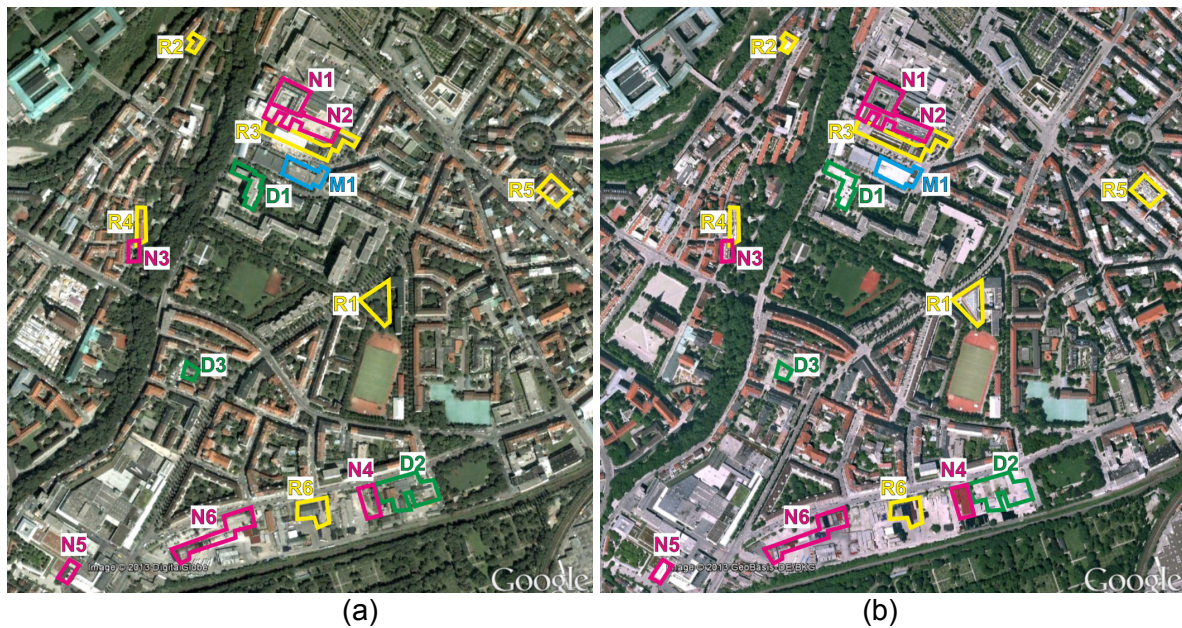
Fig. 6.11: Ground truth data of change detection derived by visual interpretation from Google Earth images. (left) 2004-08-29, (right) 2009-05-23. Manually extracted types of changes are marked with polygons of different colors (magenta: new; green: demolished; yellow: rebuilt; cyan: material change).

6.2.7 Experimental results of pixel-based positive change detection

The SAR images are generated using the LiDAR DSM with the method described in Chapter 4. Different layers (shadow, ground, layover, and double-bounce) are generated. As already mentioned, the shadow and ground layers together are called "dark layer", while the layover and double-bounce layers are referred to as "bright layer". The SAR image (with digital numbers denoting the signal amplitude) is processed by a non-local filter (Deledalle et al. 2009) to reduce the speckle noise.

The histograms of SAR pixel values in different layers are presented in Fig. 6.12. Note that the horizontal axis refers to the natural logarithm of the SAR image value. The estimated normal distributions are illustrated by dashed lines accordingly. These lines approximate the histograms for the proposed application sufficiently. Nevertheless, other distributions (e.g., generalized Gaussian distribution, Gamma distribution, generalized Gamma distribution [Li et al. 2011]) might fit the SAR distribution slightly better, but they will not significantly affect the threshold determination.

Table 6.5 presents the statistical parameters of the SAR image in different layers. The area ratio of dark layers in the image is about 60%. The mean values of different layers are similar, indicating the difficulty of distinguishing the pixels.
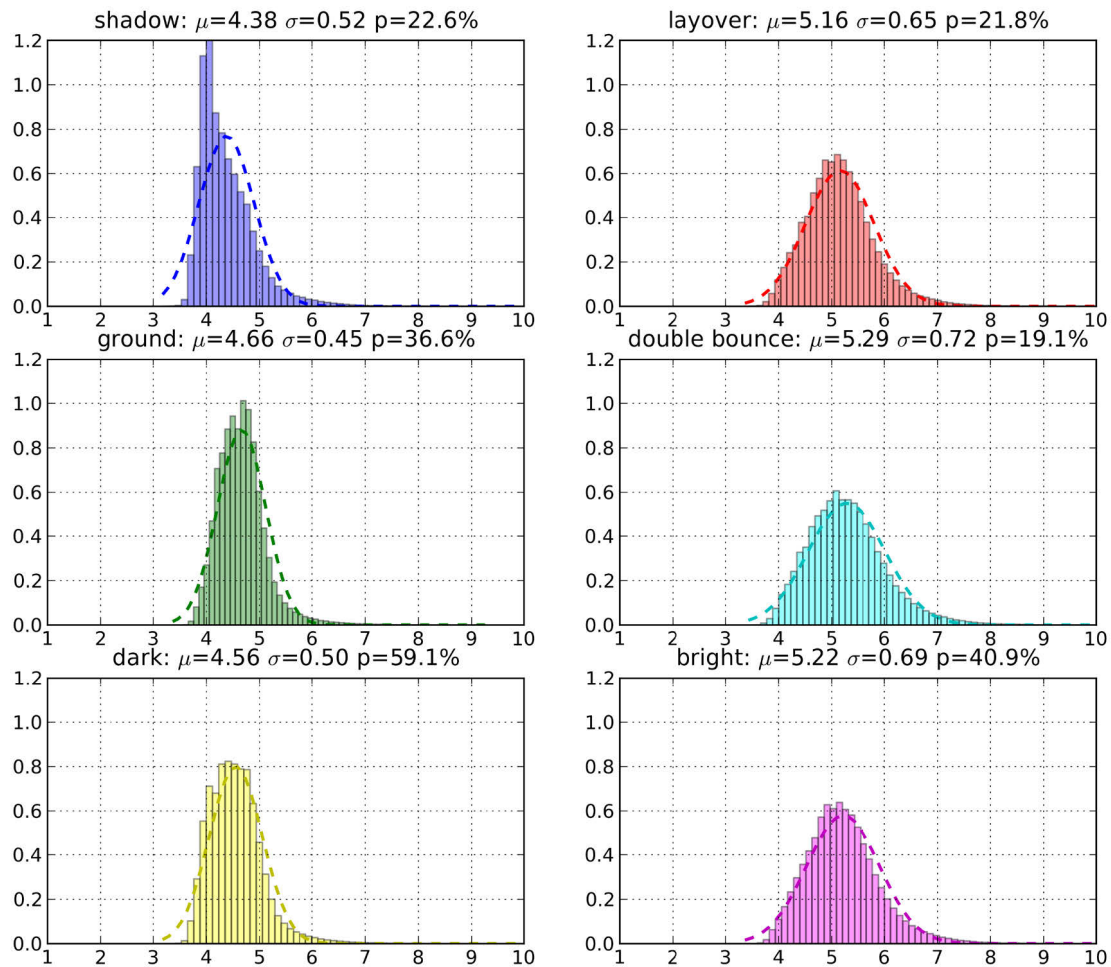
Fig. 6.12: The histograms of SAR pixel values in different layers with the estimated Gaussian distribution lines. The horizontal axis is the natural logarithm of the image value.

Table 6.5: Statistical parameters of the SAR image in different layers

layer	Area (pixels)	Area ratio	ln(SAR) μ	ln(SAR) σ	SAR μ	ln(SAR) μ-σ	ln(SAR) μ+σ	SAR μ-σ	SAR μ+σ	ln(SAR) μ-2σ	ln(SAR) μ+2σ	SAR μ-2σ	SAR μ+2σ
shadow	1302542	23%	4,38	0,52	78	3,86	4,90	46	133	3,34	5,42	27	224
ground	2110720	37%	4,66	0,45	104	4,21	5,12	66	165	3,76	5,57	41	261
layover	1255763	22%	5,16	0,65	173	4,51	5,81	89	332	3,86	6,46	46	638
double bounce	1102341	19%	5,29	0,72	196	4,56	6,01	94	407	3,84	6,74	45	841
dark	3413262	59%	4,56	0,50	94	4,06	5,05	56	155	3,56	5,55	34	256
bright	2358104	41%	5,22	0,69	183	4,53	5,91	91	367	3,84	6,60	45	732
all	5771366	100%	4,83	0,67	123	4,16	5,50	62	242	3,49	6,16	31	474

To find a suitable threshold value, different false-alarm-decision-costs are defined. Their derived threshold values with ratios of false-alarm and missed-hit are presented in Table 6.6. The difference between the threshold values of shadow-to-bright, ground-to-bright and dark-to-bright layers is minor. The dark layer contains more pixels than the shadow and ground

Table 6.6: Threshold values derived from different layers (with the bright layer) and different false-alarm-costs (Pf: false alarm rate; Pm: missed hit rate; P0: probability of dark signal; P1: probability of bright signal)

Layer	False alarm cost	Threshold (ln)	Threshold (ori.)	P0*Pf	P1*Pm	Pf	Pm
Shadow	1	4,60	98	0,119	0,119	0,335	0,185
	5	5,22	183	0,019	0,321	0,054	0,499
Ground	1	5,04	153	0,095	0,209	0,201	0,396
	5	5,57	262	0,010	0,367	0,021	0,695
Dark= shadow +ground	1	5,15	171	0,070	0,188	0,119	0,460
	2	5,40	220	0,027	0,247	0,046	0,604
	3	5,53	251	0,015	0,276	0,026	0,675
	4	5,62	274	0,010	0,294	0,017	0,719
	5	5,68	293	0,007	0,306	0,012	0,749
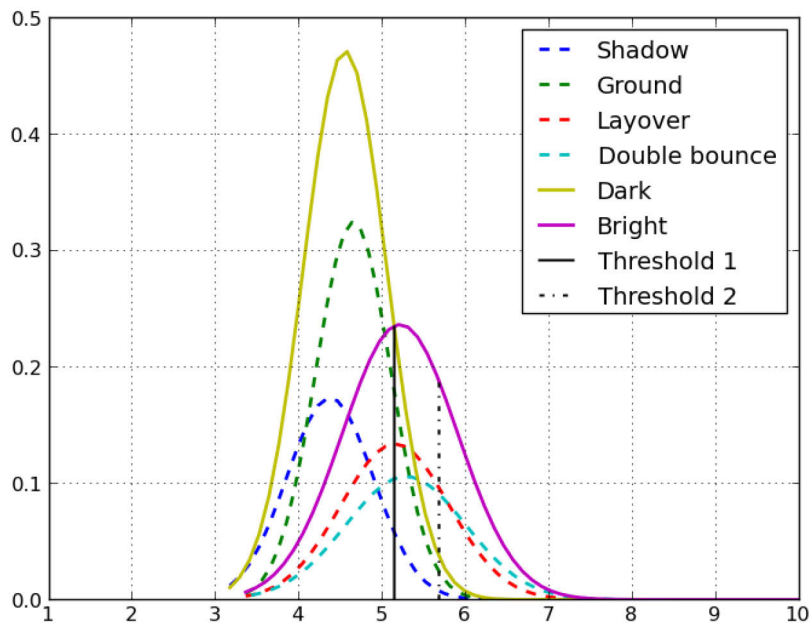
Fig. 6.13: The distribution estimates of SAR image values in different layers and the two threshold values (vertical lines) between the dark and bright layers with false-alarm costs of 1 and 5.

layers. Since large "training data" will provide a robust result (specific for scenes with very small shadow or ground layers), the threshold values derived from the dark-to-bright layers are chosen for the next stage of processing.

The threshold value derived from the false-alarm decision-cost $C_{db} = 1$ is smaller than that from $C_{db} = 5$, leading to a high false-alarm rate and low missed-hit rate. These two threshold values are illustrated in Fig. 6.13, with the mixture Gaussian distributions of dark and bright layers. The corresponding SAR images after thresholding are presented in Fig. 6.14. The detected changed pixels in the shadow and ground layers are illustrated by blue and green colors, respectively. In Fig. 6.14a, many detected pixels are located in the ground layer. Most of them correspond actually to trees (lower image, and left upper corner) and urban railway

lines (right lower corner). In both figures, many small masks are derived within the boundaries of the dark layers. They are mainly due to the LiDAR model errors (e.g., missed details of roofs, slightly sloping walls instead of vertical walls, location errors). In the left and right borders of both Figures, many small masks are derived. This is mainly due to the lack of LiDAR data. The buildings outside the LiDAR data area also affect the SAR image. But they cannot be considered in the simulated layers. So the results in the left and right borders of the change map should be discarded.

(a)   (b)
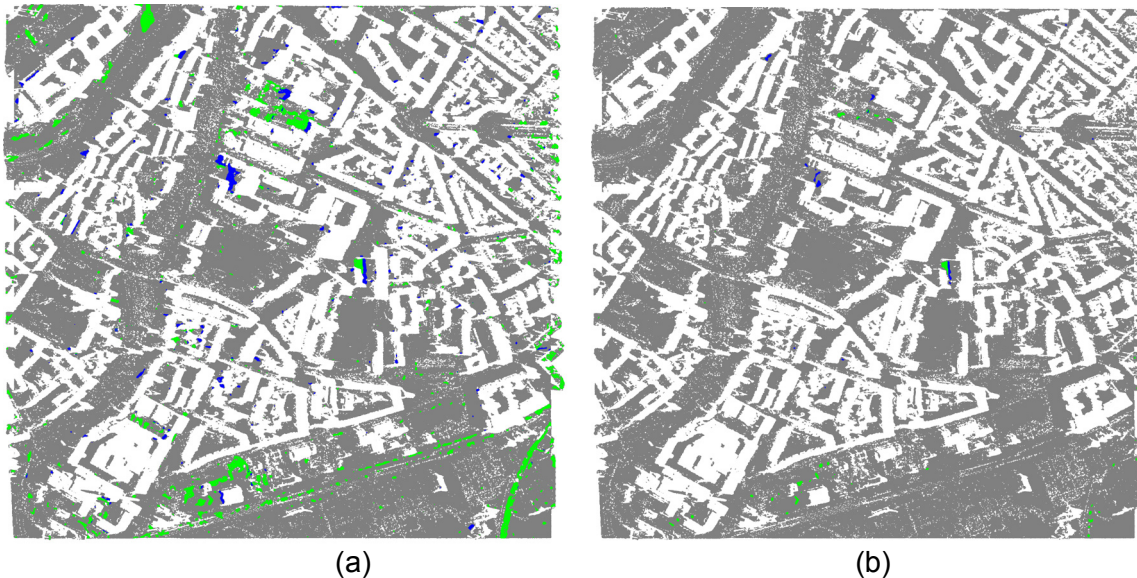
Fig. 6.14: Masks based on the dark layer of the SAR image after thresholding. (a) weak change Bw with false-alarm-cost 1, (b) strong change Bs with false-alarm cost 5 (blue: detected change in the shadow layer; green: detected change in the ground layer; grey: dark layer; white: bright layer and background).

(a)   (b)
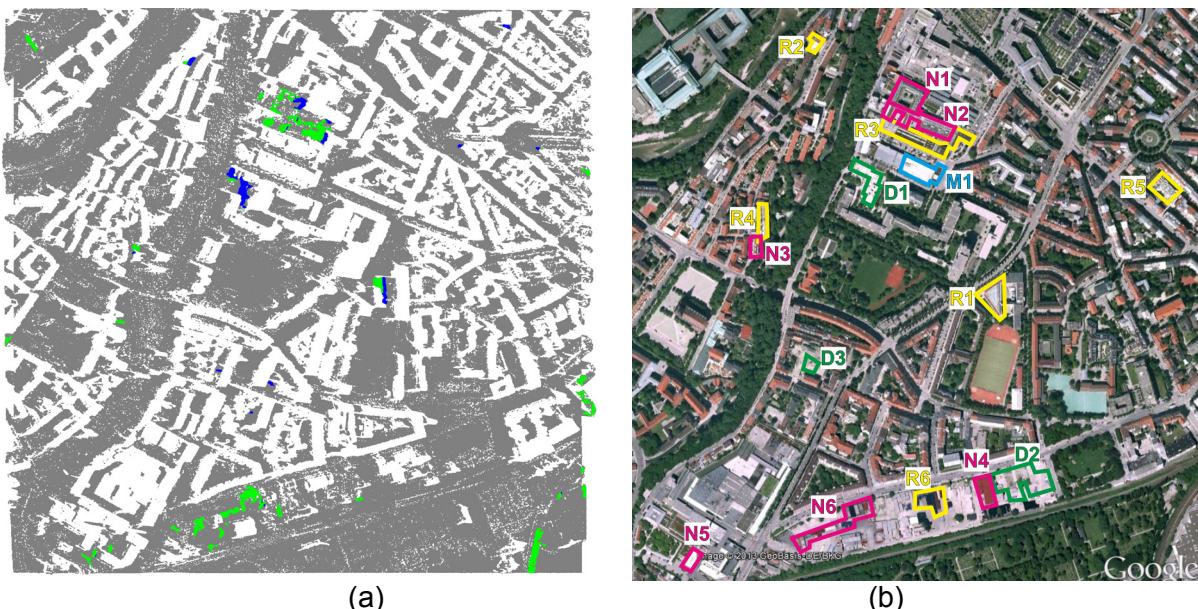
Fig. 6.15: Final result of pixel-based change detection between LiDAR and SAR data: (a) change map (blue: detected change in the shadow layer; green: detected change in the ground layer; grey: dark layer; white: bright layer and background), (b) ground truth, manually extracted change marked with polygons (magenta: new; green: demolished; yellow: rebuilt; cyan: change of roof material).

The change map after the binary propagation is presented in Fig. 6.15a. By eroding the dark layers, the detected pixels within the layers' boundaries are discarded. By using the high threshold value (see details in Section 6.2.2), the false-alarm pixels of most roads and trees are discarded. This figure mainly includes relatively big masks of changed pixels.

The ground truth image is presented in Fig. 6.15b. This is an optical image acquired from Google Earth, which was taken on 2009-05-23, close to the SAR acquisition date (2010-01-05). Several polygons with name and different colors mark the areas with different change-types. Most of the detected pixels fit to the ground truth (see Table 6.7). Not only the big new buildings N1 and N2, but also the small new buildings N3 and N5 are detected correctly. Actually the change of these two small buildings is even difficult to recognize by the human eye. The area N6 including many new containers is also detected correctly. The building N4 is the only missed-hit. This is probably due to its surface material, leading to weak backscattering in the SAR image. A big mask is detected near the demolished building D1. This is due to the construction machine located in the previous shadow area of D1 in 2004. The rebuilt areas R1 and R2 include small buildings in 2004 and new large buildings in 2009. The new parts of these large buildings are detected correctly.

The main false-alarm of the change map is located in the left upper corner and the right lower corner. The detected mask in the left upper corner actually refers to a bridge, which is not included in the LiDAR DSM. The right lower corner refers to a railway line with a train on it. The train and the railway line provide strong backscattering in the SAR image. They lead to the detection of a long railway line in the change map. This kind of false-alarm is difficult to avoid. However, it can be easily recognized by human interpretation, since no buildings will provide backscattering in such a long stripe form.

Table 6.7: Experimental results of pixel based positive change detection (see the buildings marked in Fig. 6.15).

Correctly detected new buildings	N1, N2, N3, N5, N6
Correctly detected rebuilt and demolished buildings	R1, R2, D1
Missed hit	N4
False alarm	Left upper corner (bridge), right lower corner (railway line with a train)

To conclude, this section presents a pixel-based algorithm for change detection between LiDAR and SAR data. The aim is to detect increased backscattering, which represents new buildings. The LiDAR data provides apriori information for distinguishing bright and dark signals in the SAR image. The bright signals in the simulated shadow and ground layers are detected as change. Two threshold values are derived to detect strong and weak changes. They are combined to provide a reasonable result. In the experimental results, most of the new buildings are detected. The false-alarm and missed-hit pixels are mainly due to the surface materials. This is also the main limitation of the proposed algorithm. The correctness of thresholding depends on the backscattering of different objects with different materials. As discussed in Fig. 6.3, some very specific new buildings hidden by adjacent buildings will not be detected by this method. Besides this, this technique cannot provide semantic meaning for the detected pixels. Some articles (Ferro et al. 2013) present methods for extracting buildings from a single SAR image, which might help the understanding of these detected pixels, although they work only for rectangular buildings. The proposed algorithm can be applied for other data sets, which may only differ in the false-alarm costs in the thresholding step. As an automatic algorithm, the proposed work provides a quick and rough change detection result, which might be useful for city expansion monitoring.

6.2.8 Experimental results of MI-based negative change detection

Altogether 81 isolated buildings, exhibiting a size larger than 1500 pixels, are extracted from the DSM. The building identifier numbers (ID) are overlaid on the nDSM and represented in Fig. 6.16. These buildings are of different types, sizes and heights. Most of them are building complexes with courtyards. The relationship of the building IDs with the manually extracted changes (see polygons Fig. 6.16b) is given in Table 6.8. The letters "S, M, and L" are used to denote the area ratio ("small, medium, and large") of the extracted polygons (indicating changes) within the corresponding buildings. For example, the extracted polygon D3 has a relatively small area in comparison to the corresponding Building 59, so Building 59 is marked as "59 (S)" in Table 6.8, indicating a small part of this building is changed. The area of the polygon D1 is equal to the area of Building 26, so Building 26 is marked with "26 (L)" in Table 6.8, meaning a large part of this building is changed. The asterisk "*" refers to "near", which means the building is located near the polygons. For example, the buildings 9 and 12 are located near the new building marked as N1, indicating that the backscattering of these two buildings might be affected by the change of N1. The new buildings and several of the rebuilt buildings have been already detected in the last section. In this section, only the demolished and rebuilt buildings are considered. Altogether 10 buildings have changed among the 81 buildings. If we discard the four buildings (marked with S) with low ratio of changed areas, only six buildings have changed: 26, 75, 19, 22, 76, and 33.
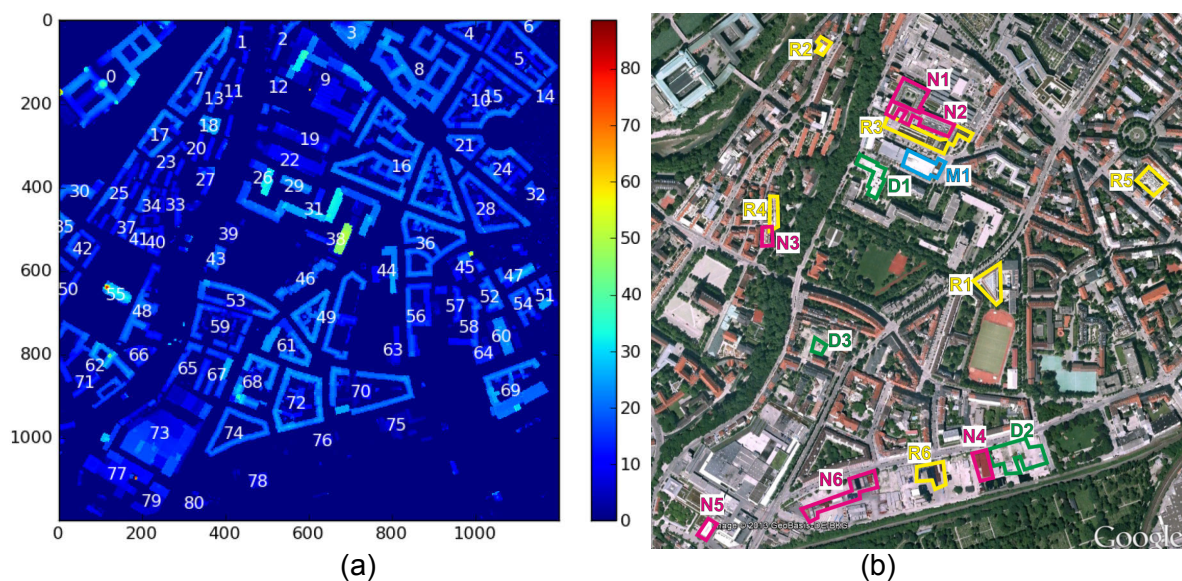
Fig. 6.16: Normalized digital surface model with building ID numbers (left) (color indicates the building height in meters). The right figure is the same as Fig. 6.15b.

Table 6.8: Relationship of the manually extracted polygons (indicating ground truth of changes during 2004 and 2009 in Fig. 6.16b) with building IDs (in Fig. 6.16a). The letters "S, M, L" after building IDs denote the area ratio of the polygons within the corresponding buildings, from small to large, respectively. The asterisk "*" denotes that the building is near the corresponding polygons.

New area	N1	N2	N3	N4	N5	N6	
Building ID	9*,12*	9*, 19*	33*, 40*	75*, 70*	77*, 79*	78*	
Rebuilt area	R1	R2	R3	R4	R5	R6	M1
Building ID	44 (S)	7 (S)	19 (L)	33 (L)	24 (S)	76 (L)	22 (M)
Demolished area	D1	D2	D3				
Building ID	26 (L)	75 (L)	59 (S)				
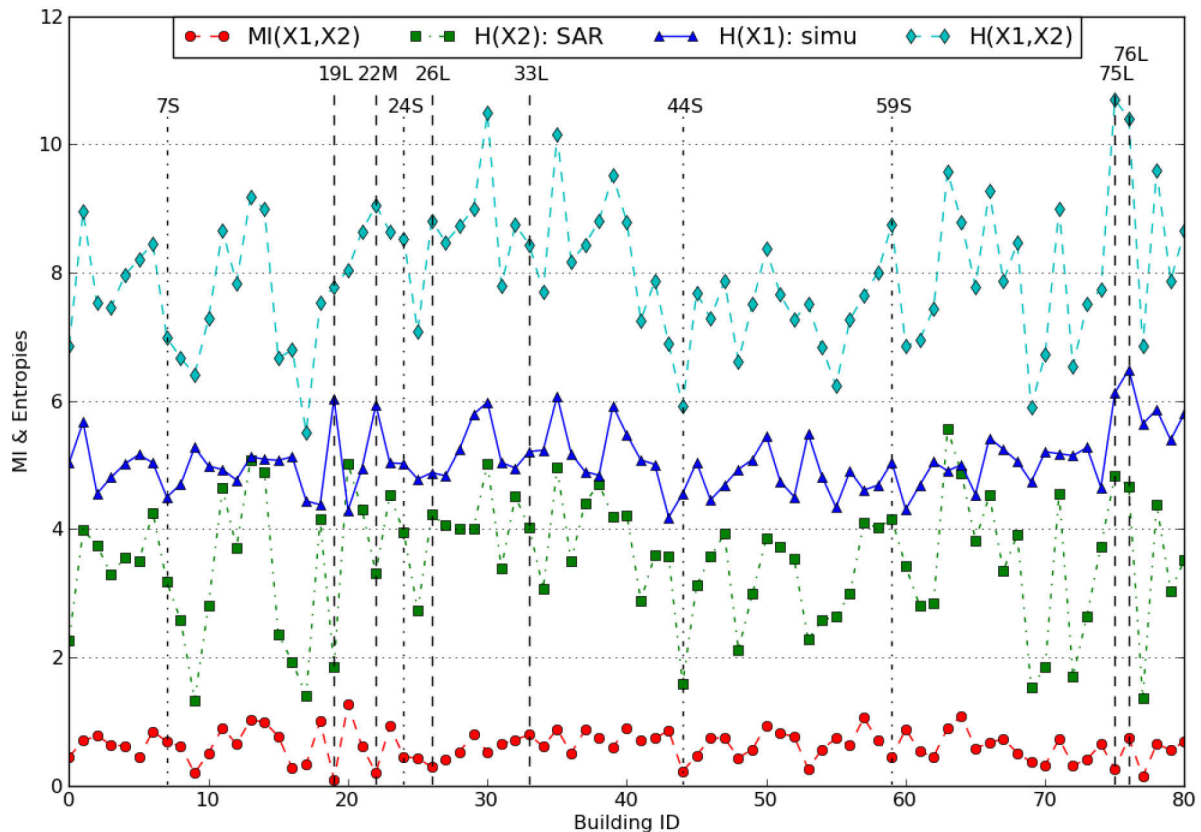
Fig. 6.17: Entropies and mutual information of the 81 buildings in the test scene (the connection of the dots are for better identifying the buildings, having no continuous meaning, the vertical lines mark the ten changed buildings related to Table 6.8).

For all extracted buildings, the building masks (including layover, shadow and double-bounce) are generated and the corresponding pixel values in the simulated image and filtered SAR image are extracted. Using these two sets of pixel values, the entropies of the simulated ($H(X_1)$) and real ($H(X_2)$) image patches, their joint entropy $H(X_1, X_2)$, and their mutual information $MI(X_1, X_2)$ are calculated. These values are plotted in Fig. 6.17. The simulated image patches have similar entropies, ranging from 4 to 6.5. In comparison, the entropies of the real SAR image patches vary strongly, ranging from 1 to 6. This is due to the differences of the size and reflection properties of buildings. The entropies of SAR images are mostly lower than that from the simulated images. Since the MI values are not good distributed, it is difficult to define a threshold value for change detection.

The different versions of NMI of the buildings are calculated and are plotted in Fig. 6.18. Because of the difference of the denominators in the different versions of NMIs ($H(X_1, X_2) \geq 1/2[H(X_1) + H(X_2)] \geq \sqrt{H(X_1)H(X_2)} \geq \min[H(X_1), H(X_2)]$), the relationship of the NMIs is: $STU - 1 \leq SAE \leq STR \leq JOE$, which is confirmed by this figure.
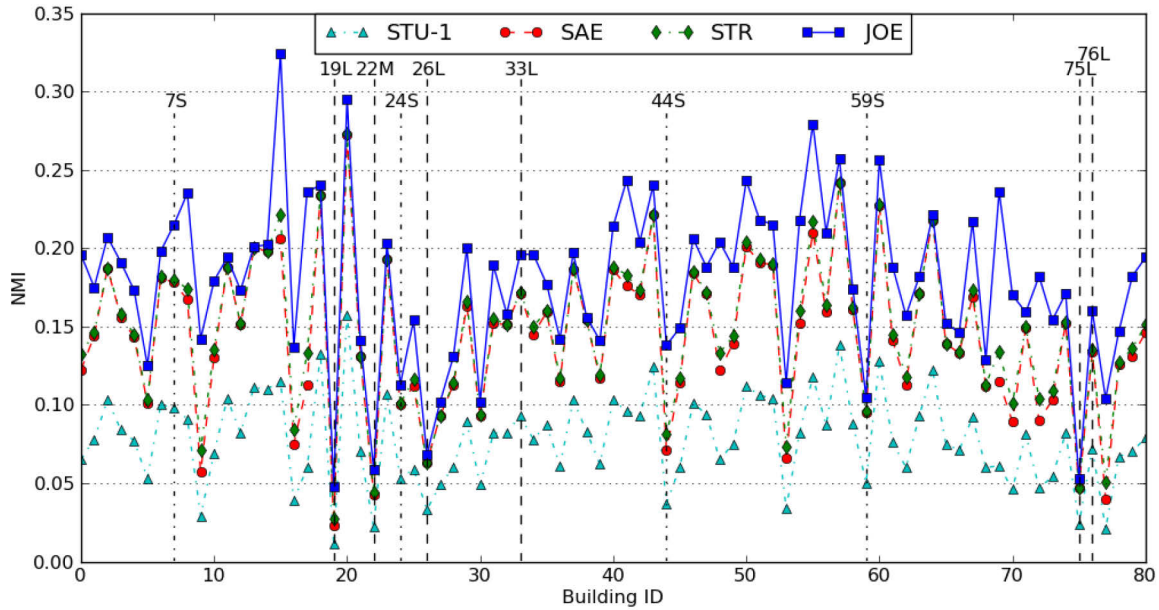
Fig. 6.18: The normalized mutual informations of the 81 buildings in the test scene (the vertical lines mark the ten changed buildings related to Table 6.8).

Table 6.9: The estimated parameters and results of the EM-algorithm for the different NMIs (the sign '#' denotes false-alarm detection)

NMI	μ_c	σ_c	$p(\omega_c)$	μ_u	σ_u	$p(\omega_u)$	T	Detected changed building ID
JOE	0.06	0.01	0.04	0.18	0.05	0.96	0.07	19, 22, 26, 75
STR	0.04	0.01	0.04	0.15	0.04	0.96	0.05	19, 22, 75, 77#
SAE	0.05	0.01	0.05	0.15	0.05	0.95	0.06	19, 22, 75, 9#, 77#
STU-1	0.02	0.01	0.04	0.08	0.03	0.96	0.03	19, 22, 75, 77#

STU uses the largest denominator for the normalization, so it is less sensitive to the building size. SAE and STR provide similar results. In comparison, JOE uses the smallest normalization $\min[H(X_1), H(X_2)]$ (in this case, $H(X_2)$ of SAR image patches is smaller than $H(X_1)$ for most of the buildings). Therefore, it is the most invariant operator to the differences of building SAR entropies.

The unsupervised EM algorithm is used for distinguishing the changed and unchanged buildings. The estimated parameters and the corresponding threshold values of different NMIs are listed in Table 6.9. Since the estimated standard deviations are very small, the difference between μ_c and μ_u can be considered as significant. Although very few changed buildings exist in the test scene, the EM-algorithm provides reasonable results. The rebuilt buildings 19 and 22 and the demolished building 75 are detected by all the four NMIs. The demolished building 26 is only detected by JOE. The false-alarm buildings 9 and 77 are detected by the other three NMIs. Both of these two buildings are located near the areas with new buildings (see Fig. 6.16 and Table 6.8 in this section). In comparison, JOE provides the best results.
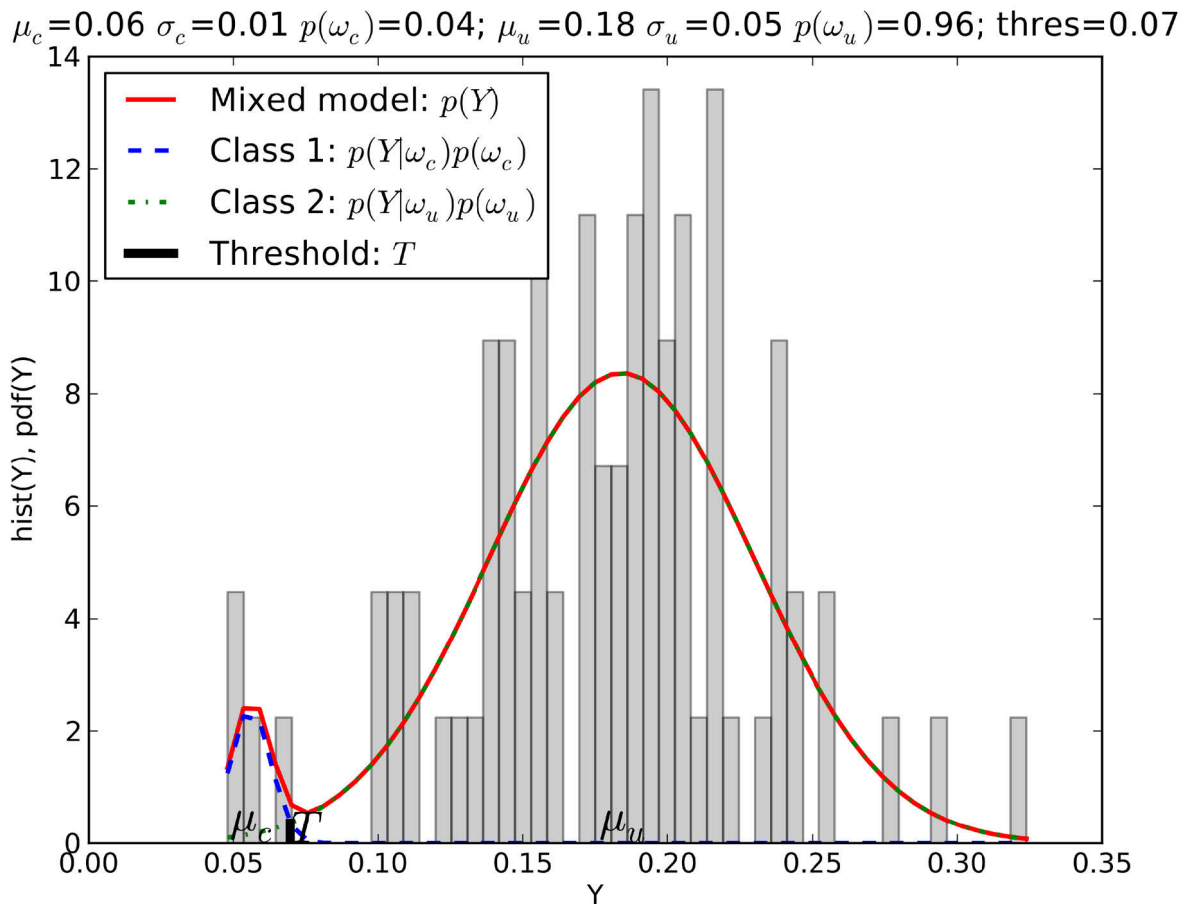
Fig. 6.19: The histogram of JOE with the estimated Gaussian mixture distributions (lines) and threshold values from the EM-algorithm (in this figure, Y=JOE).

The histogram of JOE and the estimated Gaussian mixture distribution are illustrated in Fig. 6.19. The estimated lines fit the histogram very well. Four changed buildings (demolished: 26, 75; rebuilt: 19, 22) are correctly detected. It is worth noting that the rebuilt building 19 is hard to recognize even by human eye, since its shape has only slightly changed. The shape of the building 22 has even not changed, whereas only its roof has been changed with another surface material, causing the radiometric appearance in the SAR image being different from the homogeneous simulated building surface. This building is also correctly detected by the developed method, highlighting the performance of NMI based change detection. As the whole building is considered and analyzed as a single object, the buildings (44, 7, 24 and 59) with only low ratio of changed areas are not detected. Building 33 was totally rebuilt but without any significant changes of size and roof material, so it is too difficult to be detected. Building 76 is actually rebuilt. Occasionally, the relationship of its values in the SAR and simulated images is just monotonically decreasing (i.e., SAR image has high values in the shadow layer and low values in the layover layer), which leads to a relatively high NMI value (0.16) (see Fig. 6.18). This is an example showing the limitation of NMI in change detection.
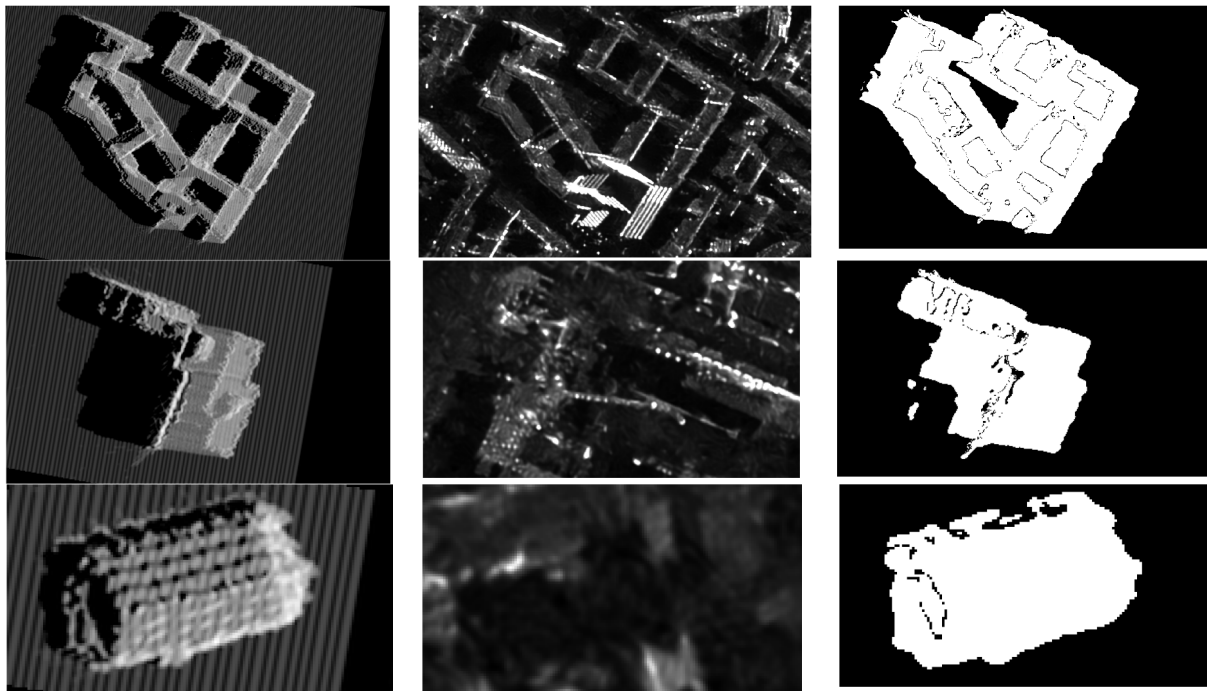
Fig. 6.20: Three buildings (top to bottom: 8, 26, 76, example for "detected unchanged" buildings, "detected changed" buildings, and "missed-hit" buildings, respectively) with their corresponding images (left to right: simulated image, non-local filtered SAR image, building mask).

Table 6.10: Confusion Matrix and kappa coefficient for the unsupervised change detection of NMI version JOE (the values in brackets have not considered the 4 buildings with tiny changes)

Overall accuracy	92.6% (97.5%)	Prediction		Producer's accuracy
Kappa coefficient	0.539 (0.787)	Change	No change	
True	Change	4	6 (2)	40.0% (66.7%)
	No change	0	71 (75)	100%
User's accuracy		100.0%	92.2% (97.4%)	

To analyze the reason of the results, Fig. 6.20 presents the simulated and real SAR images with the building masks of several buildings. The building 8, 26, 76 are examples for "detected unchanged", "detected changed", and "missed-hit" buildings, respectively.

The confusion matrix for the unsupervised change detection results of JOE is provided in Table 6.10. The estimated Cohen's Kappa statistic (or kappa coefficient) (Cohen 1960) (Kappa coefficient is a statistical measure of inter-rater agreement for qualitative items) is 0.539. The false-alarm error is zero. The overall accuracy is 92.6%. If we do not consider the four buildings with tiny changes (the values in brackets), the overall accuracy is 97.5%, indicating a very good performance of NMI-based change detection algorithm.

6.2.9 Experimental results of JHS-based negative change detection

The input of JHS is the same as for NMI: two sets of pixel values of the corresponding simulated and real SAR image patches according to the same building. Three example buildings with their simulated, real SAR images and joint histograms before and after radiometric normalization are presented in Fig. 6.21. The building 8 and 26 are examples for unchanged and changed buildings, respectively. The building 76 is the missed-hit building of NMI. Before radiometric normalization, the three buildings have similar values of JHS, as the SAR images have low backscattering which dominates the calculation of the joint histogram slope. After the radiometric normalization, the JHS values of the three buildings are significantly different. Especially the changed building 76 has a strong negative slope, confirming that it has been changed.
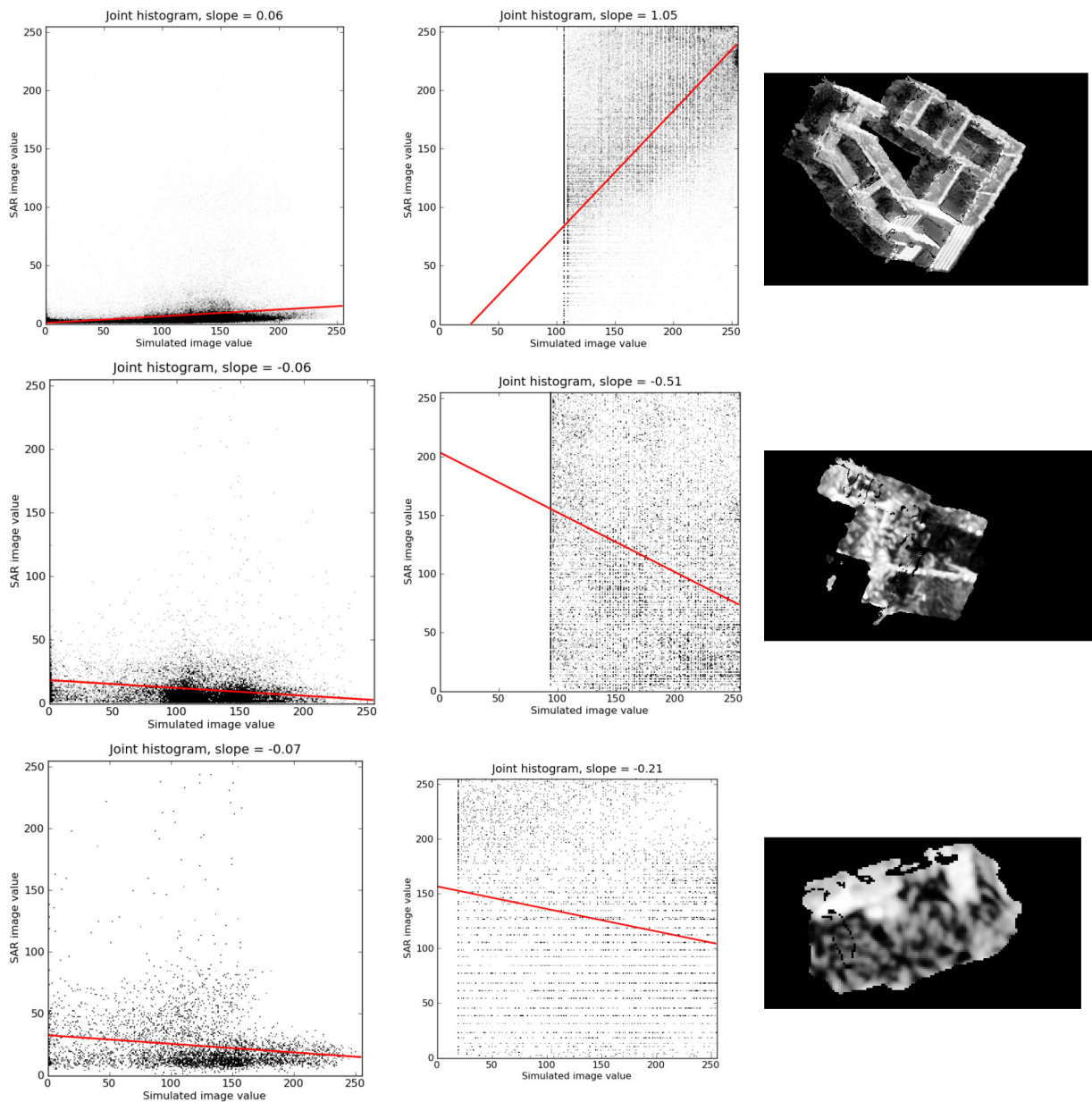
Fig. 6.21: Three buildings (top to bottom: 8, 26, 76) with their corresponding images (left to right: joint histogram and slope line without and with radiometric normalization, SAR image after radiometric normalization). This figure can be analyzed together with Fig. 6.20.
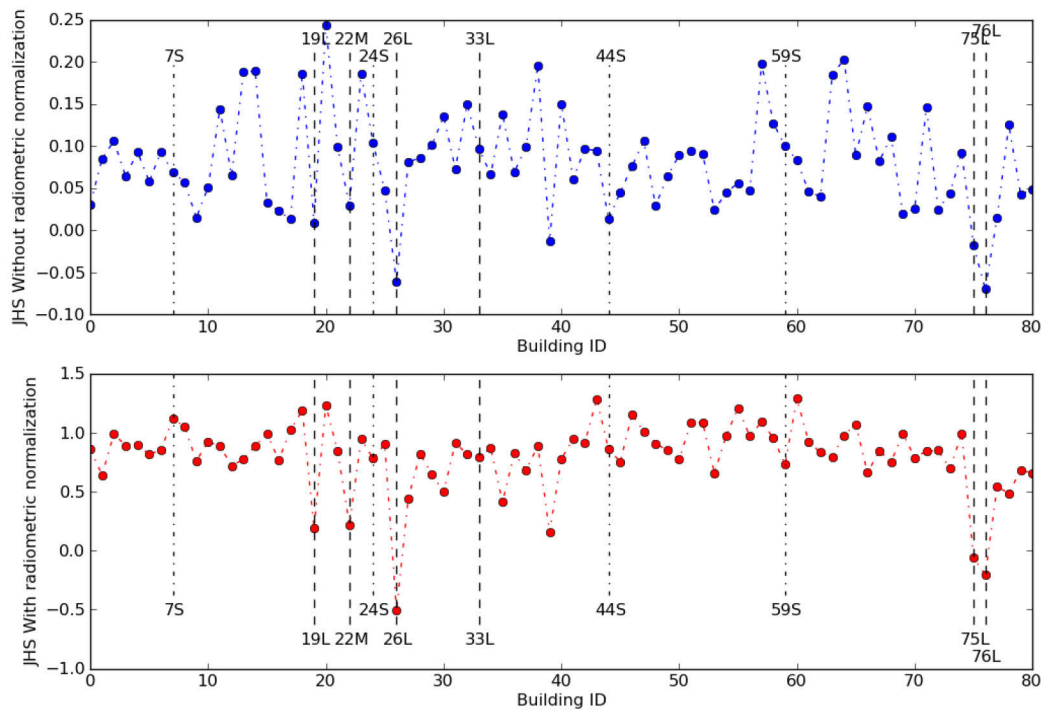
Fig. 6.22: JHS of the 81 buildings without (top) and with (bottom) radiometric normalization (the vertical lines mark the ten changed buildings related to Table 6.8).

Fig. 6.22 plots the JHS of all the 81 buildings without and with radiometric normalization. The JHS without radiometric normalization is not easily distinguishable. In comparison, the JHS after radiometric normalization ranges from -0.5 to 1.3. Most of the unchanged buildings have JHS ranging between [0.8, 1.2], which is close to the ideal unchanged value "1", indicating reasonable physical meaning of JHS.

The histogram of JHS of the buildings is illustrated in Fig. 6.23, with the curves of estimated probability density functions of the Gaussian mixture model from the EM-algorithm. The unchanged buildings with high JHS values constitute a good form of Gaussian distribution. In comparison, the changed class includes only a few values and appears to be not sufficient to constitute a Gaussian distribution. The estimated threshold value 0.47 is relatively high and leads to false alarms for buildings 27, 35 and 39.

The confusion matrix for the unsupervised change detection results of JHS is provided in Table 6.11. The JHS leads to 3 false alarms and 5 missed hits. The overall accuracy is 90.1%, and the kappa coefficient is 0.501. If we do not consider the four buildings with tiny changes (the values in brackets), these two values improve to 95.1% and 0.688, respectively.

Compared to the results of NMI, the overall accuracy of JHS is slightly lower. This is mainly due to the three additional false-alarm buildings. Apparently the JHS values of changed buildings are more distributed. Therefore they are difficult to constitute a clear Gaussian distribution, which lead to inaccuracy of finding the threshold value. Instead of using EM to analyze the results of JHS, the physical meaning of JHS can be exploited to make decisions: negative values indicate change; values bigger than 0.5 refer to non-change; values between (0, 0.5) mark change candidates, which need to be analyzed by human interpretation or by a combination with other methods.

μ_c=0.23 σ_c=0.40 $p(\omega_c)$=0.13; μ_u=0.88 σ_u=0.17 $p(\omega_u)$=0.87; thres=0.47
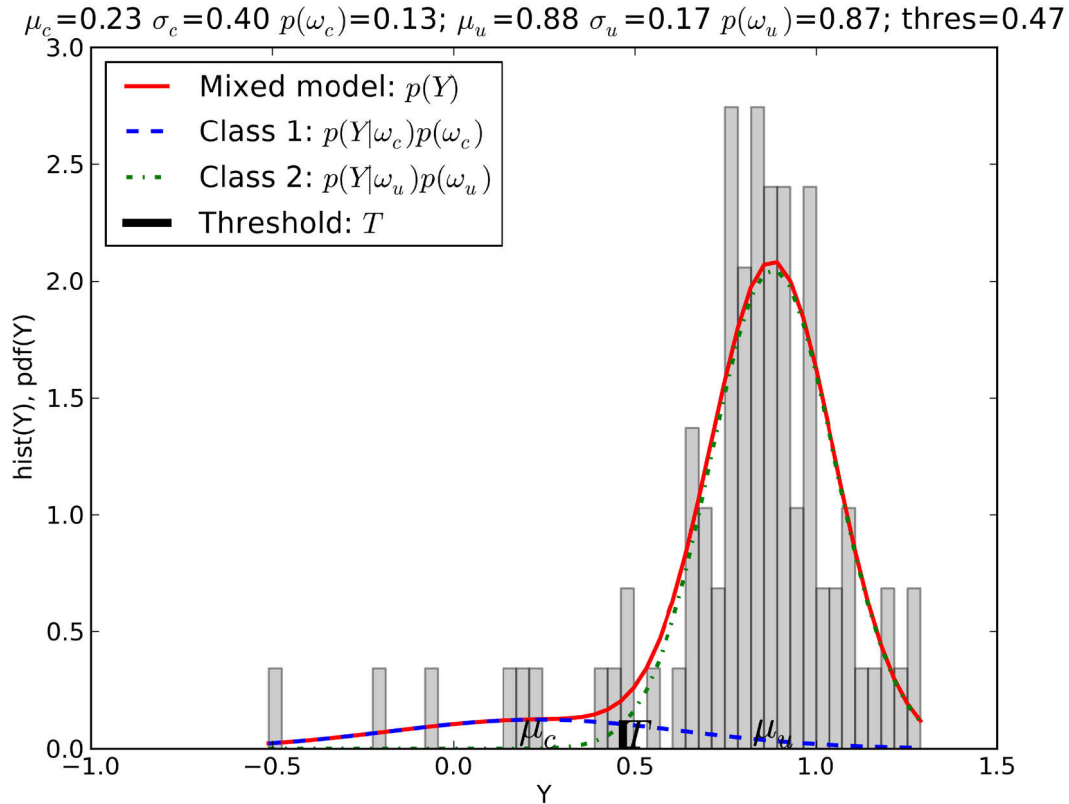
Fig. 6.23: Histogram of JHS (=Y) with the estimated lines representing the probability density functions of Gaussian mixture model and threshold values from the EM-algorithm.

Table 6.11: Confusion Matrix and kappa coefficient for the unsupervised change detection of JHS (the values in brackets have not considered the four buildings with tiny changes)

Overall accuracy	90.1% (95.1%)	Prediction		Producer's accuracy
Kappa coefficient	0.501 (0.688)	Change	No change	
True	Change	5	5 (1)	50.0% (83.3%)
	No change	3	68 (72)	96.0%
User's accuracy		62.5%	93.2% (98.6%)	

To conclude, the new comparison operator JHS described in this dissertation provides a high accuracy for change detection between LiDAR and SAR data. Compared to NMI, JHS leads to fewer missed hits but more false alarms. Because of the physical meaning of JHS, it is straightforward to interpret the results and provides an additional decision method besides the EM algorithm.

6.2.10   Experimental results of combination of NMI and JHS

In Fig. 6.24, the two comparison operators NMI and JHS with their product are visualized separately. The product NMI×JHS follows mainly the tendency of NMI and is not suitable as a final change detection operator.
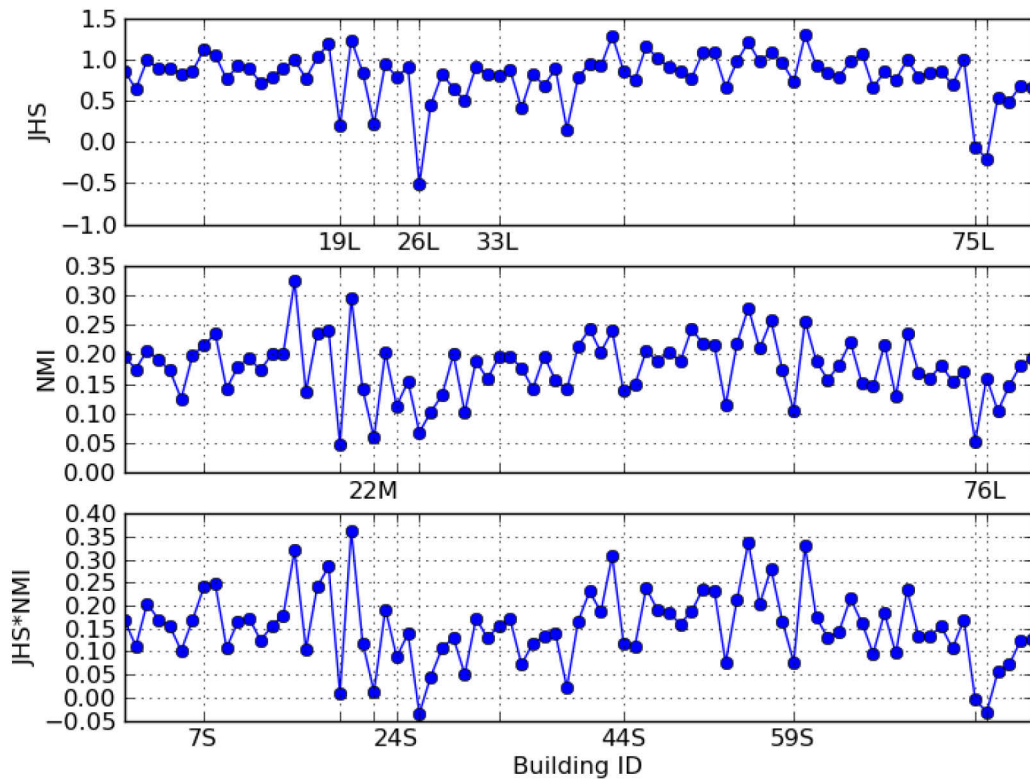
Fig. 6.24: Comparison operators NMI, JHS, and NMI×JHS of the 81 buildings (the vertical lines mark the ten changed buildings related to Table 6.8).
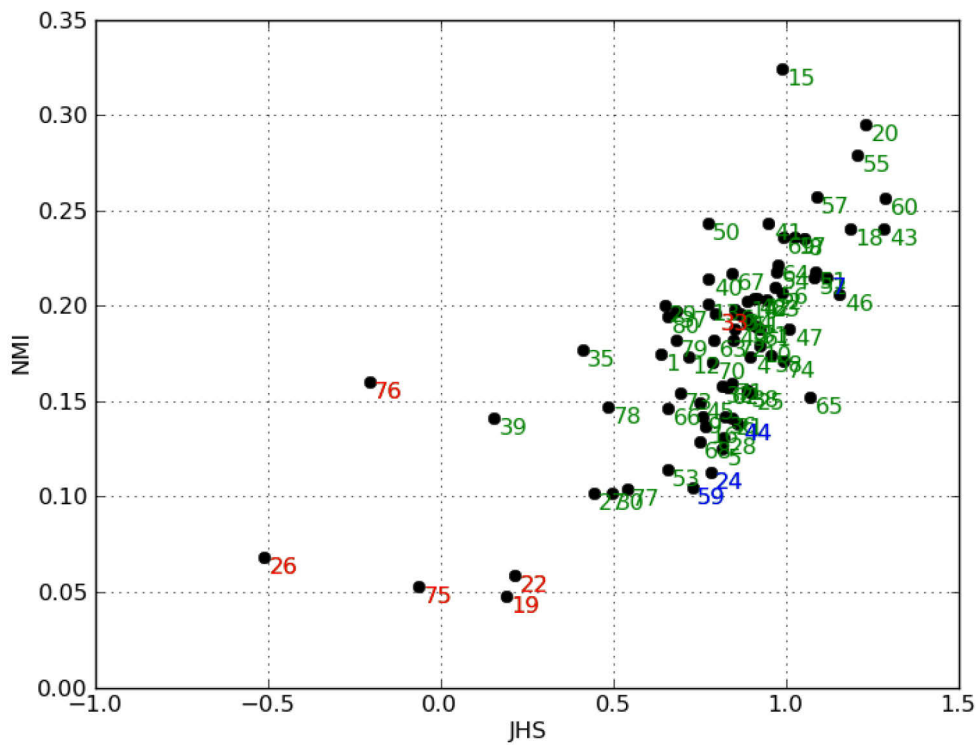
Fig. 6.25: Joint plot of the NMI and JHS values of the 81 buildings with their building IDs (the red and blue color represented IDs refer to the ten changed buildings with large and tiny changes, respectively, see ground truth in Table 6.8).

Table 6.12: Confusion Matrix and kappa coefficient for the unsupervised change detection by combining NMI and JHS (the values in brackets have not considered the four buildings with tiny changes)

Overall accuracy	93.8% (98.8%)	Prediction		Producer's accuracy
Kappa coefficient	0.637 (0.903)	Change	No change	
True	Change	5	5 (1)	50.0% (83.3%)
	No change	0	71 (75)	100%
User's accuracy		100.0%	93.4% (97.4%)	

Fig. 6.25 shows the two comparison operator values of the buildings. The unchanged buildings approximate to a 2D Gaussian distribution. In comparison, the changed buildings are too few and distributed separately, so they do not constitute another 2D Gaussian distribution. Because of this, an analysis technique using EM2d (see Section 6.2.5) is not possible.

In comparison, the proposed method "decision tree" provides better results. The five detected changed buildings of the "decision tree" are 19, 22, 26, 75 and 76, which improves the results of NMI slightly (detection of the change of building 76). The combination of JHS and NMI leads to no false-alarm decision and five missed-hit decisions. If we do not consider the four buildings with tiny changes (the values in brackets), only one decision (Building 33) is wrong among the 81 buildings, leading to an overall accuracy of 98.3%. The building 33 is rebuilt but without significantly changed shape and material, so it is too difficult to detect.

As a conclusion, the combination of JHS and NMI using decision trees yields a better result than the individual comparison operators. This combined version is stable for most unchanged buildings, leading to a low missed-hit and false-alarm rate. Most of the buildings with a large ratio of changed areas are correctly detected, including demolished and rebuilt buildings. Especially, the building with changed roof material is also correctly detected. As mentioned before, the object-based change detection has one main limitation: if only a small part of the building has changed or been rebuilt, the comparison operator will not provide a significant change signal, as the main part of the building will still confirm the dominant backscattering in the SAR image. This limitation might be covered by wall-level change detection, which will be described in Sections 6.4 and 6.5.

6.3 Building change detection of two SAR images based on layer fill

The previous section presents object-based methods using LiDAR and SAR data to detect rebuilt and demolished buildings in urban scenarios. The advantage of these methods is that they require only pre-event LiDAR data. Since these methods compare the simulated image and real SAR image, they are limited due to two reasons. First, the LiDAR data is only a rough geometrical model of the real world. Many geometrical details (e.g., window structure, balcony, surface roughness, and roof pipelines), which play an important role in SAR backscattering, are not provided in LiDAR data. Second, the simulation uses unified radiometric reflection parameters for all surfaces, whereas in the real world the signal reflection depends on the surface material, which is not provided in the LiDAR data. These limitations might lead to false alarms.

Related works reported in the literature mostly compare two SAR images with the same imaging geometry for change detection. In comparison to LiDAR-SAR change detection, the SAR-SAR change detection is free from modeling of real world and assumption of reflection parameters, thus they avoid these modeling errors which may affect change detection results. However, the traditional SAR-SAR change detection also has limitations. On one side, the interpretation of the detected changes is difficult, especially for very high resolution data. They may only provide pixels with decreased or increased signals. But the interpretation of these detected changed pixels is still a challenging task. Recently, some articles (Ferro et al. 2013; Marin et al. 2015) have presented methods to solve this problem, but the provided methods can work only for specific buildings (e.g., isolated rectangular buildings). The second limitation is the requirement of SAR images with the same imaging geometry. This requirement might not be fulfilled if we want to use the first available SAR data in crisis situation. For example, the TerraSAR-X satellite has a period of 11 days (which can fulfil the same imaging geometry) and a global access time of maximum three days (which cannot guarantee the same imaging geometry).

According to the limitations of LiDAR-SAR change detection and traditional SAR-SAR change detection with the same imaging geometry, a novel change-detection technique is proposed in this section, using one LiDAR data set and two SAR images with different incidence angles as input (this method works also for SAR images with same incidence angles but with limited advantages). The method uses LiDAR data and simulation techniques to predict the building masks in SAR images and compares the corresponding pixel values of the two SAR images. Because of the simulation step this method has no problem with the interpretation of the results, and is not limited to SAR images with the same incidence angles.

It is worth noting that this method can only detect demolished buildings. New buildings cannot be detected as only existing buildings in pre-event LiDAR data are considered. Nevertheless, the detection of new buildings is not the intended goal of this method in crisis situations.

6.3.1 Methodology

If a building is demolished, the backscattering of its layover area will decrease while the backscattering of its shadow area will increase, as only the backscattering of the ground (street or square) will be on the former site of the building. To this end, the only problem is to distinguish the backscattering of the building layover and shadow from that of the ground.

This is in fact a challenging task in the research field of SAR image processing. Most of the work in the literature exploits the geometric or radiometric features of the building in the SAR image, like corner lines (Brett and Guida 2013), the L-shape geometry of building backscattering (Simonetto et al. 2005), or the layovers and shadows of building as wide lines (Ferro et al. 2013). These methods use only one SAR image, and normally only work for specific buildings, for example, isolated regular rectangular buildings. For building complexes in dense urban scenarios, they may lead to false alarms, since the geometric features might be mixed together and hard to extract.

Instead of using the image features directly, in this dissertation the simulated layers are used to analyze the corresponding SAR image pixel values in order to distinguish the backscattering of building layover and shadow from that of the ground.
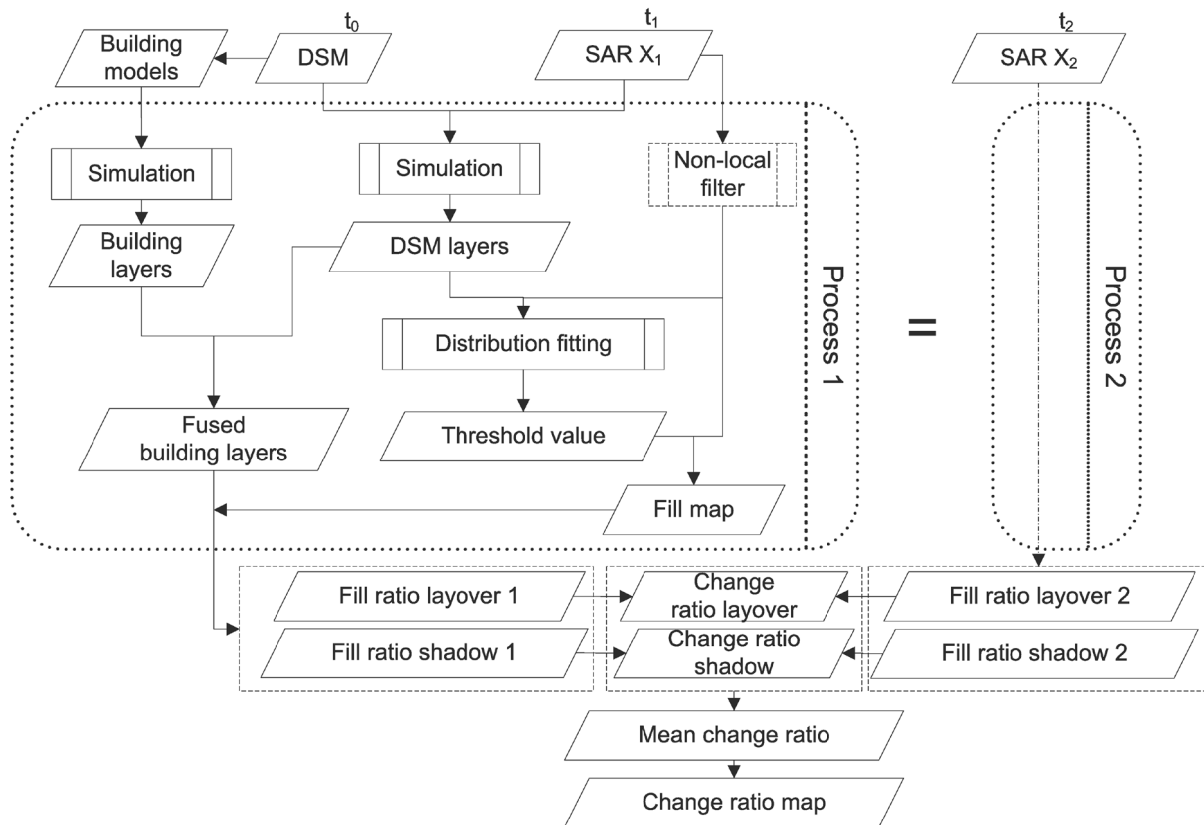
Fig. 6.26: Flowchart of change detection of two SAR images based on layer fill.

Fig. 6.26 illustrates the flowchart of the algorithm. Let us consider two amplitude high resolution SAR images (X_1 and X_2) acquired with different incidence angles on the same geographical area at different times (t_1 and t_2), capturing the pre- and post-event, respectively. The LiDAR data was acquired at time t_0 which was closed to t_1. Let us assume that no building was demolished between t_0 and t_1, and only a minority of the buildings was demolished between the times t_1 and t_2. The goal is to detect these demolished buildings. The detailed steps of the algorithm are:

1. Exploiting the geoinformation of the DSM (digital surface model) and the simulation technique described in Section 4.1, different layers (layover, double-bounce, shadow and ground) of the DSM are generated.
2. Using these layers, the corresponding SAR image parts are analyzed separately and two threshold values are calculated.
3. These threshold values transform the (filtered) SAR image to two binary images, which are called "fill map".
4. By combining the fused building layers and the SAR fill map, the fill ratios of the building layover and shadow masks are calculated.
5. Steps 1-4 are performed also for the SAR image X_2.
6. The fill ratios according to the two SAR images are compared and lead to a change ratio.
7. The change ratio values of every building are calculated and analyzed to detect demolished buildings.

A detailed description of the algorithm is presented in the following.

Thresholding

Let X_{1l}, X_{1s} and X_{1g} be the logarithmic amplitude values associated with the pixels belonging to the layover, shadow and ground layer in image X_1. The pixels belonging to the double-bounce layer are also included in X_{1l} as they have normally also higher values than those in the ground layer, which have the same properties as the pixels in the layover layer. As the intensity distribution of high-resolution SAR images in urban areas can be well modeled by the log-normal distribution (Oliver and Quegan 2004), the distribution of X_{1s} and X_{1g} are approximated by Gaussian functions:

$$f(x \mid X_M) = \frac{1}{\sigma_M \sqrt{2\pi}} \exp\left\{-\frac{(x - \mu_M)^2}{2\sigma_M^{\,2}}\right\} \sim N\left(\mu_M, \sigma_M^{\,2}\right). \ M \in \{1l, \ 1s\} \tag{6.19}$$

Where $\mu_M, \sigma_M^{\,2}$ indicate the mean and variance of the two distributions. Based on the Bayesian decision rule, a threshold value T_{1lg} is calculated by following Equation 6.13. This threshold value is used to distinguish the ground and layover signals. Using the same method, the threshold value T_{1sg} is calculated for distinguishing the shadow and ground signals.

The optimal precondition of this method for calculating the threshold is that no building has changed between t_0 and t_1. This is normally not the case. However, if only a minority of the buildings has changed, the threshold value should be acceptable for subsequent steps.

Calculation of fill ratios

Using the two values T_{1lg} and T_{1sg} to convert the SAR image, two binary images F_{1gl} and F_{1sg} are derived, which are defined as "fill maps". The value "one" in F_{1gl} means that the pixel has an intensity value greater than T_{1lg}, whereas the value "one" in F_{1sg} means that the pixel value is lower than T_{1sg}.

For any building in the DSM, its layover and shadow layer are generated using the method described in Section 4.2 and fused with the global layers using the method described in Section 4.3. The area of its fused layover layer is defined as A_l. The area of the corresponding mask in the fill map F_{1gl} with value one is A_{lf}. Then the fill ratio of the layover layer of this building is defined as

$$r_{1l} = \frac{A_{1lf}}{A_{1l}} \tag{6.20}$$

This value indicates the ratio of the simulated building layover area covered by building backscattering in the SAR image. Fig. 6.27 presents an example building with the fused building layers and the fill map of its layover layer.

Using the same idea, the fill ratio of the shadow layer of this building is defined as

$$r_{1s} = \frac{A_{1sf}}{A_{1s}} \tag{6.21}$$

(a) SAR image   (b) simulated image

(c) fused layers   (d) fill map of building layover layer
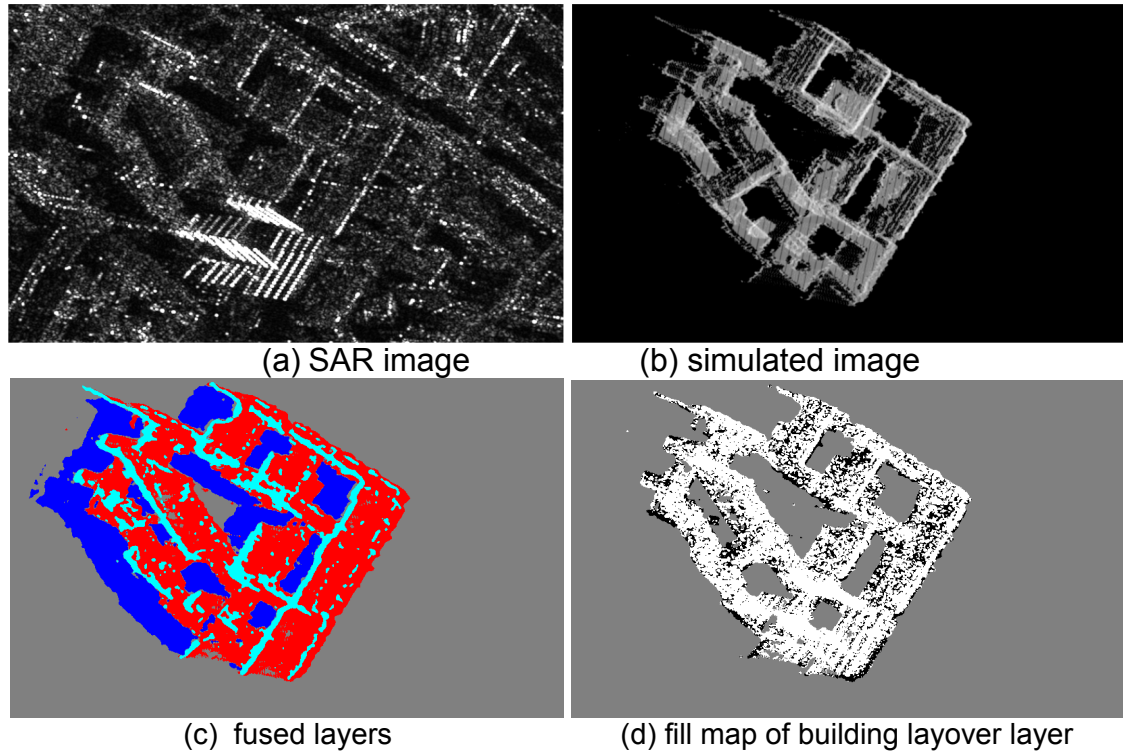
Fig. 6.27: Building layer fill. (a) TerraSAR-X image subset of a building in Munich, (b) simulated image, (c) fused layers of the building (blue: shadow, red: layover, cyan: double bounce, grey: background), (d) fill map of the building layover area (white: pixel with values above threshold, black: pixel with values below threshold, grey: background)

Where A_{1sf} is the area of the filled region of the fused building shadow layer, A_{1s} is the area of the fused building shadow layer.

The fill ratios r_{2l} and r_{2s} of this building are calculated for the SAR image X_2 in the same way.

Calculation of change ratio

The change ratio of one building layover layer is defined as

$$P_l = \max \left\{ 1 - \frac{r_{2l}}{r_{1l}}, 0 \right\}$$
(6.22)

As the aim of this change detection method is restricted to detect the demolished buildings, positive changes ($r_{2l} > r_{1l}$) are discarded. To avoid the following fusion steps being misled, the negative value of P_l is modified to 0. The greater the value P_l is, the higher is the possibility of a destroyed building. From another point of view, this value also indicates the level of destruction.

The change ratio of the building shadow layer is derived in a same way:

$$P_s = \max \left\{ 1 - \frac{r_{2s}}{r_{1s}}, 0 \right\}$$
(6.23)

Afterwards, the two change ratio values are fused with considering the area of layers as weights:

$$P_f = \frac{P_l A_{1l} + P_s A_{1s}}{A_{1l} + A_{1s}}$$

(6.24)

where P_f is the mean change ratio of the building.

This value is calculated for all the buildings or building complexes extracted from the DSM. Finally, a change ratio map is generated, including the building change ratio as the pixel value. This map can be provided for rescue team, so that they can choose the prior rescue targets.

6.3.2 Experimental results

Data set description

To assess the potential of the proposed approach, the same test scene as in Section 6.2.6 is used. Besides the data set (one LiDAR DSM acquired at time t_0 2003-04, one SAR image X_2 acquired at time t_2 2010-01-05, with incidence angle 39.3°) described there (see Fig. 6.10), another TerraSAR-X image (see Fig. 6.29a) with different incidence angle is available. This SAR image X_1 (high resolution spotlight mode, 0.5 meter pixel spacing) has been acquired from a descending orbit with an incidence angle of 25.3° on 2008-05-26 (time t_1).

The pre-event LiDAR data was acquired five years prior to the SAR image X_1. Any region with pre-event change, which happened between the time t_0 and t_1, is excluded from the following analysis.

Using the same optical images from Google Earth described in 6.2.6, the ground truth data is manually extracted and visualized in Fig. 6.28. The changes in between t_1 and t_2 are marked with solid polygons, while the changes in between t_0 and t_1 are marked with dashed polygons. In comparison to the optical ground truth in Fig. 6.16 and Fig. 6.28, only the changes marked with dashed polygons (N1, N3, R3, and R4) occurred before 2008 (time t_1). Considering the relationship of the polygons and building IDs in Table 6.13 and the ground truth optical images, the true demolished buildings are 26 and 75, while the true rebuilt buildings are 76 and 22, besides the four buildings (44, 7, 24, and 59) with tiny changes.

Besides the optical image as reference data, another TerraSAR-X image X_3 (see Fig. 6.29b),

Table 6.13: Relationship of the manually extracted polygons (indicating ground truth of changes during t_0-t_1 and t_1-t_2 in Fig. 6.28) with building IDs (in Fig. 6.16a). The letters "S, M, L" after building IDs denote the area ratio of the polygons within the corresponding buildings, from small to large, respectively. The asterisk "*" denotes that the building is near the corresponding polygons.

Change time	2007-2009 (t_1-t_2)					2004-2007 (t_0-t_1)	
New area	N2	N4	N5	N6		N1	N3
Building ID	9*, 19*	75*, 70*	77*, 79*	78*		9*,12*	33*, 40*
Rebuilt area	R6	M1	R1	R2	R5	R3	R4
Building ID	76 (L)	22 (M)	44 (S)	7 (S)	24 (S)	19 (L)	33 (L)
Demolished area	D1	D2	D3				
Building ID	26 (L)	75 (L)	59 (S)				

having the same incidence angle as X_1 and a similar acquisition time (2010-01-10) as X_2, is also used as a reference. At this end, a multi-temporal false color composite image (see Fig. 6.39b) of the two SAR images (X_1 and X_3) with the same incidence angle has been generated. In this image, the magenta color indicates the increased backscattering, while the green color stands for the decreased backscattering.

(a)   (b)
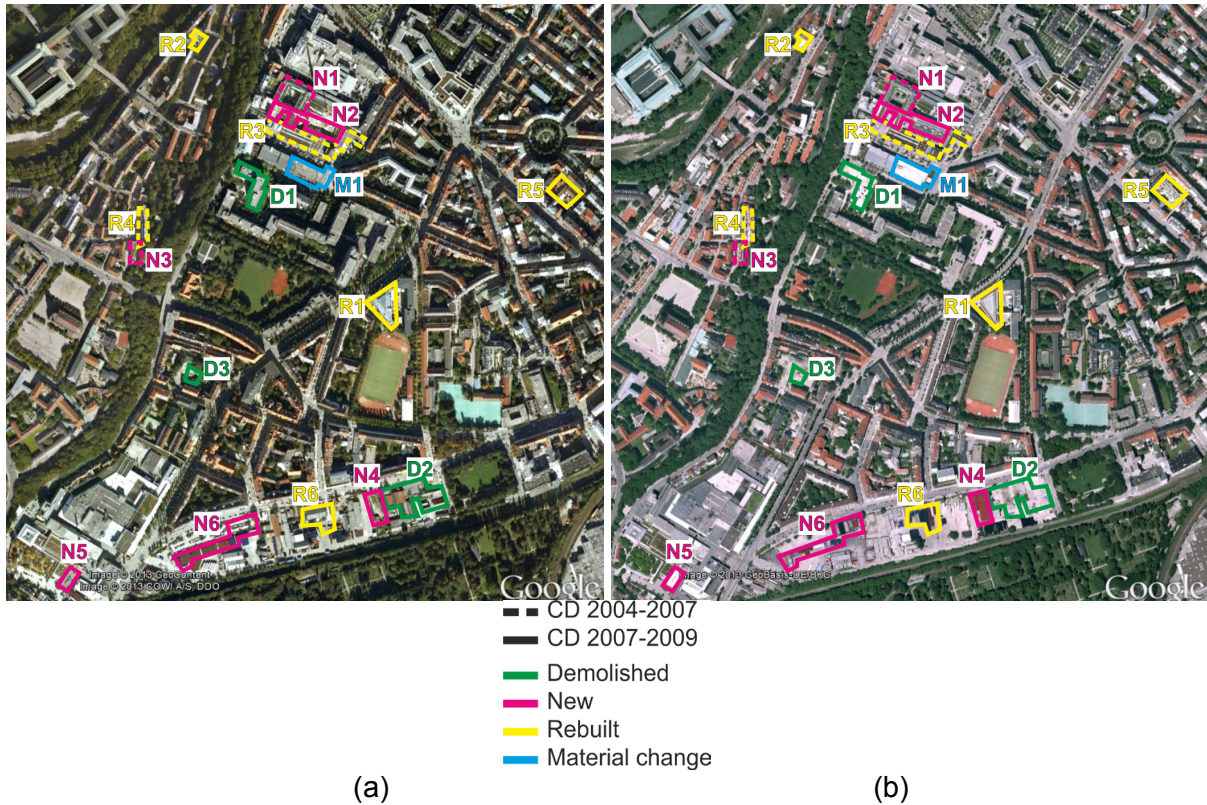
Fig. 6.28: Ground truth data of change detection (CD) derived by manual interpretation with Google Earth images. (left) 2007-08-25, (right) 2009-05-23. Manually extracted different types of changes are marked with dashed (t0-t1) and solid (t1-t2) polygons with different colors (magenta: new; green: demolished; yellow: rebuilt; cyan: material change).

(a)   (b)
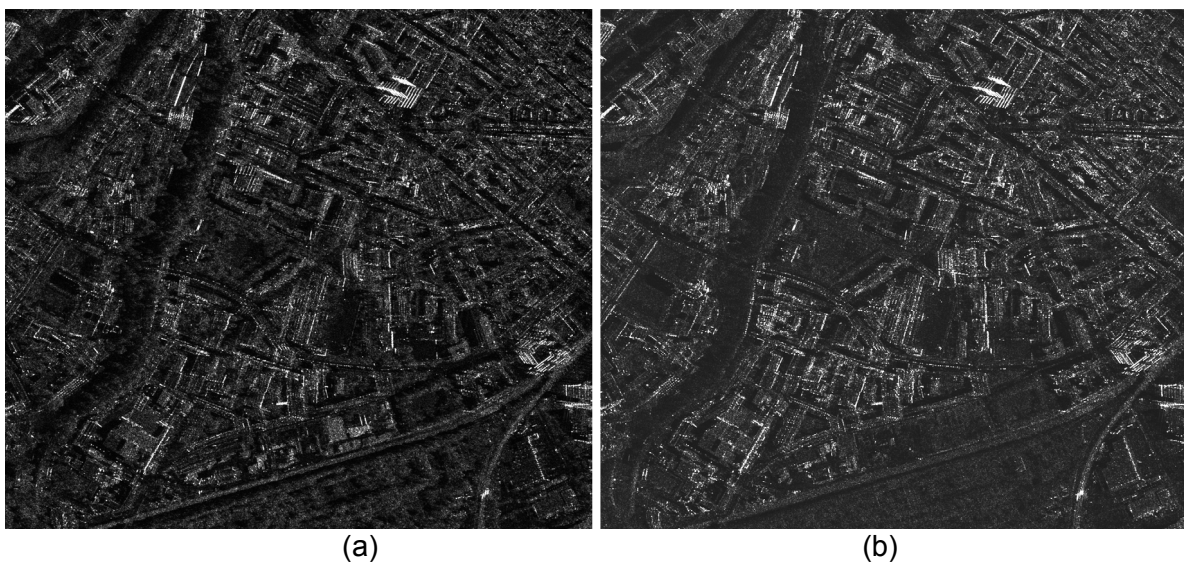
Fig. 6.29: TerraSAR-X amplitude images of Munich test site, located in UTM coordinate system, range direction: right to left. (a) Image X1 acquired on 2008-05-26 with incidence angle of 25°, (b) reference image X3 acquired on 2010-01-10 with incidence angle of 25°.

(a)   (b)
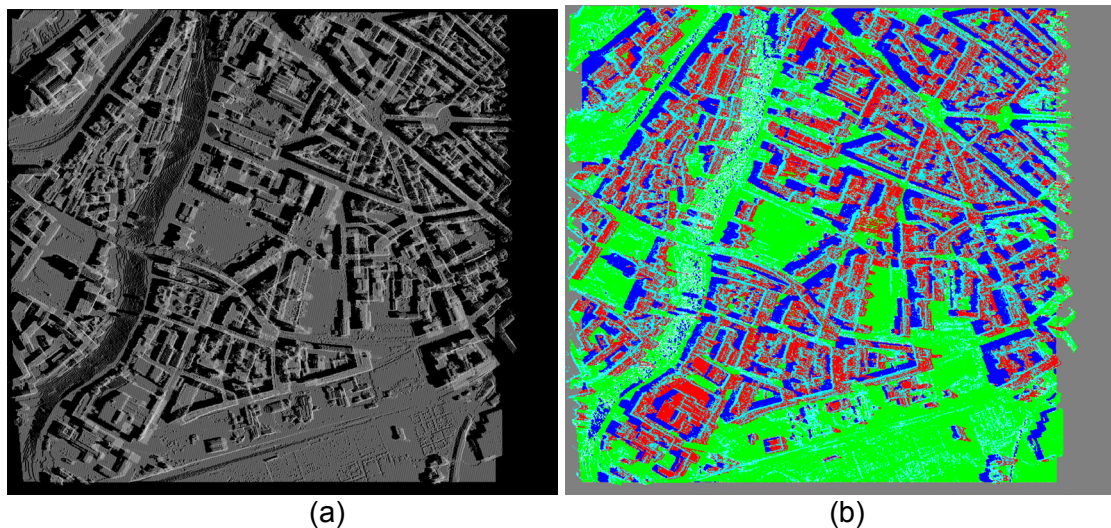
Fig. 6.30: Simulated image and layers for SAR image X1. (a) Simulated image, (b) separate layers (blue: shadow; green: ground; red: layover; cyan: double reflections; grey: background).

Results of distribution fitting and thresholding

The whole DSM is simulated and its layers are generated (see Fig. 6.30). The histograms of the SAR image X_1 in the three layers are shown in Fig. 6.31, with their estimated PDFs presented as lines. These lines approximate the histograms for the proposed application sufficiently, especially for the layover and ground layer. In comparison, the estimated line does not approximate the histogram of the shadow layer that perfectly, indicating the change in the scene. The dark vertical lines in Fig. 6.31 point out the two estimated threshold values. It looks like that these threshold values cannot clearly distinguish the two groups of backscattering. This is mainly due to the complex SAR imaging effect (geometrical and radiometric reflection properties). However, this effect will not affect the change detection method significantly, as only the relative fill ratio will be compared.

The three mean values appear to be very close to each other. This is due to the used log-function for the intensity value. Fig. 6.32 presents the relationship between the real and logarithmic intensity. In fact, the real intensities of the three mean values are 66, 91 and 129. These differences are significantly big enough.

Table 6.14 provides the estimated parameters of different layers in the two SAR images. The different incidence angles lead to slightly different mean values of the three layers.

Table 6.14: Distribution fitting results

	shadow		ground		layover		Threshold value	
	μ	σ	μ	σ	μ	σ	T_{sg}	T_{gl}
SAR X_1 (log)	4,21	0,84	4,52	0,8	4,87	0,82	4,27	4,75
SAR X_1 (real value)	66	-	91	-	129	-	71	115
SAR X_2 (log)	4,18	0,68	4,48	0,65	4,95	0,82	4,25	4,92
SAR X_2 (real value)	64	-	87	-	140	-	69	136
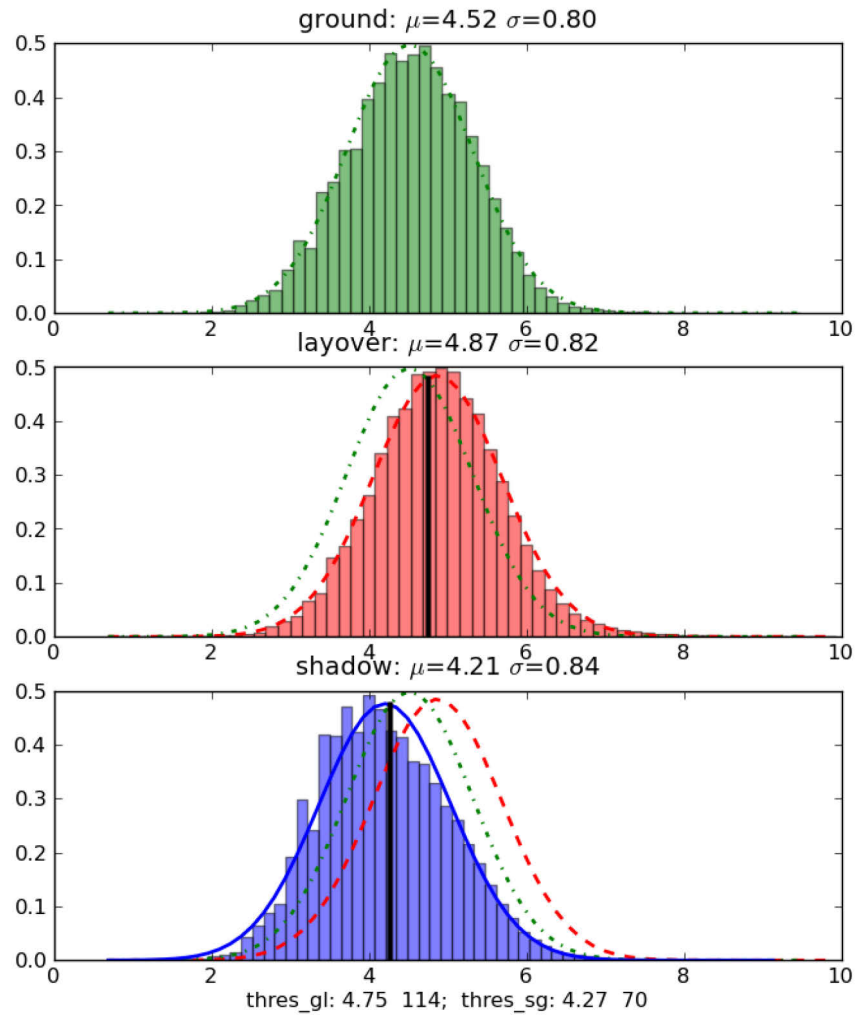
Fig. 6.31: Distribution fitting and thresholding. Three images show the histograms and the estimated PDFs (lines) of the ground, layover and shadow layer of the whole DSM. The black lines in the middle and lower image indicate the threshold value of ground-to–layover and shadow-to-ground layers, respectively.
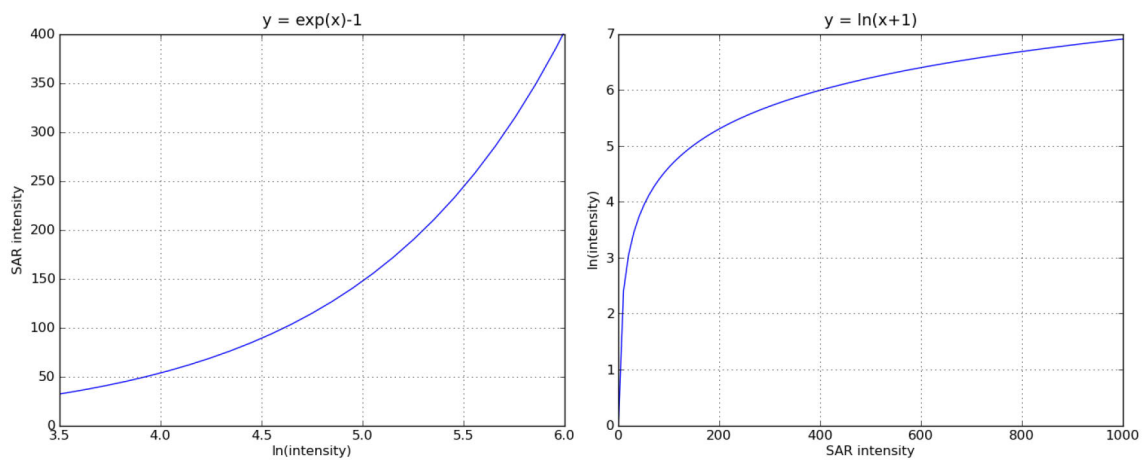
Fig. 6.32: Relationship between the real and logarithmic intensity.
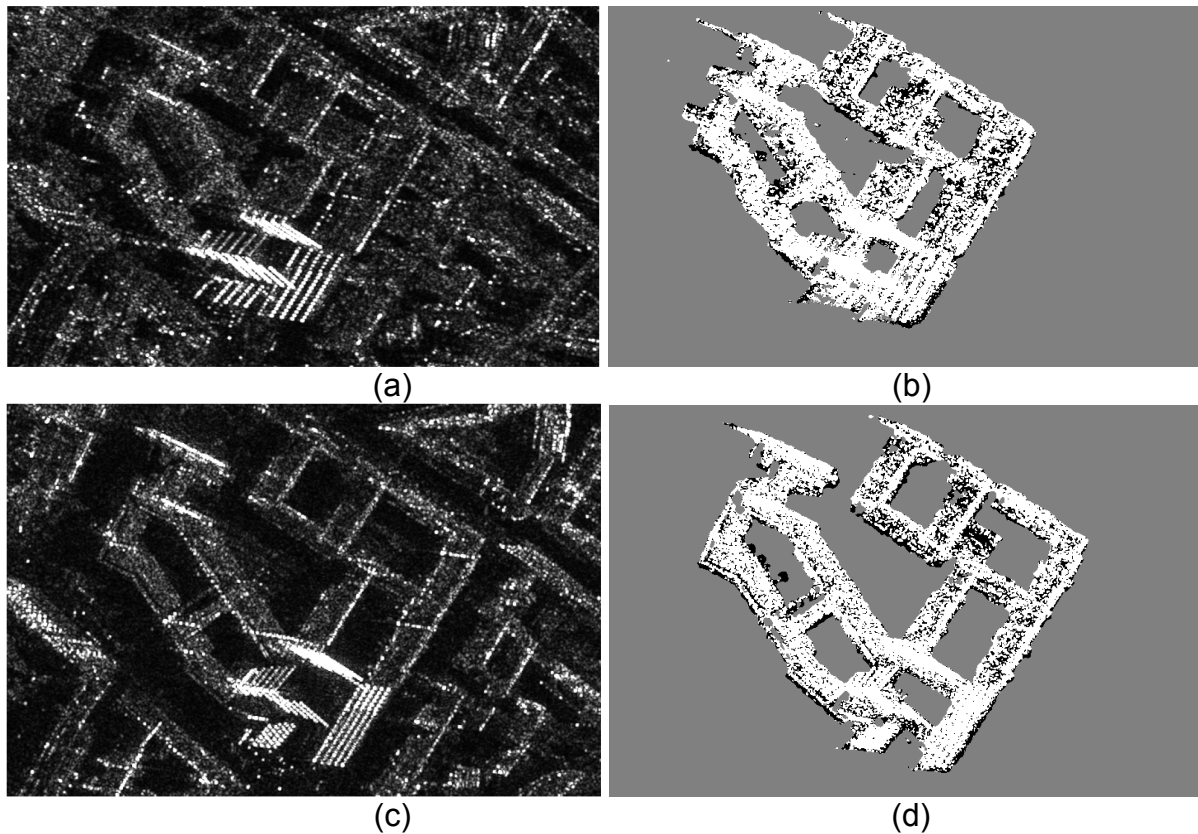
Fig. 6.33: Detailed results for intact building 8. (a) and (b) image subset in TerraSAR-X image X_1 and corresponding layover fill mask. (c) and (d) image subset in TerraSAR-X image X_2 and corresponding layover fill mask.

Detailed results for an intact building example

Fig. 6.33 presents the detailed results of the proposed method for Building 8 (marked in Fig. 6.16a). Although the signatures of the building in the two SAR images are very different, the fill ratios are similar (0.688 in X_1 and 0.676 in X_2), leading to a low change ratio of 0.017. This value indicates that the building is intact.

Detailed results for a demolished building example

Detailed results for the demolished building 26 are provided in Fig. 6.34. The fill ratio of the building layover is changed from 0.693 to 0.318. Consequently, this building was most likely destroyed. In fact, this result is confirmed in the presented pre- and post-event optical images (see in Fig. 6.35). Theoretically, the fill ratio of a demolished building should be "0". This building has a fill ratio of 0.318 instead of 0.0, due to the signatures of a nearby crane (see in Fig. 6.34c).
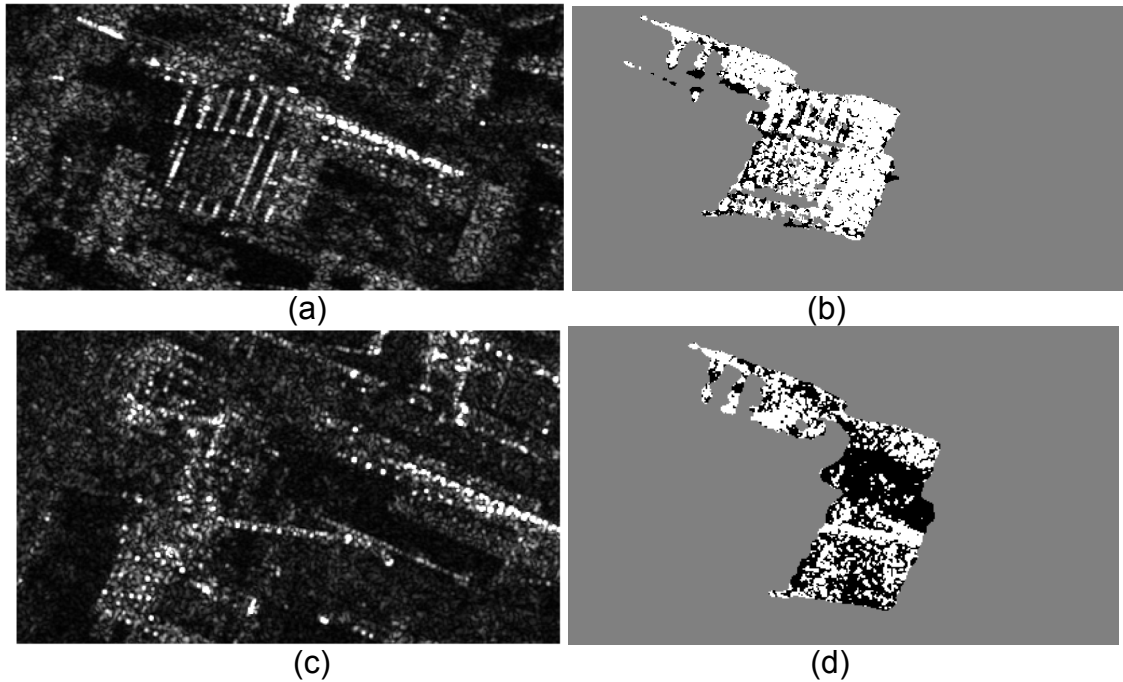
Fig. 6.34: Detailed results for a changed building 26. (a) and (b) image subset in TerraSAR-X image X_1 and corresponding layover fill mask. (c) and (d) image subset in TerraSAR-X image X_2 and corresponding layover fill mask.
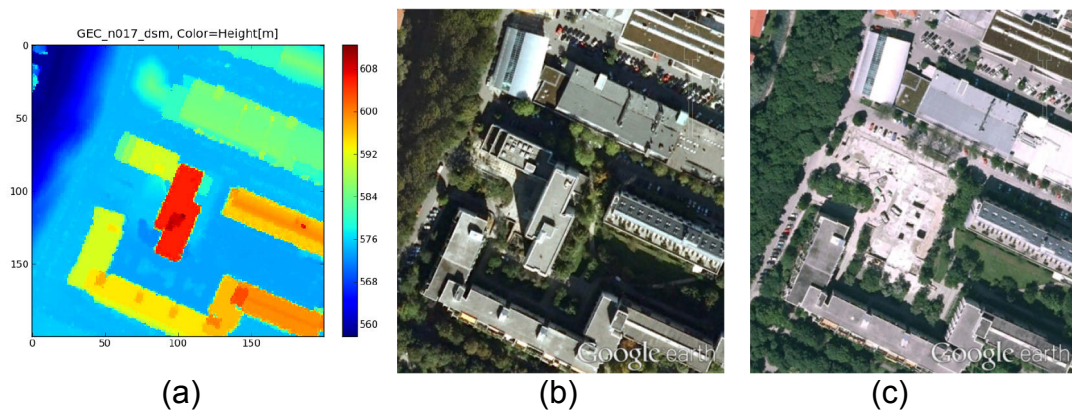
Fig. 6.35: Ground truth of the building 26. (a) subset of the LiDAR data (b) optical image taken on 2007-08-25 (c) optical image taken on 2009-05-23. Both optical images are screenshots from Google Earth [TM] viewer.

Summarized results of all buildings in the data set

Every selected building in the nDSM is simulated and analyzed. Fig. 6.36 shows the layover fill ratio of these buildings in the two SAR images. The layover fill ratio of most buildings ranges from 0.5 to 0.7, which is different from the ideal value '1.0'. This is mainly due to the complex SAR reflection properties (e.g., some part of the layover area of an intact building may also have low intensity values because of specific surface geometry or material of walls). However, as discussed before, this value is similar for both SAR images, making the comparison possible and reasonable.

Fig. 6.37 presents the change ratios of the buildings using the layover, shadow, and both layers. The change ratio of shadow layers varies infrequently. Some of them have the value "0", because of the definition in Equation 6.22. Some change ratios of shadow layer are even higher than the corresponding values from the layover layer, highlighting the sensitivity of

change ratio from the shadow layer. In comparison, the change ratio of layover varies frequently but relatively mildly. The fusion to mean change ratio stabilizes the result.

The histogram of the mean change ratios of all the 81 buildings is presented in Fig. 6.38. The mean change ratio of most buildings ranges from 0.0 to 0.2, close to the ideal value '0'. Three buildings (Building 76, 26, and 75) have significantly greater change ratios (0.597, 0.584, and 0.461) than the other buildings, indicating that they are most likely demolished. Three other buildings (Building 39, 22, 19) have relatively high change ratios, ranging between [0.2, 0.3], indicating that they might be partly changed.

Compared with the ground truth in Table 6.13, a confusion matrix for the change detection results based on building layer fill is provided in Table 6.15. The four buildings (26, 75, 76, and 22) have significantly greater change ratios than the other buildings (see Fig. 6.38) and are correctly detected. The detected building 19 is actually not a false alarm, because the new building N2 (see Fig. 6.28) is nearby and affects its backscattering. The building 39 is a false alarm, resulting from a seasonal change of the trees nearby, which partly cover the building roof. The mean change ratio values are presented as a change ratio map in Fig. 6.39a, which ease the comparison with the ground truth.
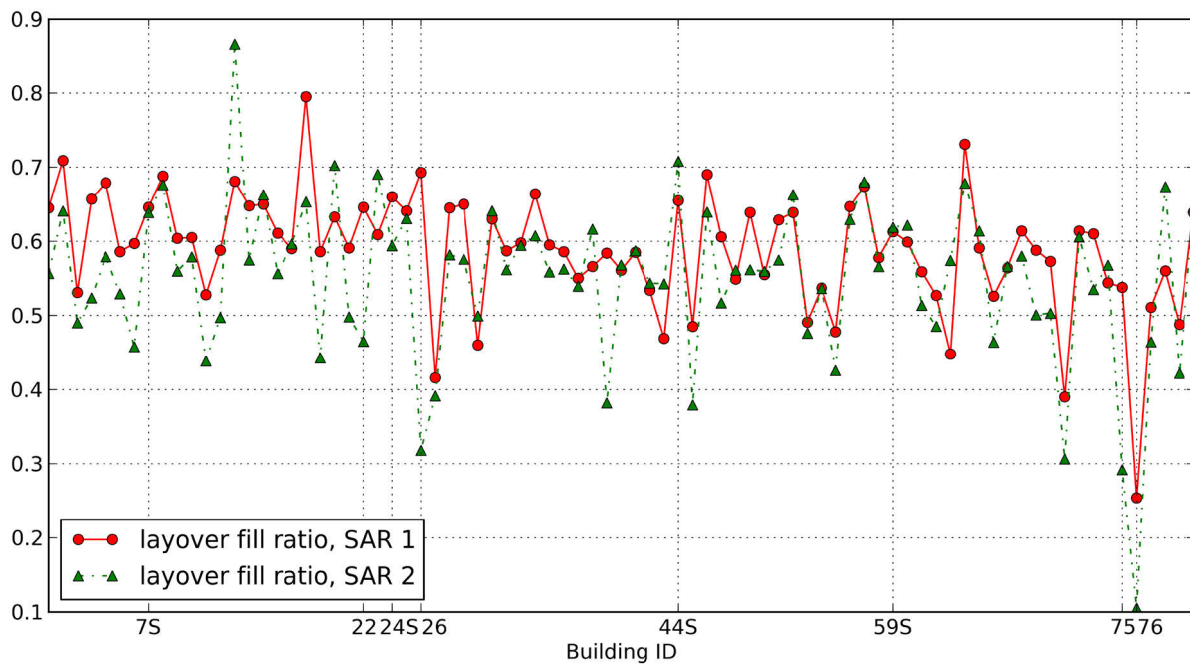
Fig. 6.36: Layover fill ratio of all the buildings according to the two SAR images (the vertical lines mark the eight changed buildings related to Table 6.13, while the buildings with tiny changes are marked with 'S' after their IDs).
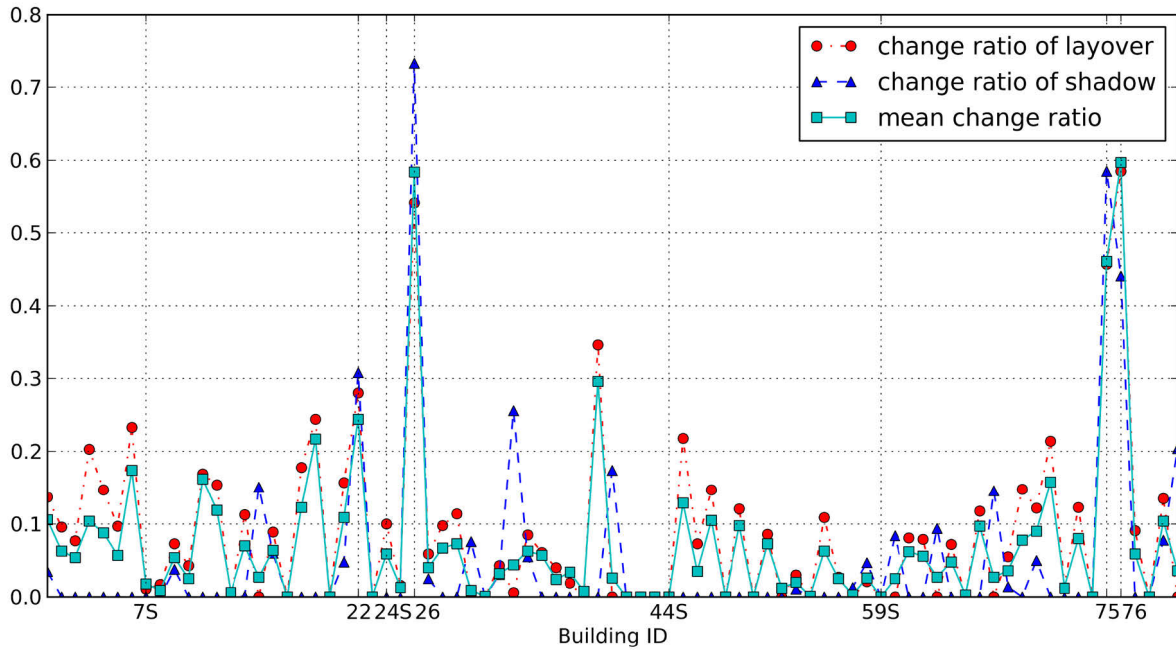
Fig. 6.37: Change ratio of all buildings using layover layers, shadow layers, and the fused result, individually (the vertical lines mark the eight changed buildings related to Table 6.13, while the buildings with tiny changes are marked with 'S' after their IDs).
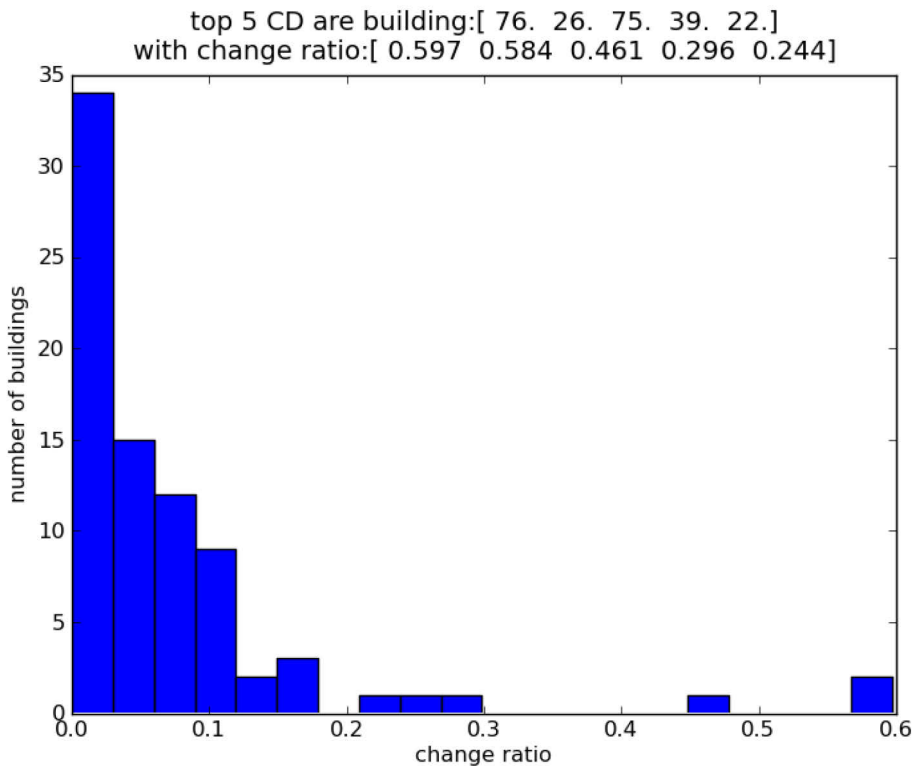
Fig. 6.38: Histogram of the mean change ratio of all the buildings. Most of the buildings have a low change ratio, indicating that they are intact. Three buildings (76, 26, and 75) have a high change ratio, indicating that they are most likely demolished.

Table 6.15: Confusion Matrix, detected buildings and kappa coefficient for the unsupervised change detection based on building layer fill (the values in brackets neglect the four buildings with tiny changes)

Overall accuracy	92.6% (97.5%)	Prediction		Producer's accuracy
Kappa coefficient	0.532 (0.787)	Change	No change	
True	Change {building IDs}	4 {22, 26, 75, 76 }	4 (0) {7, 24, 44, 59}	50.0% (100%)
	No change {building IDs}	2 {19, 39}	71 (75) {other building IDs}	97.4%
User's accuracy		66.6%	94.7% (100%)	

(a) (b)
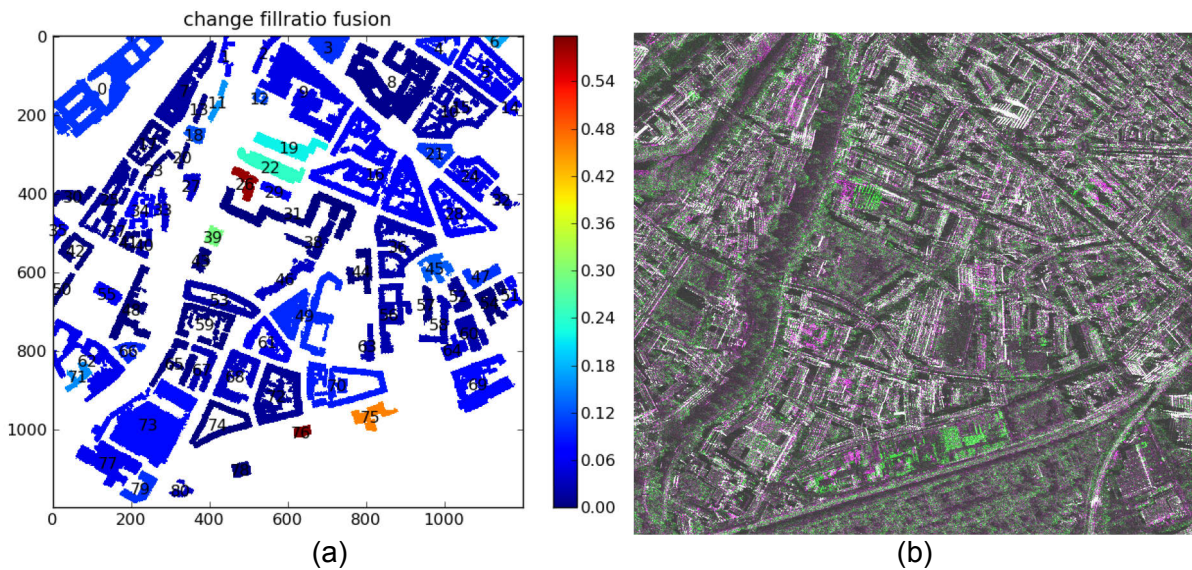
Fig. 6.39: Change detection result. (a) Change ratio map of the Munich test site using the method of building layer fill (color indicates the building mean change ratio). (b) Multi-temporal false color composite of spotlight TerraSAR-X images (Red and blue channel: 2010-01-10, Green channel: 2008-05-26)

Results for non-local filtered SAR image as input

All the previous presented results in this section are based on the original SAR images. Since the backscattering of every pixel related to a building is considered and compared in this algorithm, to reduce the speckle noise, a non-local filter (Deledalle et al. 2009) without iteration is performed for the two input SAR images (see the dashed box in the flowchart of Fig. 6.26). Without changing anything else, the new result is presented in Fig. 6.40. Compared to the Fig. 6.37 and Fig. 6.38, the mean change ratio spreads out significantly so that it is easier to distinguish the demolished and intact buildings. Although the detected buildings with or without the filter are the same in this test site, the non-local filter is suggested for other scenes. Nevertheless, the non-local filter is relatively time consuming (20 minutes for this test scene). In urgent cases, it is suggested to use the algorithm without filter firstly and to improve the result with filter later.
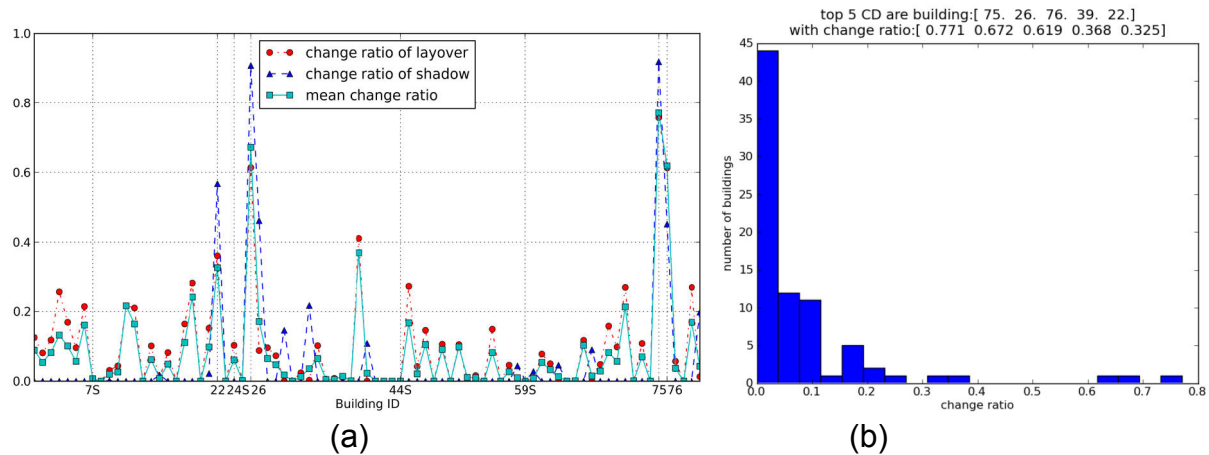
Fig. 6.40: Result of building layer fill based change-detection algorithm with non-local filter. (a) Change ratio of all buildings using layover or shadow layers and the fused result. (b) Histogram of the mean change ratio of all the buildings.

Conclusion

This section has presented a change-detection algorithm of SAR images with different incidence angles based on a simulation technique using a LiDAR DSM as input. The proposed algorithm has defined a new comparison operator: the change ratio based on the fill ratio of building layers. With experimental tests, the operator works well for buildings with different sizes and shapes in complex urban scenarios. Since the operator considers the whole building signatures as one object, small changed buildings cannot be detected. This limitation may be covered by a change-detection algorithm focused on individual walls (see Section 6.5), which is based on the same idea.

6.4 Wall change detection from two SAR images based on point-feature location

Section 6.3 has presented an algorithm for change detection between two SAR images with different incidence angles based on building-layer fill ratio. Since the algorithm considers the whole building as one object, partly changed buildings can hardly be detected.

Because of this, this section will present a wall-level change-detection algorithm based on point feature location. A digital surface model based on LiDAR data is included in order to provide a priori knowledge about the building shape in the SAR images. Based on the simulation results, the layover areas corresponding to individual façades in the SAR images are extracted and compared. To this end, point signatures are extracted within the layover areas and projected into the same geometry. Their positions are then compared with a buffer change-detection algorithm following the idea of Sui et al. (2004). Part of this section appears in Tao et al. (2013).

6.4.1 Methodology

The underlying scenario is that a DSM and two SAR images are captured at times t_0, t_1 and t_2, respectively. The aim is to detect negative changes (i.e., collapsed or demolished buildings) between time points t_1 and t_2. In this context, the basic idea is to focus on changes of façade layover areas in SAR images. The flowchart of the algorithm is presented in Fig. 6.41. To predict the façade layover areas, models of individual buildings and walls are extracted from the LiDAR DSM (see the details in Chapters 4 and 5). The "visible" walls
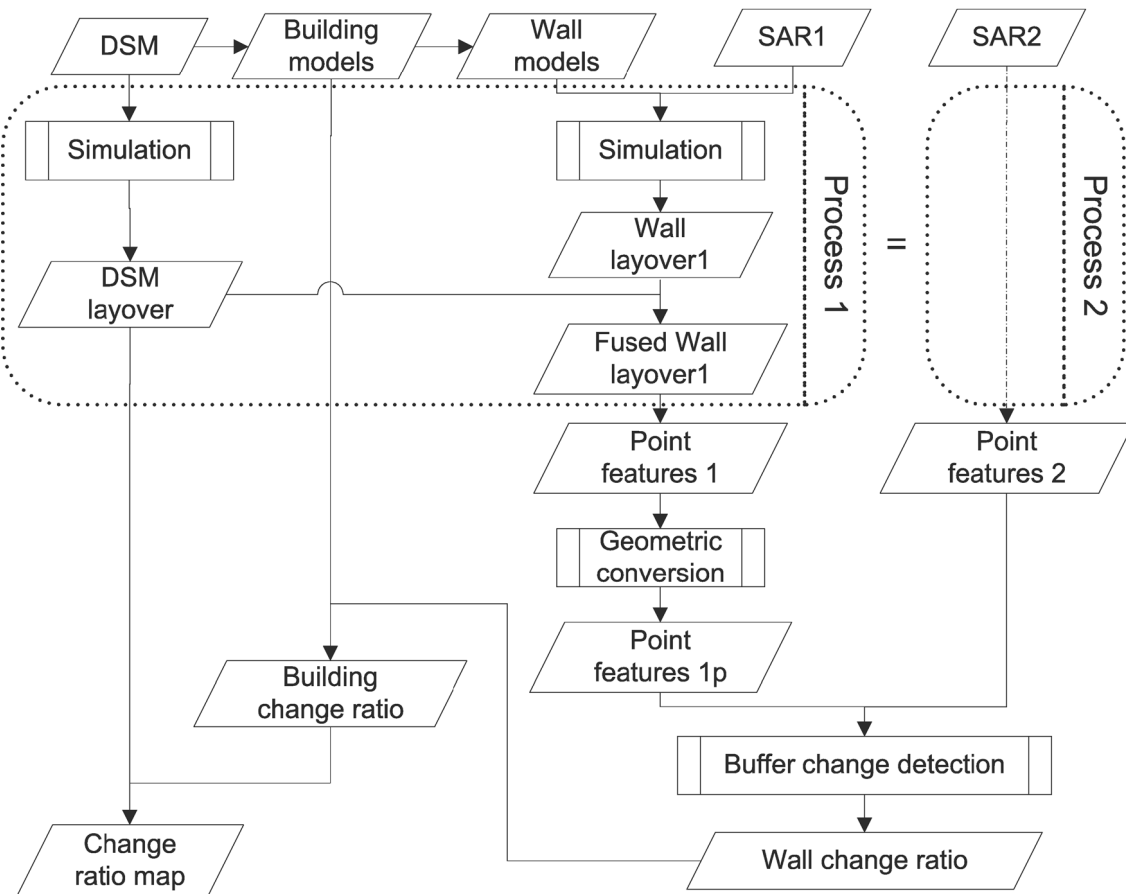
Fig. 6.41: Flowchart of the wall level change detection of two SAR images with different incidence angles based on point-feature location.

(from the SAR sensor's perspective) are selected and simulated. Their fused wall layover areas are generated using the local and global layover layers (see details in Chapter 5). Afterwards, point features from the wall layover areas are extracted and converted to have the same geometry. The converted point features are then compared using the buffer change-detection algorithm to calculate a wall change ratio. Lastly, the wall change-detection results are fused to calculate the building change ratio and analyzed in the DSM level thereafter to detect changed buildings. This fusion step is an option to detect changes on building level.

Selection of proper walls

Based on the algorithm of Section 5.2, all walls with different types (length, height, gradient direction, toward courtyard or street) are extracted. However, not all of them are suitable for the wall change-detection analysis.

First of all, not all of the walls are visible to the SAR sensor. Given a wall with gradient direction of γ and the SAR azimuth angle of α (see Fig. 6.42), the aspect angle ϕ is then defined as:

$$\phi = \left\| (\gamma + 90°) - (\alpha - 90°) \right\| = \left\| \gamma + 180° - \alpha \right\|. \tag{6.25}$$
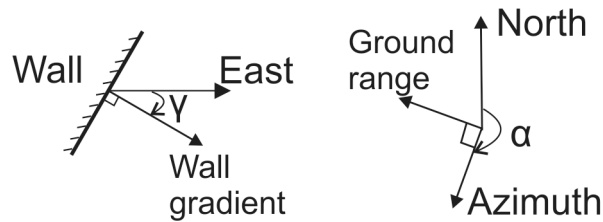
Fig. 6.42: Sketch of azimuth angle α and wall gradient direction γ for calculation of aspect angle ϕ.

The aspect angle is the angle between the wall normal direction (i.e., gradient direction in the wall segmentation step in Section 5.2) and the range direction of the sensor. The aspect angle ranges between [0°, 180°]. If the wall is located parallel to the azimuth direction and faces the sensor, then the aspect angle is 0°. In this case, the wall layover area reaches the maximum. If the aspect angle is greater than 60°, the corresponding signatures of the wall are hardly separable, since the layover area is very narrow in azimuth direction. The walls with aspect angles greater than 90°, are "invisible" to the sensor.

Most of the bright point signatures in SAR images are most likely related to the window corners or balcony corners of building façades. To analyze walls with enough point features, only walls with height (H) and length (L) exceeding defined thresholds are selected. These threshold values are defined according to the local building floor height and window distance. For Munich test sites 10 meter are chosen for both of them.

Finally, a combined parameter is defined for the selection of suitable wall models: the flux area A_{flux}.

$$A_{flux} = L \times H \times \cos(\phi). \tag{6.26}$$

The value of A_{flux} is linear dependent on the wall layover area in the SAR images. Using the four parameters (ϕ, H, L, and A_{flux}) discussed above, relevant walls according to the SAR azimuth direction are chosen for the subsequent analysis.

Wall layover conversion

Using the separated wall models as input for an automatic processing chain based on RaySAR (see Chapter 3), simulated images of the wall models are generated. These geocoded images can be directly compared to the TerraSAR-X GEC products. The simulated wall layover images are converted to binary masks and the corresponding SAR image patches are extracted.

The correspondence of image pixels in wall layover areas and the building façade can be found using the geoinformation of the wall model (the position and gradient direction of the wall) and the projection geometry inherent to the SAR GEC products. Based on this geometric relationship, the extracted wall layover parts of different SAR images are converted to have the same image geometry. This principle is illustrated in Fig. 6.43 and described in the following.

The building wall is assumed to be a vertical plane, which can be described with one point (e.g., wall center point, P_5, with coordinates E_5 and N_5) and one direction (wall median gradient direction, ω). These parameters are provided by the wall extraction step described in Chapter 5. Given the azimuth direction (α_1) and the signal incidence angle (θ_1), a point P1

(with coordinates E_1, N_1, and H_1) in the layover area of SAR image X_1 can be projected to this vertical plane with an intersection point P_0 (with coordinates E_0, N_0, and H_0). Considering the imaging geometry of SAR image X_2 with another azimuth (α_2) and signal incidence angle (θ_2), this point P_0 is then projected to the horizontal plane of the SAR GEC image X_2 with an intersection point P_2 (with coordinates E_2, N_2, and H_2).

To sum up, the given values are as follows: incidence angle, azimuth angle and frame mean height of the two SAR GEC images (θ_1, α_1, H_1, θ_2, α_2, H_2); the wall gradient direction (ω), and wall center point coordinates (E_5, N_5); and any point P_1 in SAR image X_1 (E_1, N_1). The unknown values are the coordinates of its corresponding point P_2 in SAR image X_2 (E_2, N_2).

Due to the SAR imaging geometry, the relationship of a wall point P_0 with coordinate (E_0, N_0, and H_0) and its corresponding points in the 2 SAR images can be described as:

$$
\begin{pmatrix} E_0 \\ N_0 \\ H_0 \end{pmatrix} = \begin{pmatrix} E_1 \\ N_1 \\ H_1 \end{pmatrix} + \lambda_1 \begin{pmatrix} \cos\alpha_1 \\ -\sin\alpha_1 \\ \tan\theta_1 \end{pmatrix} = \begin{pmatrix} E_2 \\ N_2 \\ H_2 \end{pmatrix} + \lambda_2 \begin{pmatrix} \cos\alpha_2 \\ -\sin\alpha_2 \\ \tan\theta_2 \end{pmatrix}. \tag{6.27}
$$

The wall point P_0 is located on the vertical wall model, thus:

$$
\begin{pmatrix} \cos w \\ -\sin w \end{pmatrix} \bullet \begin{pmatrix} E_0 - E_5 \\ N_0 - N_5 \end{pmatrix} = 0. \tag{6.28}
$$

These two equations can be converted to (i.e., E_0 and N_0 in Equation 6.28 are substituted by the first two lines of the first part in Equation 6.27, and it is solved for λ_1. Using the third line in Equation 6.27, λ_2 can be obtained.):

$$
\begin{aligned}
\lambda_1 &= \frac{\cos\omega(E_5 - E_1) + \sin\omega(N_1 - N_5)}{\cos(\omega - \alpha_1)} \\
\lambda_2 &= \frac{H_1 - H_2 + \lambda_1 \tan\theta_1}{\tan\theta_2} \\
E_2 &= E_1 + \lambda_1 \cos\alpha_1 - \lambda_2 \cos\alpha_2 \\
N_2 &= N_1 - \lambda_1 \sin\alpha_1 + \lambda_2 \sin\alpha_2.
\end{aligned} \tag{6.29}
$$

Using the Equation 6.29, all pixels in a wall layover area can be converted from one SAR imaging geometry to another.

It is worth noting that the assumption of a planar wall may lead to errors in the conversion. In reality, not all façade structures related to point signatures will be arranged in a plane. Accordingly, the error of the converted point position is proportional to the distance between the real point and the assumed vertical plane.
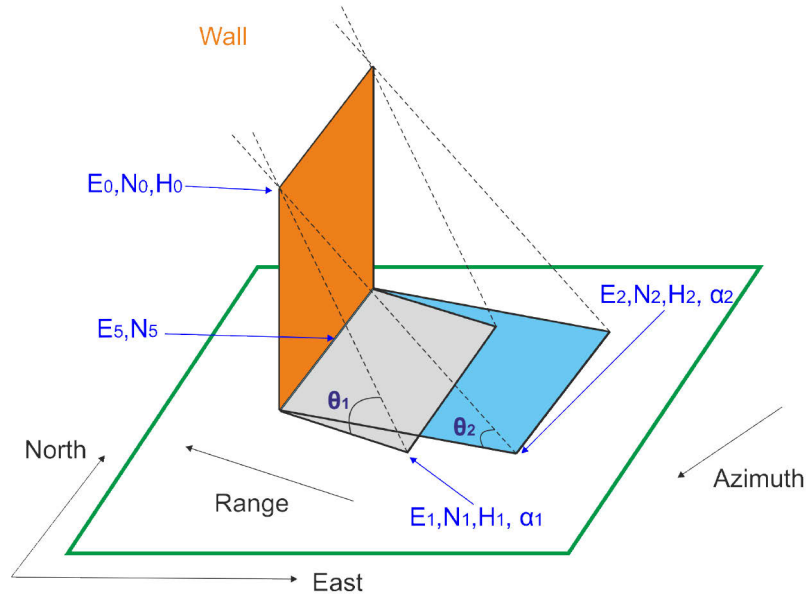
Fig. 6.43: Geometry of the wall layover conversion.

Buffer change detection based on point features

The previous steps provide wall models and the geometrical relationship between wall layover images for different imaging geometries. For comparing them, a buffer change detection method is used which follows the idea of Sui et al. (2004). This method was originally developed for geographic information system (GIS) applications (e.g., for comparing road maps). For the change-detection approach proposed in this section, point features (local maxima within the wall layover) are compared. The processing follows four main steps:

1. The local maxima of the two SAR wall layovers are extracted. The maxima points with low intensity (e.g., < 700) are less important and are discarded.
2. The extracted point features from SAR image X_1 are converted to the second SAR imaging geometry using the method described above.
3. For every converted point of SAR image X_1, its Euclidean distances to all point features of SAR image X_2 are calculated. In case at least one distance is smaller than a pre-defined buffer distance (see discussion later in this section), the point is considered as being "inside". Otherwise, it is an "outside" point.
4. The third step is conducted for all converted points (with a total number of L_{total}). The number of "inside" points is L_{inside}. The change ratio is then defined as:

$$P_{point} = 1 - \frac{L_{inside}}{L_{total}}. \tag{6.30}$$

The buffer distance used in the third step mainly depends on the accuracy of the wall center point coordinates, the wall gradient direction, the assumption of planar façades, and the accuracy of the extracted local maximum points. Furthermore, using the procedure described previously in this section, the propagation of uncertainty of the converted point positions (E_2, N_2), depending on the input parameters [wall direction (ω), wall center point position (E_5, N_5), and position of extracted local maximum points (E_1, N_1)], are calculated. Based on this, the buffer distance for every wall model is calculated, resulting in buffer values between 2 and 6 pixels.

Lastly, the wall change results are fused with the wall areas as weight to provide a building change result. The results are then converted to a change map of the whole DSM. This method can also be used to detect the demolished buildings, with the same aim as the algorithm described in Section 6.3. However, due to the complexity of the calculation of this algorithm (mainly on the wall extraction and wall simulation), it is suggested to combine the algorithms of Section 6.3 and 6.4. That means, using the algorithm of Section 6.4 only to analyze the buildings with relatively high change ratio or specific buildings of interest, in order to identify the demolished walls of the partly changed buildings.

6.4.2 Experimental results

To indicate the potential of the proposed approach, experiments were carried out on the same data set described in Section 6.3.2. Although 81 buildings (see Fig. 6.16a) are extracted from the provided LiDAR DSM, some of them cannot be processed by this algorithm, since they do not include walls with proper size (height, length, aspect angle and flux area).

Results of a demolished building (Building 26)

As an example, Building 26 is selected for detecting changes. It is shown in Fig. 6.44. Using the method described in Section 5, individual wall models are extracted from this building model. Fig. 6.44b shows the wall masks with their wall IDs. Altogether ten walls are extracted from this building. The walls will be named "{building ID}_{wall ID}". For example, Wall 26_5 means the 5th wall of Building 26 in the DSM.

Additionally, the wall parameters are calculated (see Table 6.16). As the azimuth angles of the two input SAR images are approximately 188°, only the walls 1-5 are "visible" to the SAR sensor. The walls 26_1, 26_2, and 26_4 have aspect angles greater than 50° relative to the sensor. Their corresponding signatures are hardly separable as the layover areas are very narrow in azimuth. Only the walls 26_3 and 26_5 are of relevant size (e.g., length and height > 10m) and are chosen for the layover change detection.
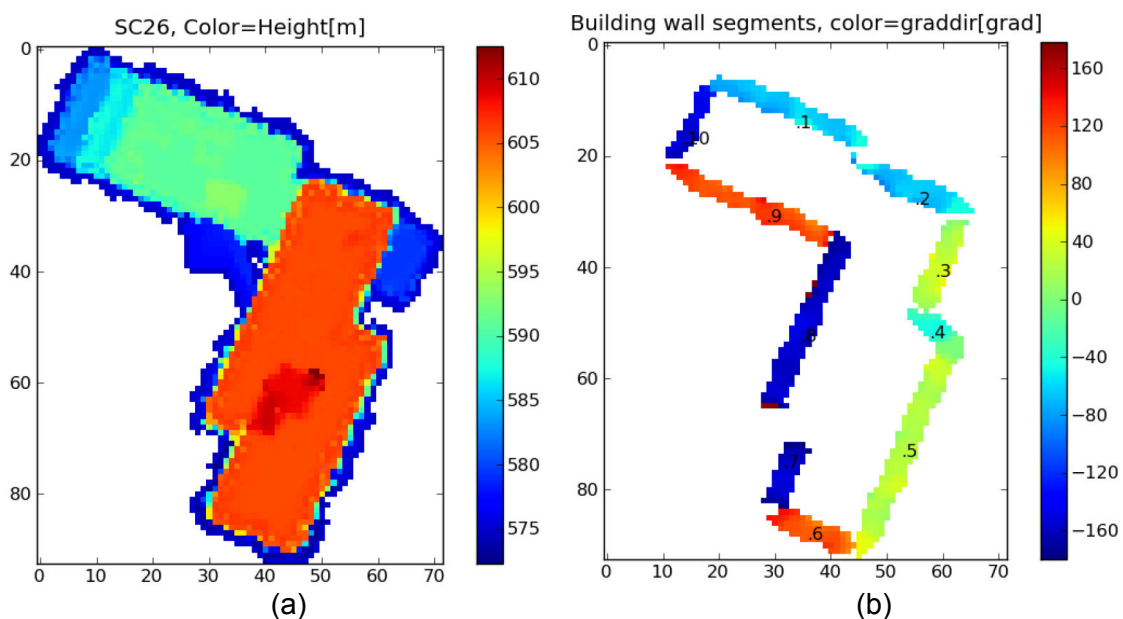
Fig. 6.44: Wall extraction from the building model 26. (a) Building model with color indicating height, (b) extracted wall masks with wall IDs, color indicates gradient direction.

Table 6.16: Wall parameters of building 26

wall id	gradient direction [degrees]	Aspect angle [degrees]	wall length [m]	height [m]
1	-64,6	73,4	29,5	18,4
2	-64,9	73,7	20,1	28,9
3	24,1	15,3	18,4	26,7
4	-44,1	52,9	7,1	19,4
5	24,9	16,1	40,7	31,3
6	112,9	104,1	15,7	31,3
7	-152,5	161,3	17	26,5
8	-157,1	165,9	32,6	26,6
9	115,2	106,4	30,4	18,3
10	-145,9	154,7	14,3	18,3

The corresponding part of the chosen wall mask in the DSM is extracted as a wall model. This wall model is simulated and the resulting layover image is geocoded. Thereafter, the wall layover is converted to a mask and the corresponding real SAR image is extracted. Fig. 6.45 (a) and (b) show the layover of the wall 26_5 in two SAR images. The red points indicate the extracted local maxima from the SAR image. The cyan circles in Fig. 6.45b indicate the projected positions of the red points from Fig. 6.45a. Only a few projected points (cyan) in Fig. 6.45b correspond to near red points. The change ratio for the wall 26_5 is 0.889, which means 88.9% of the converted points are "outside". This result indicates that this wall is most likely demolished.

The wall change-detection results can be fused to calculate the change ratio of the building. To this end, different weights for the fusion of wall results can be chosen: number of wall points, area of wall, or flux area of wall. The processing using the first weight (number of wall points) yields reasonable and good result. For practical use of this method, if a building includes many walls, it is suggested to fuse only the results of several selected walls (e.g., five walls with the highest number of points) to reduce the processing time. The fused change ratio of Building 26 is 0.912.

Results of an intact building (Building 8)

Compared to the detected negative change of Building 26, Fig. 6.45 (c) and (d) show the intact Wall 8_20 of Building 8. As shown in Fig. 6.45d, most of the converted points (cyan) have a red point nearby, indicating that they are still present. However, some points (e.g., on the right side of Fig. 6.45c) are "outside", as they are signatures related to an adjacent wall. The change ratio of this wall is 0.395. After the fusion with the other wall results the change ratio of Building 8 is 0.378.

Results of a possible false-alarm building (Building 38)

Not all buildings provide a dominant point pattern similar to the example of Wall 8_20. The point features in a SAR image are dependent on different geometric and radiometric properties of the buildings and façades (balconies, roughness, material, etc.). Fig. 6.45ef presents the wall layovers of the intact Wall 38_2. Only 49 point features can be found in Fig. 6.45e, whereas a clear point pattern with 100 points can be seen in Fig. 6.45f. The change ratio of this building is relatively high (0.776). This is mainly related to the different incidence angles. The window corners leading to the point features might not be visible from one of the SAR images because of the occlusion of balconies. This results in a systematic error of this

(a) 26_5

(b) 26_5

(c) 8_20

(d) 8_20

(e) 38_2

(f) 38_2
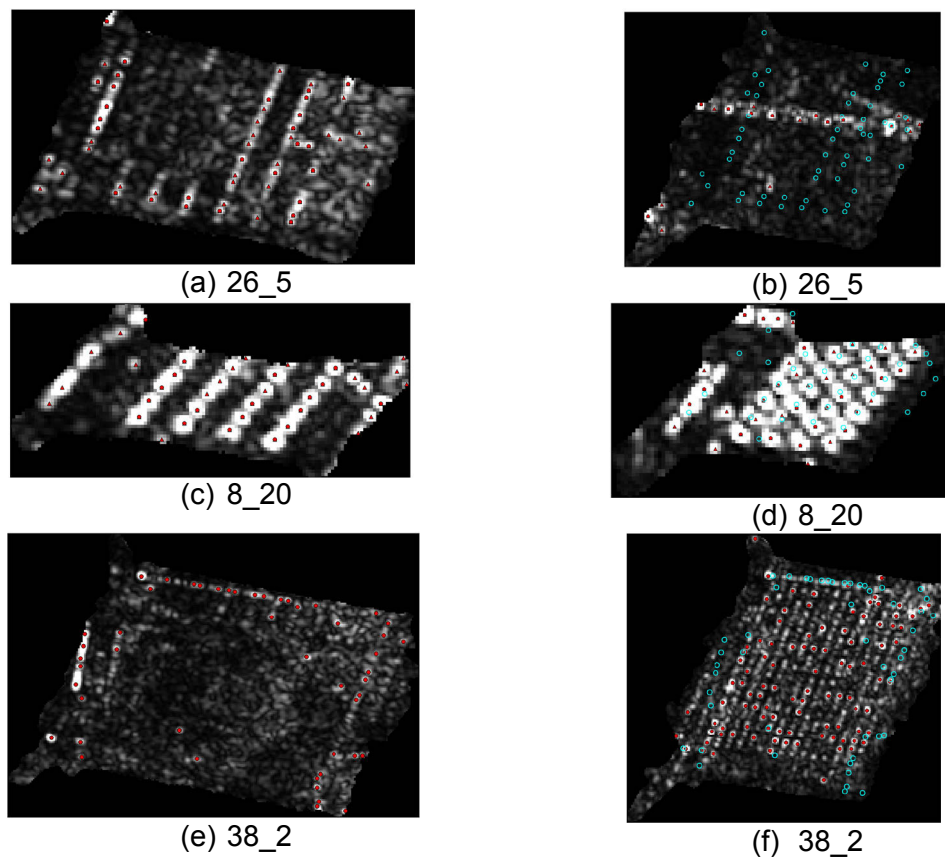
Fig. 6.45: SAR images with original and converted local maxima of different walls. (left) SAR image, 2008-05-26, 25°, (right) SAR image, 2010-01-05, 39°. (a,b) demolished Wall 26_5, (c,d) intact Wall 8_20, (e,f) intact Wall 38_2. The red points are the originally extracted point features. The cyan points in the right images are the converted points from the corresponding left images.

algorithm. Besides this, not all the walls appear in SAR images with many point features. Having a low number of points leads to results with low reliability or even to false alarms.

Results of all buildings in the data set

Table 6.17 summarizes the buffer change detection results of several selected walls. An ideal change ratio for an unchanged building should be zero. Most of the unchanged buildings in this table have a change ratio varying from 0.1 to 0.6. The main reason is that the algorithm has only considered the main impact of different incidence angles – the scaling of wall layover. In contrast, the other effects (e.g., different occlusions, mixture of signatures from other objects) are not covered, leading to "outside" points for every tested building.

Some of the walls have regular point patterns in their layover area (e.g., wall 8_20). This kind of walls have significant low change ratio than the walls without point pattern. Besides this, the change ratio of walls belonging to the same building can still vary slightly (for example the different walls of Building 8). A fusion of them will make the change ratio of the building relatively stable.

Table 6.17: Buffer change detection results of several selected walls

Wall properties	Wall name	Number of points from SAR X_1	Number of "inside" points	Change ratio
Wall with point pattern	8_18	100	68	0.320
	8_20	38	26	0.316
	8_58	40	34	0.150
	8_62	39	35	0.103
Wall without point pattern	49_2	100	45	0.550
	61_2	44	16	0.636
Possible false alarm	38_2	49	10	0.796
Demolished	26_3	45	0	1.000
	26_5	54	6	0.889

The fused change ratios of the buildings in the DSM are plotted in Fig. 6.46. The corresponding histogram is presented in Fig. 6.47. The change ratio of most buildings ranges between 0.4 and 0.7. Building 26 has a significantly high change ratio of 0.912. For a final change decision, the suggested decision rule of the change ratio may be: change, 0.8-1.0; unchanged, 0-0.7; and change candidate, 0.7-0.8. An additional change detection algorithm may help to further categorize the change candidates. Based on this rule, the building 26 has changed, while the buildings (74, 54, 38, and 43) are change candidates.
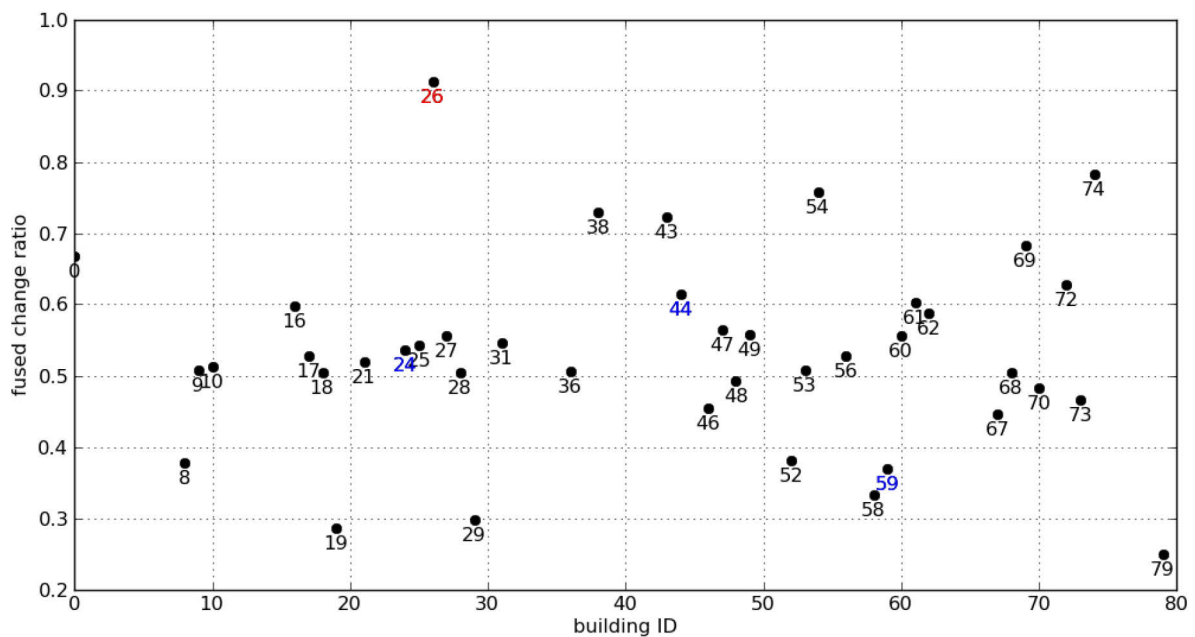
Fig. 6.46: Plot of building change ratios using point feature location (the red and blue color represented IDs refer to the buildings with large and tiny changes, see ground truth in Table 6.13).
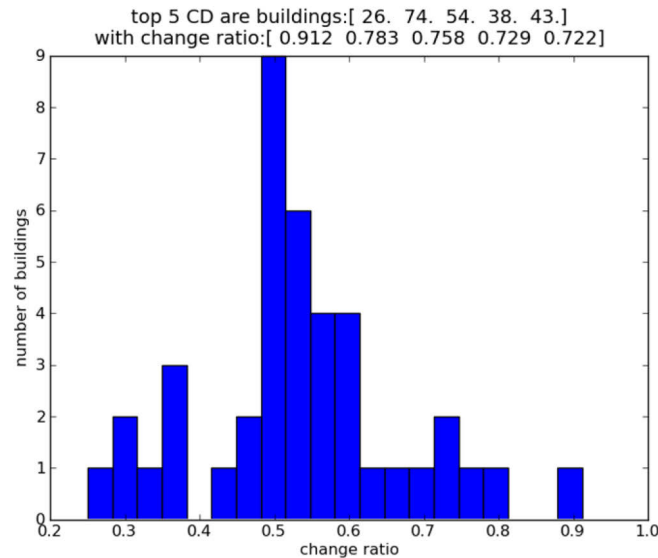
Fig. 6.47: Histogram of the fused change ratio of all the buildings using the algorithm based on point feature location. Most of the buildings have a relatively low change ratio (0.5), indicating that they are intact. The building 26 has significant high change ratio (0.9), indicating that it is most likely demolished.

The change ratio map of the algorithm based on point feature location is presented in Fig. 6.48a, with the same reference data as Fig. 6.39. Some of the buildings do not include proper walls for processing, so they are marked only with building IDs without color in the change ratio map.

Considering Table 6.13 and the optical images in Fig. 6.28, the demolished buildings are 26 and 75, while the rebuilt buildings are 76 and 22, besides four buildings (44, 7, 24, and 59) with tiny changes.

After comparing with the ground truth data, the change-detection result is analyzed and summarized in Table 6.18. Unfortunately, Most of the changed buildings (buildings 75, 76, 22, and 7) were not processed by the algorithm described in this section, since they do not include walls with required conditions. The demolished building 26 has the highest change ratio and is correctly detected. The buildings (24, 44, and 59) with tiny changes are not detected. The four buildings (74, 54, 38, and 43) have relatively high change ratios but are actually intact. This is mainly due to different effects (e.g., different occlusions, mixture with signatures from other objects) which are not covered by the change-detection algorithm.

Table 6.18: Confusion Matrix, detected buildings and kappa coefficient for the unsupervised change detection based on point feature location (the values in brackets are related to the neglect of three buildings with tiny changes)

Overall accuracy	82.9% (90.2%)	Prediction			Producer's accuracy
Kappa coefficient	0.128 (0.305)	Change	No change	Unprocessed	
True	Change {building IDs}	1 {26 }	3 (0) {24, 44, 59}	4 {75,76,22,7}	25.0% (100%)
	No change {building IDs}	4 {38, 43, 54,74}	33 (36) {other buildings}	36	89.2% (90.0%)
User's accuracy		20.0%	91.7% (100%)		
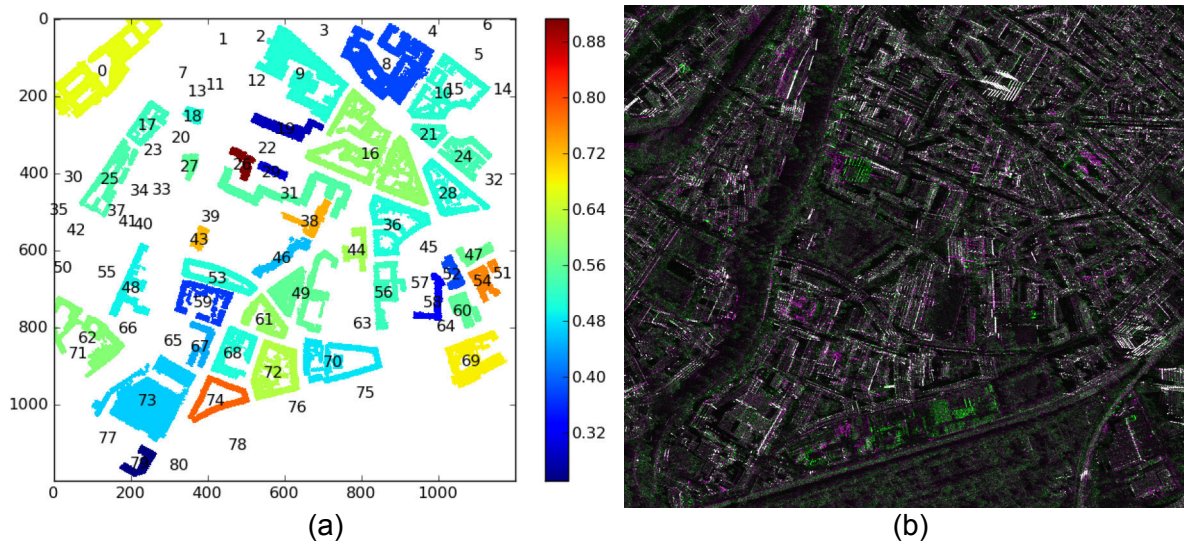
Fig. 6.48: Change detection result of algorithm based on point feature location. (a) Change ratio map of the Munich test site using the method of point feature location (color indicates the building fused change ratio). (b) Multi-temporal false color composite of spotlight TerraSAR-X images (Red and blue channel: 2010-01-10, Green channel: 2008-05-26)

Discussion and conclusion

This section presented a method for detecting changes between two high resolution TerraSAR-X images captured with different incidence angles. Individual building wall models are extracted from a LiDAR DSM and are used to predict their shape in real SAR images with the support of a SAR simulator. The two SAR image sections corresponding to the same building façade are extracted. Thereafter, the detection of changes is based on the comparison (buffer change detection) of local maximum points which are converted to have the same geometry.

The proposed algorithm is applicable for identifying negative changes within the first available SAR dataset after an unexpected event, what may support urgent situations, e.g., the assessment of building damages.

In this context, several limitations are of relevance. First, the method is based on point features in wall layover areas which might be influenced by signatures coming from roofs, grounds or other adjacent objects. Second, the difference of incidence angles may lead to disappearance of the points because of occlusions, possibly resulting in false alarms in the results. Third, the reliability of the result is dependent on the number of extracted points. Walls with few points may not provide reasonable results or even cannot be processed. Moreover, the step of "wall layover conversion" is very sensitive to the accuracy of the LiDAR data. A small error in the LiDAR data may lead to false results. Finally, any changes between the acquisition time of LiDAR and the first SAR image are not considered in this approach.

Nonetheless, the proposed method enables to give hints on building changes and offers an approach for detecting changes of façades despite a variation of the imaging geometry. The algorithm analyzed the point features related to window corners. Therefore it might provide specific information (e.g., the change of building floors) which can be hardly provided by other algorithms.

So far, the method has been tested for different building blocks in Munich and shows promising results. The algorithm will perform better in case of higher resolution SAR images and LiDAR data. The buildings in high resolution SAR images will be represented by more

point features and provide more reliable results. High resolution of LiDAR data will improve the accuracy of the layover conversion step. To detect wall changes with present SAR images like TerraSAR-X, the wall fill position based algorithm (see Section 6.5) might provide better result.

6.5 Wall change detection of two SAR images based on fill position

The algorithm described in Section 6.3 can detect completely demolished buildings but not partly demolished buildings. In Section 6.4, a wall-level algorithm indicates wall changes. However this algorithm relies strongly on the extracted point features thus it is not suitable for all kinds of buildings. By combining the comparison operator of Section 6.3 and the processing structure of Section 6.4, a novel wall change detection algorithm has been developed and will be presented in this section.

The main aim of this algorithm is to detect demolished walls in partly demolished buildings. As an option, the wall change-detection results can be fused to provide a building change-ratio map.

6.5.1 Methodology

The flowchart of the proposed algorithm is presented in Fig. 6.49. This flowchart is the result of the combination of the flowcharts in Fig. 6.26 and Fig. 6.41, which present the two related algorithms.
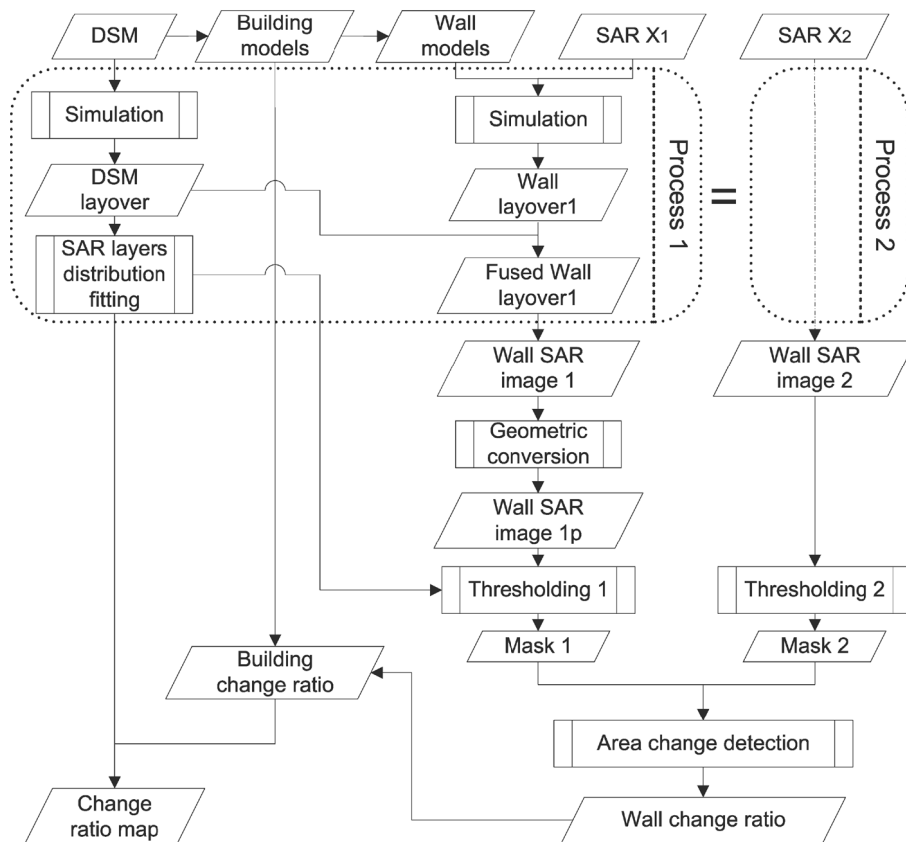
Fig. 6.49: Flowchart of the wall-level change detection of two SAR images with different incidence angles based on the fill position.

The input data of the algorithm includes a DSM and two SAR images (X_1, X_2) acquired with different incidence angles. Equal to the method in Section 6.4.1, the fused wall layover areas are simulated for every selected wall model. The only difference is that the walls are selected with only one requirement: they should be "visible" from the SAR sensor. The wall parameters height and length are not important in this context.

Afterwards, the corresponding SAR image patch of a wall in X_1 is converted to have the same geometry of SAR X_2 following Equation 6.29 in Section 6.4, where the converted image is resampled with bicubic interpolation.

This converted image patch of X_1 and the corresponding patch of X_2 are then converted into two binary masks F_{1gl} F_{2gl} using two threshold values individually. These threshold values are derived from the DSM layers following the method described in Section 6.3.1.

Thereafter, two kinds of wall change ratio can be calculated using the masks F_{1gl} F_{2gl}. The first change ratio is based on fill ratio, which follows the same idea of Equation 6.20 and Equation 6.22 in Section 6.3.1:

$$r_{1l} = \frac{A_{1lf}}{A_{1l}}, \; r_{2l} = \frac{A_{2lf}}{A_{2l}}, \; P_{wf} = 1 - \frac{r_{2l}}{r_{1l}}, \tag{6.31}$$

where A_{1l} and A_{2l} are the area of the building fused layover in the two SAR images; A_{1lf} and A_{2lf} are the area of the filled layover region; r_{1l} and r_{2l} denote the fill ratio of the two layover regions; and P_{wf} is the change ratio based on the fill ratio. For this fill-ratio-based change ratio, the layover conversion is actually not necessary, since the fill-ratio of image patch X_1 will stay the same without conversion.

The second change ratio is based on the position of the layover fill area. If the filled area (i.e., number of pixels with value "1") in mask F1gl is defined as A1lf, the area of intersection mask of F1gl and F2gl (i.e., number of pixels with value "1" in both masks) is defined as A1lfi, the change ratio based on layover fill position is then defined as

$$P_{wa} = 1 - \frac{A_{1lfi}}{A_{1lf}}. \tag{6.32}$$

The fill-ratio-based change ratio does not consider which part of a wall layover is filled, which might lead to false alarms (see example in Fig. 6.50). This task may be covered by the fill-position-based change ratio.

Lastly, as an option, the wall change ratio results can be fused (using the area A_{1lf} as weight) to derive a building change ratio and analyzed on the building-level thereafter in order to detect demolished buildings.

		Fill ratio	Fill position
F_{1gl}	▮▮▮▮□□□	$r_{1l}=0.5$	$A_{1lf}=0.5A_{1l}$
F_{2gl}	□□□▮▮▮▮	$r_{2l}=0.5$	$A_{1lfi}=0.0A_{1l}$
Change ratio:		$P_{wf}=0$	$P_{wa}=1$
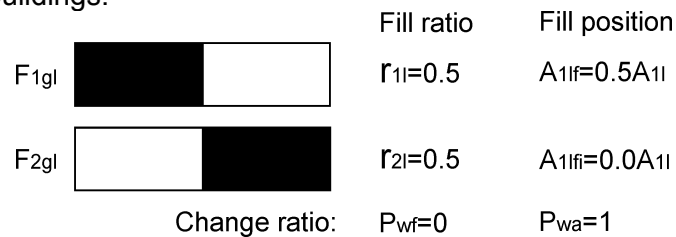
Fig. 6.50: Sketch of an example of change ratios based on fill ratio and fill position. The fill-position-based method detects the change in the sketch correctly whereas the fill-ratio-based method does not.

6.5.2 Experimental results

Data set description

Experiments were carried out on the same data set described in Section 6.3.2, so the acquisition times and parameters of the input data are the same as before. To indicate the potential of the proposed approach, a different and smaller test site in Munich including a partly demolished building is selected. The input data (one DSM and two SAR images) are presented in Fig. 6.51abc.

A false-color composite of two SAR images is generated and presented in Fig. 6.51d. The magenta color indicates increased signals while the green color denotes decreased signals. Additionally, by comparing two optical images from Google Earth, the ground truth data is manually extracted and presented in Fig. 6.52. The two kinds of ground truth data confirm that three segments of a building complex are demolished, which are marked with red lines in Fig. 6.52.
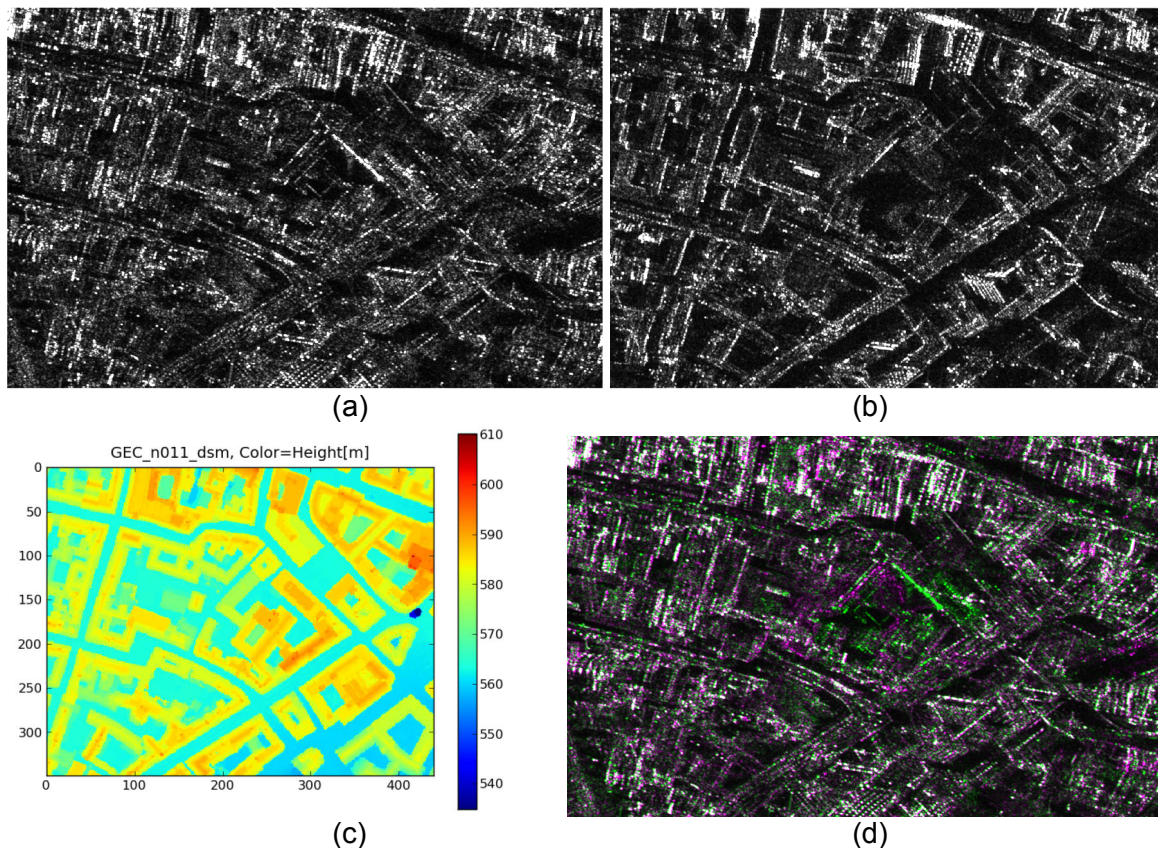
Fig. 6.51: The input data of Munich center and corresponding reference data: (a) TerraSAR-X image 2008-05-26, incidence angle 25°, (b) 2010-01-05, incidence angle 39°, (c) LiDAR digital surface model 2003-04, (d) Multi-temporal false color composite of spotlight TerraSAR-X images as reference (Green channel: 2008-05-26, Red and blue channel: 2010-01-10, both with incidence angle 25°).

(a)   (b)
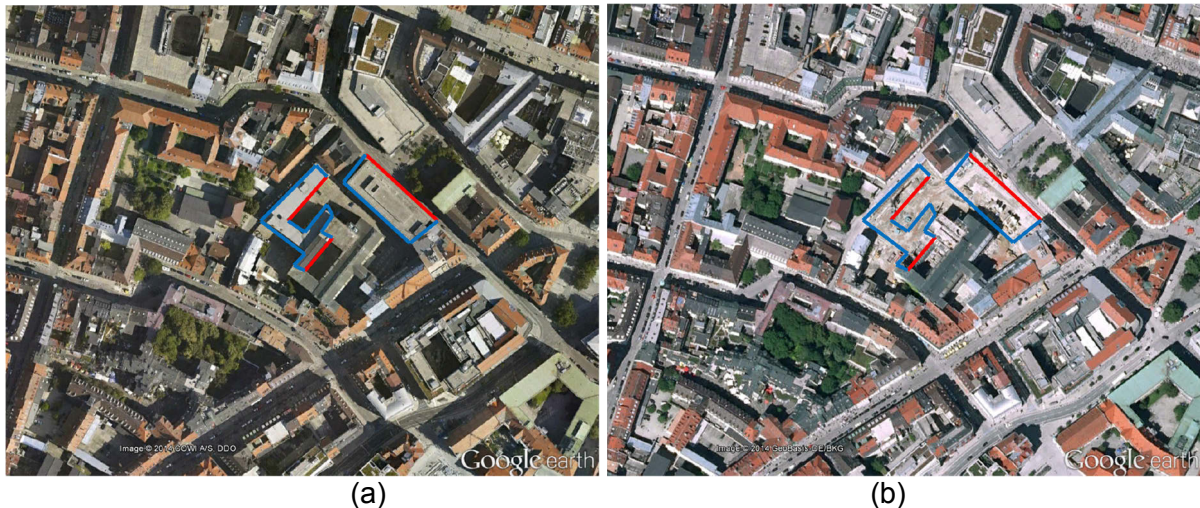
Fig. 6.52: Ground truth data of change detection derived by visual interpretation of Google Earth images. (left) 2004-08-29, (right) 2009-05-23. The demolished building segments are marked with colored polygons, while the red lines denote demolished walls visible from the SAR sensors' perspective.

Results of building 6

Altogether 15 isolated buildings (see Fig. 6.58a) were extracted from the DSM. Building 6 is the largest building in this DSM (see Fig. 6.53). It includes two main parts and totally 94 separated wall segments. The separated wall segments with their ID numbers are shown in Fig. 6.53.

For all of the 16 "visible" walls, two change-ratio values (based on fill-ratio and fill-position) were calculated. These wall change-ratio values are plotted in Fig. 6.54 and presented as histograms in Fig. 6.55. The fill-ratio-based change-ratio ranges between [-0.2, 0.6]. Most of the change ratio are smaller than 0.2. The fill-position-based change ratio varies between [0.2, 0.8], with most of the values being lower than 0.5. The change ratio map of building 6 and the corresponding optical reference image are presented in Fig. 6.56. Based on the optical reference images, the "visible" walls according to the three demolished building segments are 37, 48 and 80. The change ratio values of these three walls are "0.772, 0.631, and 0.619" for the fill-position-based method and "0.405, 0.531, and 0.451" for the fill-ratio-based method. These change-ratio values are higher than that of the rest intact walls, showing the good performance of the proposed algorithm. In comparison with the fill-ratio-based method, the fill-position-based method provides a result which is slightly better differentiable (see Fig. 6.55). Besides this, more change situations (e.g., rebuilt wall) are considered with the fill-position-based method, it is thus preferable for the wall-level change detection.

Nevertheless, several factors might affect the wall change-detection results. Because of the step of wall layover conversion, the fill-position-based algorithm is sensitive to the DSM resolution and the accuracy of the extracted wall parameters (wall center point position, wall gradient direction). Besides, any change of the roof (e.g., material, structure) or neighboring buildings might also affect the result since the walls are individually analyzed in the proposed algorithm. For example, the change ratios of wall 42 are relatively high for both methods. This is due to the neighboring wall 48. The layover areas of these two walls are possibly mixed together. The demolition of wall 48 leads to decreased backscatter in the layover area of wall 42, which results then in a high change ratio of wall 42. Except for this specific situation, the proposed algorithm provides reasonable wall-level change-detection results.

(a)   (b)
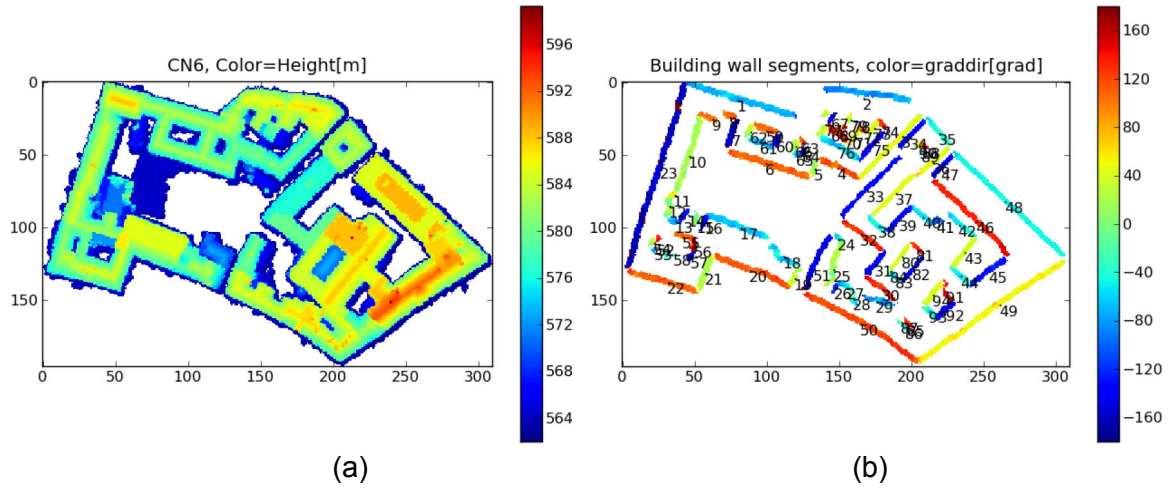
Fig. 6.53: The DSM area of Building 6 (a) and the separated wall segments with wall IDs (b).
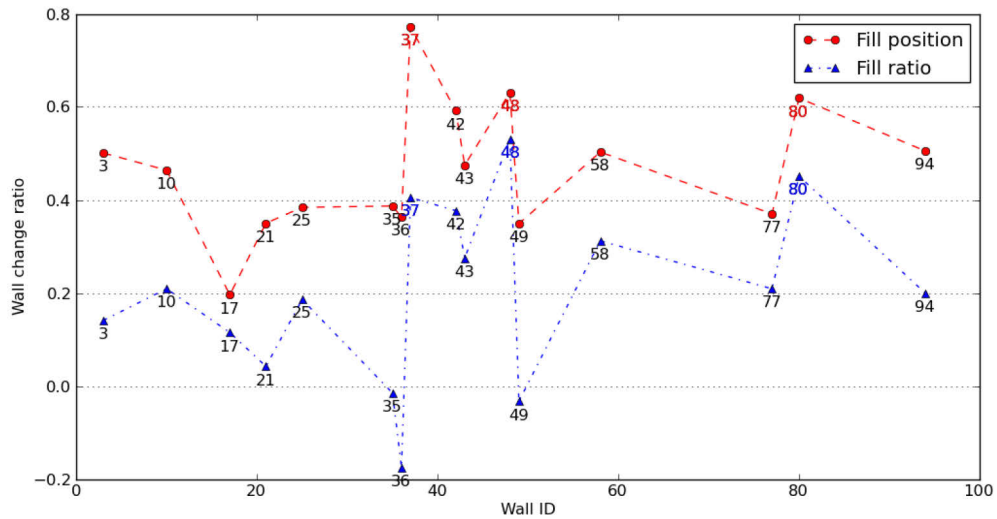
Fig. 6.54: Wall change ratios of the building 6 based on fill position and fill ratio (the IDs represented in red and blue color refer to the three changed walls, see ground truth in Fig. 6.56).

(a)   (b)
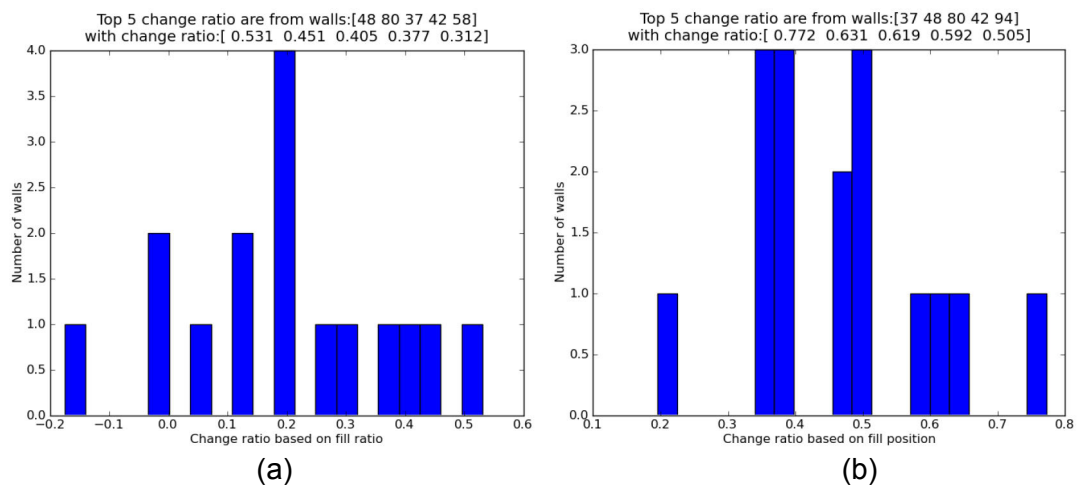
Fig. 6.55: Histogram of the wall change ratios of building 6 based on (a) fill ratio and (b) fill position.
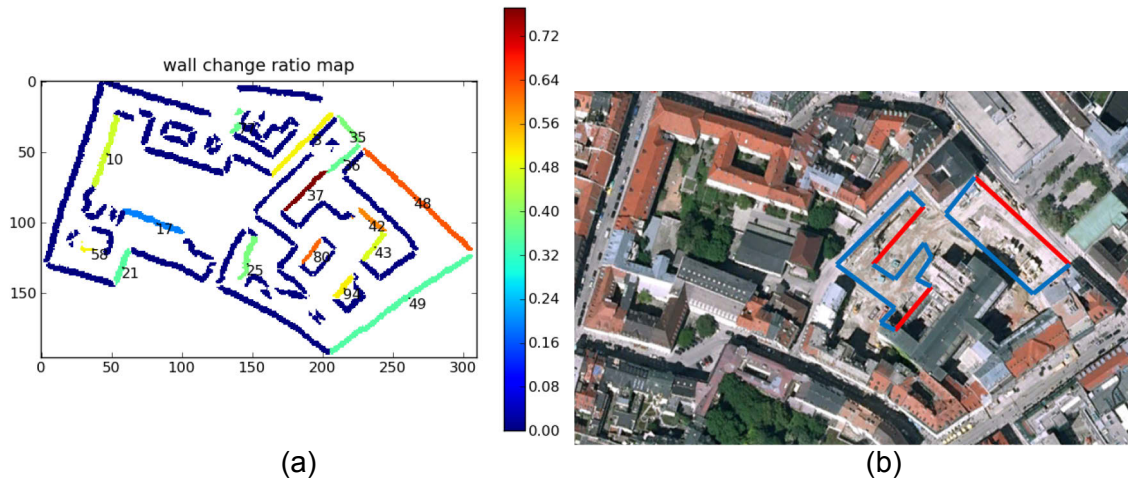
Fig. 6.56: Change ratio map of Building 6 (a) and corresponding reference image (b) extracted from Fig. 6.52b. The three demolished walls 37, 48 and 80 have higher change ratios than the other walls.

Results of all Buildings

As an option, the wall change-detection results can be fused to provide the building change ratios, using the wall layover area as weight and the fill-position-based results. The change ratio values of the 15 buildings are plotted in Fig. 6.57a and represented in a histogram in Fig. 6.57b. Most of the buildings have a fused change ratio between 0.3 and 0.4. Although only a small part of the large building 6 is demolished, this building has a higher change ratio than the other buildings. A change-ratio map is presented in Fig. 6.58a.

In comparison, the same test site is analyzed using the building-layer-fill-based algorithm described in Section 6.3. The change ratio map is presented in Fig. 6.58b. In this case, the partly demolished building 6 has a relatively low change ratio and is not differentiable. This result shows the potential of the wall-level change-detection algorithm for partly demolished buildings.
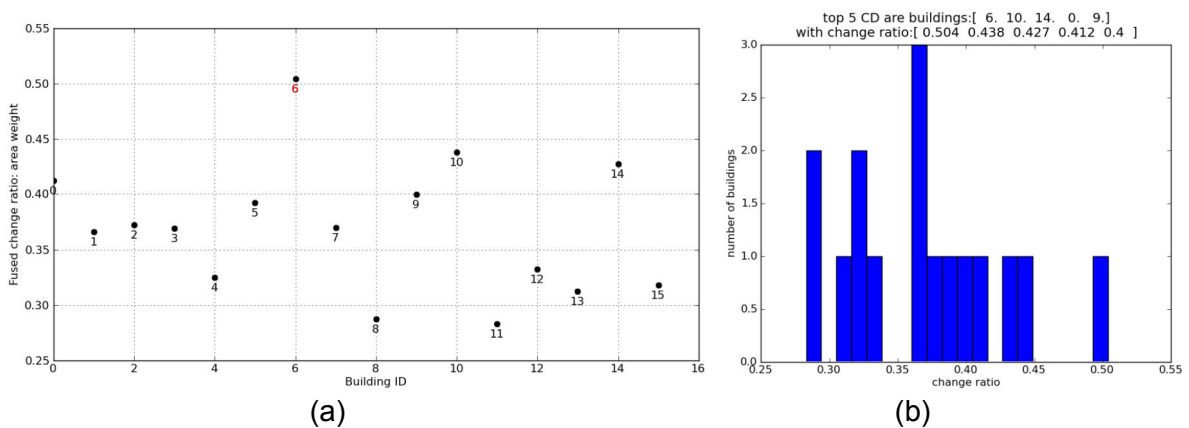
Fig. 6.57: Result of change-detection algorithm based on wall fill position. (a) Plot of building change ratios (the red color represents the changed building 6. (b) histogram of the building change ratios.
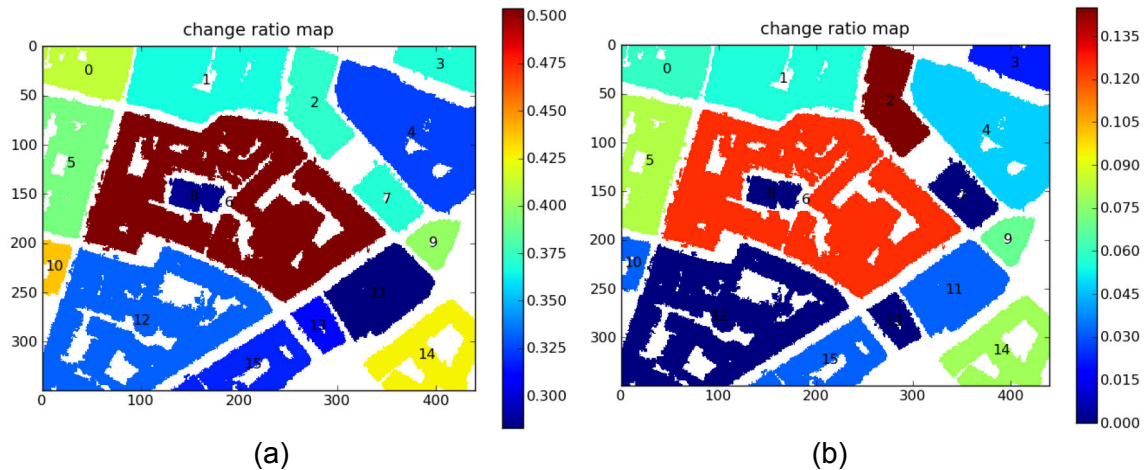
Fig. 6.58: Change detection result of proposed algorithm based on wall fill position (a), in comparison with the result of the algorithm based on building layer fill in Section 6.3 (b).

Conclusion

A novel wall-level change-detection algorithm based on wall fill position is proposed in this section. To this end, "visible" walls are selected from the DSM and simulated to predict their shapes in the SAR images. The corresponding SAR patches of a wall are extracted, converted to have the same geometry, and changed to binary masks. Based on these binary masks, two change ratio values based on fill-ratio and fill-position are calculated. This wall change result can be fused to provide building change ratio. Demolished walls and buildings are correctly detected in the experimental results. Besides this, the wall-level change-detection algorithm yields a better result than building-level change-detection algorithm for partly demolished buildings.

The proposed algorithm relies on the wall segmentation and simulation. It is therefore more time consuming than other proposed algorithms. Because of this, this algorithm is suggested to be performed only for selected buildings or buildings of interest (e.g., building change candidate of other algorithms), as well as in combination with the building-level change-detection algorithms (see Section 6.6.2).

6.6 Comparison and combination of the proposed change-detection algorithms

6.6.1 Comparison of the proposed change-detection algorithms

The properties of all the five proposed change-detection algorithms (Sections 6.2-6.5) are summarized in Table 6.19. For convenience, these algorithms are named as CD_1, CD_2, …, CD_5. The input and output data of them are presented. Additionally, their potential and limitations are briefly discussed.

Table 6.19: Comparison of the proposed five change-detection algorithms

Change-detection Algorithm	Pixel-based LiDAR-SAR	MI- and JHS-based LiDAR-SAR	Building layer-fill-based SAR-SAR	Wall point-feature-based SAR-SAR	Wall fill-position- based SAR-SAR
Name	CD_1	CD_2	CD_3	CD_4	CD_5
Section	6.2.2	6.2.3-6.2.5	6.3	6.4	6.5
Input	• 1 DSM • 1 SAR	• 1 DSM • 1 SAR	• 1 DSM • 2 SAR	• 1 DSM • 2 SAR	• 1 DSM • 2 SAR
Output	Pixels with increased backscattering (new buildings)	Demolished or rebuilt buildings	Demolished buildings	Demolished walls; demolished buildings	Demolished walls; demolished buildings
Method (comparison operator)	Thresholding in dark layers	Building NMI and/or JHS of simulated and real SAR images	Building fill-ratio-based change ratio in 2 SAR images	Ratio of matched point features of walls in 2 SAR images	Fill-position (or fill-ratio) based change ratio of walls
Simulation (Level of analysis)	• DSM	• DSM • Buildings	• DSM • Buildings	• DSM • Buildings • Walls	• DSM • Buildings • Walls
Computation complexity	+	++	++	+++	+++
Potential	• Detection of small changes • Quick processing	• No requirement of pre-event SAR • Stable building change detection	• Stable building change detection	• Towards future applications with increased spatial resolution	• Stable wall change detection • Suitable for partly demolished buildings
Limitations	• No semantic interpretation • Sensitive to surface material	• Not for partly demolished buildings	• Not for partly demolished buildings	• Only for buildings with many point features • Sensible to DSM errors	• Relatively time consuming

6.6.2 Options for combining of different change-detection algorithms

Since the proposed algorithms have different potential, their combination may be application oriented.

For detecting new buildings, the algorithm CD_1 (pixel-based LiDAR-SAR) is the only algorithm proposed in this dissertation. Since CD_1 provide only pixels with increased backscattering without interpretation, the buildings near the detected pixels can be simulated, so that isolated new building and possible rebuilt (or extended) buildings can be differentiated.

In order to detect demolished buildings based on one LiDAR and one SAR data, the method CD_2 (MI- and JHS-based LiDAR-SAR) can be used. Moreover, the result of CD_1 might be helpful for further detection of weakly demolished buildings (e.g., rebuilt buildings).

To detect demolished buildings based on one LiDAR and two SAR data (especially when acquired with different incidence angles), the algorithm CD_3 (Building layer-fill-based SAR-SAR) is suggested. Additionally, CD_2 can be used for identifying the pre-event demolished

buildings (events between the time points t_0 and t_1). These detected buildings are then discarded in the final result. Since CD_3 can hardly detect partly demolished buildings, CD_5 (Wall fill-position-based SAR-SAR) can be applied for selected large buildings (or building blocks), in order to decide whether they are partly demolished.

Both of the algorithms CD_4 and CD_5 can be used to detect demolished walls. For the LiDAR and SAR data at hand, the algorithm CD_5 provides better results. The algorithm CD_4 may work better for future sensors with increased resolution (better than 1 meter resolution of LiDAR and SAR data) to detect changes of detailed structures (e.g., window changes, floor changes).

7   Conclusion and outlook

7.1   Summary and conclusions

In this dissertation, simulation based algorithms for object identification in SAR images and building change detection in urban scenarios are presented. To this end, a novel SAR simulator GeoRaySAR is developed, which uses LiDAR digital surface models as input and automatically generates geocoded simulated images. Based on this simulator, different layers (layover, shadow) of DSM, individual buildings and walls can be identified in SAR images. Especially, an algorithm to segment individual walls from building models has been developed. Moreover, based on the simulator and object identification algorithms, five change detection algorithms have been developed. Among them, a pixel-based algorithm detects increased backscattering in SAR images by comparing LiDAR pre-event data and SAR post-event data. To detect demolished buildings using these two kinds of data, normalized mutual information and a novel comparison operator "joint histogram slope" are used to compare the sub-images in the real and simulated images according to the same building. To detect changes between two SAR images acquired with different incidence angles, one building-level and two wall-level algorithms are developed. The building-level change detection algorithm uses the change ratio based on the fill ratio of building layers as comparison operator. The two wall-level change detection algorithms are based on the wall fill ratio and point feature location, respectively.

With reference to the four objectives discussed in the introduction part, the results of this dissertation are discussed as following.

The first objective is to develop an enhanced SAR simulator to generate geocoded simulated radar images automatically. Based on an existing simulator RaySAR, the simulator GeoRaySAR has been developed, which is specialized on using DSM as input data. The simulator has two main properties. First, it consists of an automatic processing chain including different software packages and programing languages (Python, C and Matlab). It performs fully automatically after giving one DSM and one SAR xml file as input. All parameters the simulation needs are automatically calculated. Second, the generated simulated images are geocoded, which enable a direct comparison with geocoded SAR data. Because of these two properties, this simulator enables an easier fusion of LiDAR and SAR data. Because of the memory consuming property and parallel light assumption during the simulation, the simulator works well for small local scenes (current limit about 2000 m × 2000 m). For larger DSM scenes it is suggested to split it into small ones for simulation.

The second objective is to identify different layers of DSM, individual buildings and walls in SAR images. The main challenging task is to separate individual walls from buildings. For this task, an algorithm based on image processing has been developed. The main contribution of this method is that it preserves walls which may contribute to large layover areas in the corresponding SAR images. Besides of this, various parameters of separated walls are estimated, which are relevant for wall-level SAR image analysis. By combination of different simulated images of the input elevation models, different layers (layover and shadow) of DSM and individual buildings and walls are generated. The fusion of local (buildings and walls) and global (DSM) layers provides reasonable results. The identification improves the interpretation of SAR scenes in dense urban areas where backscattering of different objects are often mixed together. Besides of this, it enables object-based SAR image analysis.

The third objective is to detect changes between LiDAR and SAR data. The change detection between 3D data (e.g., LiDAR) and 2D data (e.g., SAR images) has been rarely

provided in literature. This dissertation contributes a pixel-based algorithm to detect increased backscattering in SAR images by analyzing the SAR pixel values according to simulated layers. To detect demolished buildings, simulated images are generated using LiDAR data. Two comparison operators (normalized mutual information and joint histogram slope) are used to compare image patches related to same buildings. An experiment using Munich data has shown that both of them provide an overall accuracy of more than 90%. A combination of these two comparison operators using decision trees improves the result.

The fourth objective is to detect changes between SAR images acquired with different incidence angles. For this purpose, three algorithms are presented in this dissertation. The first algorithm is a building-level algorithm based on layer fill. Image patches related to the same buildings in the two SAR images are extracted using simulation methods. For each extracted image patch pair, the change ratio based on the fill ratio of building layers is estimated. The change ratio values of all buildings are then classified into two classes using the EM-algorithm. This algorithm works well for buildings with different size and shape in complex urban scenarios. Since the whole building is analyzed as one object, buildings with partly demolished walls may not be detected. Under the same idea, a wall-level change detection algorithm was developed. Image patches related to the same walls in the two SAR images were extracted and converted to have the same geometry. These converted patch pairs are then compared using change ratios based on fill ratio or fill position. Lastly, the wall change results are fused to provide building change result. Compared to the building-level change detection algorithm, this method is more time consuming, but yields better results for partly demolished buildings. A combination of these two algorithms is therefore suggested, whereby the building-level method is used for all buildings and wall-level method additionally for selected large buildings. The third developed algorithm is a wall-level change detection algorithm based on point-feature location. To this end, local maximum points in two SAR images corresponding to the same building façade are compared. This method provides promising result for the present data. It may work better for future data with increased resolution to detect changes of detailed façade structures.

7.2 Outlook

The proposed SAR simulator GeoRaySAR and its application in change detection provide a good basis for future research on remote sensing applications. Based on these results, potential future work is discussed under the following perspectives.

7.2.1 Other input data of 3D city or building models

The input data of GeoRaySAR is DSMs derived from LiDAR point clouds. The developed software package can be extended to other 3D data, like DSM derived from optical stereo matching, or GIS-Data like CityGML (City Geography Markup Language) data or SketchUp data. This kind of 3D data can provide comparable simulation results to identify layover and shadow masks.

The current optical sensors on different platforms (satellite, airplanes or unmanned aerial vehicles) can provide optical images up to decimeter-resolution. Combined with the state of the art techniques of dense stereo matching (e.g., semi global matching, total variation), DSM with higher spatial resolution can be generated. This kind of DSM can be directly used as input in GeoRaySAR. However, since the point accuracy from stereo matching might not be perfect, the generated DSM surface might be rough, which may lead to inhomogeneous signatures in the simulated images. To compensate this affect, techniques like building

modeling or DSM enhancement (discussed in Section 5.1) can be involved as a preprocessing step for the DSMs from optical stereo matching.

An extended version of GeoRaySAR using CityGML data as input is under development at the Chair of Remote Sensing Technology of Technische Universität München. The simulated results may look like "artificial", but they are enough for applications like object identification in SAR images discussed in Chapter 4. Moreover, the CityGML data provides additional information besides of 3D building geometry (e.g., surface feature of roof, wall, vegetation), which may ease some of the methods proposed in this dissertation (e.g., wall extraction in Chapter 5).

Additional information like surface material is also interesting for the simulation of images with high radiometric similarity, since signatures in SAR images dependent not only on geometric shape, but also on the surface material. This information can be provided by hyperspectral sensors. Exploiting the surface material in the simulation, the simulated images may be not only geometrically but also radiometrically similar. This will provide a great potential on applications like image interpretation and change detection.

7.2.2 Other input data of SAR images

The proposed work used only TerraSAR-X GEC products for simulation. For some remote sensing applications (e.g., Persistent Scatterer Interferometry), the interpretation of the original SAR images in azimuth-range map (SSC product) may be relevant. To this end, an extension of GeoRaySAR may be interesting, which generates simulated images in azimuth-range geometry and provides the link to SAR SSC products. The difficulty of this task is the geometric linking of small simulated images with large SAR scenes using the geoinformation of DSM and SAR satellite orbit information.

Additionally, the future SAR products with higher resolution (e.g., Staring Spotlight imaging mode of TerraSAR-X with up to 25cm resolution) will provide more detail information of buildings and other objects. To simulate images for such products may lead to more applications.

7.2.3 Other change detection methods

This dissertation provides five different change-detection algorithms to detect changes between LiDAR-SAR or SAR-SAR. Since very few articles have provided methods for simulation based change detection, technique gaps can still be found in this research field. Methods based on extraction of geometrical primitives (e.g., double bounce signals) or statistical features of individual buildings can be pursued. Besides of this, SAR images with higher resolution may provide detailed information about buildings. This will provide the opportunity of detecting changes on a higher level (e.g., window-level).

7.2.4 Other applications

The aim of the proposed change detection algorithm is to detect collapsed buildings in urgent situations like earthquakes. Unfortunately, this application has not been tested so far, because of the lack of test data. The proposed approaches require a pre-event LiDAR data for SAR simulation. This is however not the case for the existing earthquake events, as most earthquakes happened in the countryside not in big cities, where the LiDAR data is available. On the viewpoint of the author, this will not be a big problem in near feature. On one hand the LiDAR data will increase in numbers with time. On the other hand, more and more high accurate 3D data will be provided by optical stereo matching and GIS data. After the

extension of the simulator by using other kinds of 3D data, the change-detection algorithms can be tested in disaster areas for damage assessment.

In addition, the simulator can be used for other remote sensing applications like object recognition and mission planning. Giving a ship model and several potential ship locations in a SAR image, simulated images can be generated and compared with SAR image patches to estimate the ship location. Given a database of different ship models and a ship location in a SAR image, the simulation technique can recognize the ship type in the SAR image.

Acknowledgments

Bibliography

Acharya, T., Ray, A.K., (2005). Image processing: principles and applications. John Wiley, Hoboken, N.J.

Ackermann, F., (1999). Airborne laser scanning—present status and future expectations. ISPRS J. Photogramm. Remote Sens. 54, 64–67.

Arefi, H., d' Angelo, P., Mayer, H., Reinartz, P., (2011). Iterative approach for efficient digital terrain model production from CARTOSAT-1 stereo images. J. Appl. Remote Sens. 5, 053527–053527–19.

Arefi, H., Reinartz, P., (2013). Building Reconstruction Using DSM and Orthorectified Images. Remote Sens. 5, 1681–1703.

Auer, S., Balz, T., Becker, S., Bamler, R., (2010a). 3D SAR Simulation of Urban Areas Based on Detailed Building Models. Photogramm. Eng. Remote Sens. 76, 1373–1384.

Auer, S., Gernhardt, S., (2014). Linear Signatures in Urban SAR Images-Partly Misinterpreted? IEEE Geosci. Remote Sens. Lett. 11, 1762–1766.

Auer, S., Gernhardt, S., Bamler, R., (2011). Ghost Persistent Scatterers Related to Multiple Signal Reflections. IEEE Geosci. Remote Sens. Lett. 8, 919–923.

Auer, S., Gisinger, C., Bamler, R., (2012). Characterization of SAR image patterns pertinent to individual facades, in: Proceedings of IEEE International Geoscience and Remote Sensing Symposium (IGARSS). pp. 3611–3614.

Auer, S., Hinz, S., Bamler, R., (2010b). Ray-Tracing Simulation Techniques for Understanding High-Resolution SAR Images. IEEE Trans. Geosci. Remote Sens. 48, 1445–1456.

Auer, S.J., (2011). 3D synthetic aperture radar simulation for interpreting complex urban reflection scenarios. München, Techn. Univ., Diss., 2011.

Balz, T., (2004). SAR simulation based change detection with high-resolution SAR images in urban environments. ISPRS Arch. 35.

Balz, T., (2010). SAR simulation of urban areas: techniques and applications, in: Radar Remote Sensing of Urban Areas. Springer, pp. 215–231.

Balz, T., Becker, S., Haala, N., Kada, M., (2008). Using real-time SAR simulation to assist pattern recognition applications in urban areas. Pattern Recognit. Image Anal. 18, 412–416.

Balz, T., Liao, M., (2010). Building-damage detection using post-seismic high-resolution SAR satellite data. Int. J. Remote Sens. 31, 3369–3391.

Balz, T., Stilla, U., (2009). Hybrid GPU-Based Single- and Double-Bounce SAR Simulation. IEEE Trans. Geosci. Remote Sens. 47, 3519–3529.

Ban, Y., Yousif, O.A., (2012). Multitemporal Spaceborne SAR Data for Urban Change Detection in China. IEEE J. Sel. Top. Appl. Earth Obs. Remote Sens. 5, 1087–1094.

Barthelet, E., Mercier, G., Denise, L., (2011). Building change detection in a couple of optical and SAR high resolution images, in: Proceedings of IEEE International Geoscience and Remote Sensing Symposium (IGARSS). pp. 2393–2396.

Barthelet, E., Mercier, G., Denise, L., Reynaud, S., (2012). Feature based maximum likelihood model inversion for three-dimensional building extraction from single high resolution SAR images, in: Proceedings of IEEE International Geoscience and Remote Sensing Symposium (IGARSS). pp. 3600–3603.

Bazi, Y., Bruzzone, L., Melgani, F., (2005). An unsupervised approach based on the generalized Gaussian model to automatic change detection in multitemporal SAR images. IEEE Trans. Geosci. Remote Sens. 43, 874–887.

Bazi, Y., Bruzzone, L., Melgani, F., (2007). Image thresholding based on the EM algorithm and the generalized Gaussian distribution. Pattern Recognit. 40, 619–634.

Berger, C., Voltersen, M., Eckardt, R., Eberle, J., Heyer, T., Salepci, N., Hese, S., Schmullius, C., Tao, J., Auer, S., Bamler, R., Ewald, K., Gartley, M., Jacobson, J., Buswell, A., Du, Q., Pacifici, F., (2013). Multi-Modal and Multi-Temporal Data Fusion: Outcome of the 2012 GRSS Data Fusion Contest. IEEE J. Sel. Top. Appl. Earth Obs. Remote Sens. 6, 1324–1340.

Bolter, R., (2001). Buildings from SAR: detection and reconstruction of buildings from multiple view high resolution interferometric SAR data. University Graz.

Bovolo, F., Bruzzone, L., (2005). A detail-preserving scale-driven approach to change detection in multitemporal SAR images. IEEE Trans. Geosci. Remote Sens. 43, 2963–2972.

Bovolo, F., Bruzzone, L., (2007). A Split-Based Approach to Unsupervised Change Detection in Large-Size Multitemporal Images: Application to Tsunami-Damage Assessment. IEEE Trans. Geosci. Remote Sens. 45, 1658–1670.

Breit, H., Fritz, T., Balss, U., Lachaise, M., Niedermeier, A., Vonavka, M., (2010). TerraSAR-X SAR Processing and Products. IEEE Trans. Geosci. Remote Sens. 48, 727–740.

Brett, P.T.B., Guida, R., (2013). Earthquake Damage Detection in Urban Areas Using Curvilinear Features. IEEE Trans. Geosci. Remote Sens. 51, 4877–4884.

Brunner, D., Lemoine, G., Bruzzone, L., (2010a). Earthquake Damage Assessment of Buildings Using VHR Optical and SAR Imagery. IEEE Trans. Geosci. Remote Sens. 48, 2403–2420.

Brunner, D., Lemoine, G., Bruzzone, L., Greidanus, H., (2010b). Building Height Retrieval From VHR SAR Imagery Based on an Iterative Simulation and Matching Technique. IEEE Trans. Geosci. Remote Sens. 48, 1487–1504.

Brunner, D., Lemoine, G., Greidanus, H., Bruzzone, L., (2011). Radar Imaging Simulation for Urban Structures. IEEE Geosci. Remote Sens. Lett. 8, 68–72.

Bruzzone, L., Bovolo, F., (2013). A Novel Framework for the Design of Change-Detection Systems for Very-High-Resolution Remote Sensing Images. Proc. IEEE 101, 609–630.

Bruzzone, L., Prieto, D.F., (2000). Automatic analysis of the difference image for unsupervised change detection. IEEE Trans. Geosci. Remote Sens. 38, 1171–1182.

Buck, D., (2014). The Early History of POV-Ray. http://www.povray.org/documentation/view/3.6.0/7/ [checked: 15.Aug.2014].

Carincotte, C., Derrode, S., Bourennane, S., (2006). Unsupervised change detection on SAR images using fuzzy hidden Markov chains. IEEE Trans. Geosci. Remote Sens. 44, 432–441.

Celik, T., (2009). Multiscale Change Detection in Multitemporal Satellite Images. IEEE Geosci. Remote Sens. Lett. 6, 820–824.

Chini, M., Pierdicca, N., Emery, W.J., (2009). Exploiting SAR and VHR Optical Images to Quantify Damage Caused by the 2003 Bam Earthquake. IEEE Trans. Geosci. Remote Sens. 47, 145–152.

Cohen, J., (1960). A Coefficient of Agreement for Nominal Scales. Educ. Psychol. Meas. 20, 37–46.

Cui, S., Datcu, M., (2012). Statistical Wavelet Subband Modeling for Multi-Temporal SAR Change Detection. IEEE J. Sel. Top. Appl. Earth Obs. Remote Sens. 5, 1095–1109.

Dekker, R.J., (2011). High-Resolution Radar Damage Assessment After the Earthquake in Haiti on 12 January 2010. IEEE J. Sel. Top. Appl. Earth Obs. Remote Sens. 4, 960–970.

Deledalle, C.-A., Denis, L., Tupin, F., (2009). Iterative Weighted Maximum Likelihood Denoising With Probabilistic Patch-Based Weights. IEEE Trans. Image Process. 18, 2661–2672.

Dell'Acqua, F., Bignami, C., Chini, M., Lisini, G., Polli, D.A., Stramondo, S., (2011). Earthquake Damages Rapid Mapping by Satellite Remote Sensing Data: L'Aquila April 6th, 2009 Event. IEEE J. Sel. Top. Appl. Earth Obs. Remote Sens. 4, 935–943.

Dell'Acqua, F., Gamba, P., (2012). Remote Sensing and Earthquake Damage Assessment: Experiences, Limits, and Perspectives. Proc. IEEE 100, 2876–2890.

Dempster, A.P., Laird, N.M., Rubin, D.B., (1977). Maximum likelihood from incomplete data via the EM algorithm. J. R. Stat. Soc. Ser. B Methodol. 1–38.

Duda, R.O., Hart, P.E., Stork, D.G., (2001). Pattern Classification. John Wiley & Sons.

Ehrlich, D., Guo, H.D., Molch, K., Ma, J.W., Pesaresi, M., (2009). Identifying damage caused by the 2008 Wenchuan earthquake from VHR remote sensing data. Int. J. Digit. Earth 2, 309–326.

Ferro, A., Brunner, D., Bruzzone, L., (2013). Automatic Detection and Reconstruction of Building Radar Footprints From Single VHR SAR Images. IEEE Trans. Geosci. Remote Sens. 51, 935–952.

Ferro, A., Brunner, D., Bruzzone, L., Lemoine, G., (2011). On the Relationship Between Double Bounce and the Orientation of Buildings in VHR SAR Images. IEEE Geosci. Remote Sens. Lett. 8, 612–616.

Franceschetti, G., Iodice, A., Riccio, D., Ruello, G., (2003). SAR raw signal simulation for urban structures. IEEE Trans. Geosci. Remote Sens. 41, 1986–1995.

Fujii, T., Fukuchi, T., (2005). Laser Remote Sensing. CRC Press.

Gamba, P., Dell'Acqua, F., Lisini, G., (2006). Change Detection of Multitemporal SAR Data in Urban Areas Combining Feature-Based and Pixel-Based Techniques. IEEE Trans. Geosci. Remote Sens. 44, 2820–2827.

Gamba, P., Dell'Acqua, F., Trianni, G., (2007). Rapid Damage Detection in the Bam Area Using Multitemporal SAR and Exploiting Ancillary Data. IEEE Trans. Geosci. Remote Sens. 45, 1582–1589.

Gelautz, M., Frick, H., Raggam, J., Burgstaller, J., Leberl, F., (1998). SAR image simulation and analysis of alpine terrain. ISPRS J. Photogramm. Remote Sens. 53, 17–38.

Gruenthal, G. (Ed.), (1998). European Macroseismic Scale 1998. Cahiers du Centre European de Geodynamique et de Seismologie, Luxembourg.

Guida, R., Iodice, A., Riccio, D., Stilla, U., (2008). Model-Based Interpretation of High-Resolution SAR Images of Buildings. IEEE J. Sel. Top. Appl. Earth Obs. Remote Sens. 1, 107–119.

Haala, N., Kada, M., (2010). An update on automatic 3D building reconstruction. ISPRS J. Photogramm. Remote Sens. 65, 570–580.

Hammer, H., Schulz, K., (2011). SAR-simulation of large urban scenes using an extended ray tracing approach, in: Proceedings of Joint Urban Remote Sensing Event (JURSE). pp. 289–292.

Huo, C., Zhou, Z., Lu, H., Pan, C., Chen, K., (2010). Fast object-level change detection for VHR images. IEEE Geosci. Remote Sens. Lett. 7, 118–122.

Inglada, J., Mercier, G., (2007). A New Statistical Similarity Measure for Change Detection in Multitemporal SAR Images and Its Extension to Multiscale Change Analysis. IEEE Trans. Geosci. Remote Sens. 45, 1432–1445.

Joe, H., (1989). Relative entropy measures of multivariate dependence. J. Am. Stat. Assoc. 84, 157–164.

Keeping, E.S., Kenney, J.F., (1965). Mathematics of Statistics. Affiliated East- West Press.

Kittler, J., Illingworth, J., (1986). Minimum error thresholding. Pattern Recognit. 19, 41–47.

Kullback, S., Leibler, R.A., (1951). On information and sufficiency. Ann. Math. Stat. 22, 79–86.

Lafarge, F., Descombes, X., Zerubia, J., Pierrot-Deseilligny, M., (2008). Automatic building extraction from DEMs using an object approach and application to the 3D-city modeling. ISPRS J. Photogramm. Remote Sens. 63, 365–381.

Lee, J.-S., (1981). Speckle analysis and smoothing of synthetic aperture radar images. Comput. Graph. Image Process. 17, 24–32.

Li, H.-C., Hong, W., Wu, Y.-R., Fan, P.-Z., (2011). On the Empirical-Statistical Modeling of SAR Images With Generalized Gamma Distribution. IEEE J. Sel. Top. Signal Process. 5, 386–397.

Longbotham, N., Pacifici, F., Glenn, T., Zare, A., Volpi, M., Tuia, D., Christophe, E., Michel, J., Inglada, J., Chanussot, J., Du, Q., (2012). Multi-Modal Change Detection, Application to the Detection of Flooded Areas: Outcome of the 2009-2010 Data Fusion Contest. IEEE J. Sel. Top. Appl. Earth Obs. Remote Sens. 5, 331–342.

Lu, D., Mausel, P., Brondízio, E., Moran, E., (2004). Change detection techniques. Int. J. Remote Sens. 25, 2365–2401.

Luo, F., Yang, W., Wu, Q., Yan, W., (2012). A clustering approach for change detection in SAR images, in: Proceedings of 9th European Conference on Synthetic Aperture Radar (EUSAR). pp. 388–391.

Mametsa, H.-J., Rouas, F., Berges, A., Latger, J., (2002). Imaging radar simulation in realistic environment using shooting and bouncing rays technique. pp. 34–40.

Margarit, G., Mallorqui, J.J., Rius, J.M., Sanz-Marcos, J., (2006). On the Usage of GRECOSAR, an Orbital Polarimetric SAR Simulator of Complex Targets, to Vessel Classification Studies. IEEE Trans. Geosci. Remote Sens. 44, 3517–3526.

Marin, C., Bovolo, F., Bruzzone, L., (2015). Building Change Detection in Multitemporal Very High Resolution SAR Images. IEEE Trans. Geosci. Remote Sens. 53, 2664–2682.

Matsuoka, M., Yamazaki, F., (2004). Use of Satellite SAR Intensity Imagery for Detecting Building Areas Damaged Due to Earthquakes. Earthq. Spectra 20, 975–994.

Moser, G., Serpico, S.B., (2006). Generalized minimum-error thresholding for unsupervised change detection from SAR amplitude imagery. IEEE Trans. Geosci. Remote Sens. 44, 2972–2982.

Oliver, C., Quegan, S., (2004). Understanding Synthetic Aperture Radar Images. SciTech Publishing.

Radke, R.J., Andra, S., Al-Kofahi, O., Roysam, B., (2005). Image change detection algorithms: a systematic survey. IEEE Trans. Image Process. 14, 294–307.

Redner, R.A., Walker, H.F., (1984). Mixture densities, maximum likelihood and the EM algorithm. SIAM Rev. 26, 195–239.

Rottensteiner, F., Briese, C., (2002). A new method for building extraction in urban areas from high-resolution LIDAR data. Int. Arch. Photogramm. Remote Sens. Spat. Inf. Sci. 34, 295–301.

Saerndal, C.E., (1974). A comparative study of association measures. Psychometrika 39, 165–187.

Schmitt, A., Wessel, B., Roth, A., (2009). Curvelet approach for SAR image denoising, structure enhancement, and change detection. Int. Arch. Photogramm. Remote Sens. Spat. Inf. Sci. 38, 151–156.

Schreier, G., (1993). SAR geocoding: data and systems. Wichmann.

Shannon, C.E., (1948). A mathematical theory of communication. Bell Syst Tech J 27, 379–423/623–656.

Siegel, A.F., (1982). Robust regression using repeated medians. Biometrika 69, 242–244.

Simonetto, E., Oriot, H., Garello, R., (2005). Rectangular building extraction from stereoscopic airborne Radar images. IEEE Trans. Geosci. Remote Sens. 43, 2386–2395.

Soergel, U., (2003). Iterative Verfahren zur Detektion und Rekonstruktion von Gebäuden in SAR- und InSAR-Daten. Leibniz University of Hannover.

Soergel, U. (Ed.), (2010). Radar remote sensing of urban areas. Springer.

Soergel, U., Schulz, K., Thoennessen, U., Stilla, U., (2005). Integration of 3D data in SAR mission planning and image interpretation in urban areas. Inf. Fusion 6, 301–310.

Soergel, U., Thoennessen, U., Brenner, A., Stilla, U., (2006). High-resolution SAR data: new opportunities and challenges for the analysis of urban areas. Radar Sonar Navig. IEE Proc. - 153, 294–300.

Soergel, U., Thoennessen, U., Stilla, U., (2003). Visibility analysis of man-made objects in SAR images, in: Proceedings of 2nd GRSS/ISPRS Joint Workshop on Remote Sensing and Data Fusion over Urban Areas. pp. 120–124.

Sportouche, H., Tupin, F., Denise, L., (2011). Extraction and Three-Dimensional Reconstruction of Isolated Buildings in Urban Scenes From High-Resolution Optical and SAR Spaceborne Images. IEEE Trans. Geosci. Remote Sens. 49, 3932–3946.

Stramondo, S., Bignami, C., Chini, M., Pierdicca, N., Tertulliani, A., (2006). Satellite radar and optical remote sensing for earthquake damage detection: results from different case studies. Int. J. Remote Sens. 27, 4433–4447.

Strehl, A., Ghosh, J., (2003). Cluster ensembles—a knowledge reuse framework for combining multiple partitions. J. Mach. Learn. Res. 3, 583–617.

Studholme, C., Hill, D.L., Hawkes, D.J., (1999). An overlap invariant entropy measure of 3D medical image alignment. Pattern Recognit. 32, 71–86.

Sui, H., Li, D., Gong, J., (2004). Automatic feature-level change detection (flcd) for road networks. Int. Soc. Photogramm. Remote Sens. Geo-Imag. Bridg. Cont. 459–464.

Suri, S., (2010). Automatic image to image registration for multimodal remote sensing images. TECHNISCHE UNIVERSITÄT MÜNCHEN.

Tao, J., Auer, S., Palubinskas, G., Reinartz, P., Bamler, R., (2014). Automatic SAR Simulation Technique for Object Identification in Complex Urban Scenarios. IEEE J. Sel. Top. Appl. Earth Obs. Remote Sens. 7, 994–1003.

Tao, J., Auer, S., Reinartz, P., (2012). Detecting changes between a DSM and a high resolution SAR image with the support of simulation based separation of urban scenes, in: Proceedings of 9th European Conference on Synthetic Aperture Radar (EUSAR). pp. 95–98.

Tao, J., Auer, S., Reinartz, P., Bamler, R., (2013). Object-based change detection for individual buildings in SAR images captured with different incidence angles, in: Proceedings of IEEE International Geoscience and Remote Sensing Symposium (IGARSS). pp. 1238–1241.

Tao, J., Palubinskas, G., Reinartz, P., (2011a). Automatic interpretation of high resolution SAR images: first results of SAR image simulation for single buildings, in: Proceedings of ISPRS Hannover Workshop. pp. 14–17.

Tao, J., Palubinskas, G., Reinartz, P., (2011b). Simulation Based Change Detection between DSM and High Resolution SAR Image, in: Proceedings of International Symposium on Image and Data Fusion (ISIDF). pp. 1–4.

Tao, J., Palubinskas, G., Reinartz, P., Auer, S., (2011c). Interpretation of SAR images in urban areas using simulated optical and radar images, in: Proceedings of Joint Urban Remote Sensing Event (JURSE). pp. 41–44.

Tong, X., Hong, Z., Liu, S., Zhang, X., Xie, H., Li, Z., Yang, S., Wang, W., Bao, F., (2012). Building-damage detection using pre- and post-seismic high-resolution satellite stereo imagery: A case study of the May 2008 Wenchuan earthquake. ISPRS J. Photogramm. Remote Sens. 68, 13–27.

Touzi, R., Lopes, A., Bousquet, P., (1988). A statistical and geometrical edge detector for SAR images. IEEE Trans. Geosci. Remote Sens. 26, 764–773.

Tupin, F., Maitre, H., Mangin, J.-F., Nicolas, J.-M., Pechersky, E., (1998). Detection of linear features in SAR images: application to road network extraction. IEEE Trans. Geosci. Remote Sens. 36, 434–453.

Verma, V., Kumar, R., Hsu, S., (2006). 3D Building Detection and Modeling from Aerial LIDAR Data, in: Proceedings of IEEE Computer Society Conference on Computer Vision and Pattern Recognition. pp. 2213–2220.

Wang, F., Wu, Y., Zhang, Q., Zhang, P., Li, M., Lu, Y., (2013). Unsupervised Change Detection on SAR Images Using Triplet Markov Field Model. IEEE Geosci. Remote Sens. Lett. 10, 697–701.

Wang, T.-L., Jin, Y.-Q., (2012). Postearthquake Building Damage Assessment Using Multi-Mutual Information From Pre-Event Optical Image and Postevent SAR Image. IEEE Geosci. Remote Sens. Lett. 9, 452–456.

Wegmueller, U., (1999). Automated terrain corrected SAR geocoding, in: Proceedings of IEEE International Geoscience and Remote Sensing Symposium (IGARSS). pp. 1712–1714 vol.3.

Wegner, J.D., Auer, S., Soergel, U., (2010). Extraction and Geometrical Accuracy of Double-bounce Lines in High Resolution SAR Images. Photogramm. Eng. Remote Sens. 76, 1071–1080.

Weng, Q., Quattrochi, D.A., (2006). Urban Remote Sensing. CRC Press.

Xie, H., Pierce, L.E., Ulaby, F.T., (2002). SAR speckle reduction using wavelet denoising and Markov random field modeling. IEEE Trans. Geosci. Remote Sens. 40, 2196–2212.

Xie, H., Pierce, L.E., Ulaby, F.T., (2003). Mutual information based registration of SAR images, in: Proceedings of IEEE International Geoscience and Remote Sensing Symposium (IGARSS). pp. 4028–4031 vol.6.

Xu, F., Jin, Y.-Q., (2006). Imaging Simulation of Polarimetric SAR for a Comprehensive Terrain Scene Using the Mapping and Projection Algorithm. IEEE Trans. Geosci. Remote Sens. 44, 3219–3234.

Zhou, Q.-Y., Neumann, U., (2008). Fast and extensible building modeling from airborne LiDAR data, in: Proceedings of the 16th ACM SIGSPATIAL International Conference on Advances in Geographic Information Systems. p. 7.

List of tables

List of figures